Bimaterial Lattices With Anisotropic Thermal Expansion

by

Marina Toropova

A thesis submitted in conformity with the requirements
for the degree of Doctor of Philosophy
Graduate Department of Aerospace Science and Engineering
University of Toronto

Abstract

Bimaterial Lattices With Anisotropic Thermal Expansion

Marina Toropova
Doctor of Philosophy
Graduate Department of Aerospace Science and Engineering
University of Toronto
2016

Numerous structures that are used in the aerospace and automobile industries, microelectronics, and civil engineering are subject to large variations of temperature. The deformations caused by temperature can be dangerous because they lead to thermal stresses and failure if materials with mismatched thermal expansion are joined. On the other hand, thermal extensions can be used to achieve desirable displacements in structures. In this work, we use bimaterial lattices made of two materials and empty space that combine low weight with high stiffness and structural robustness. The lattices can serve as adapters that eliminate or mitigate dangerous thermal stresses, as elements for fine tuning, or as thermal actuators. To perform these functions, the lattices must be anisotropic, which can be achieved if the lattice consists of non-identical anisotropic cells. Each cell is composed of an irregular triangle made of one material surrounded by a skewed hexagon made of another material. The overall performance of the lattice is defined by six hexagon skew angles and the ratio of the two coefficients of thermal expansion (CTEs) of the lattice materials. The cells are connected to adjoining cells at three points; changes in the distances between these points as a function of temperature can be tailored.

The primary goal of the research is to elaborate general principles and algorithms to design lattices, select material, and improve structural efficiency. Several adaptive lattices are designed including a polygonal ring connector to prevent distortion in cylindrical optical components, a lattice preventing shaft and collar sticking, and lattices controlling the total deflection of two substrates. Lattices providing predetermined displacements in

desirable directions have been studied, and it was demonstrated that different temperature supplied to different cells of a polygonal ring connector can be used for fine tuning of optical lenses. Finally, thermal actuators - a switch, tweezers, and a valve - are designed. In terms of overall performance, the actuators are slow but do not exhibit hysteresis: their thermal expansion depends on temperature but not on preceding thermal history. The forces and deflections they achieve compare favorably with piezoelectrics and shape memory alloys.

Acknowledgements

I would like to express my thanks and esteemed gratitude to Professor Craig A. Steeves for his help and guidance in completing this thesis. It was a privilege to work with him. His encouragements and suggestions have been tremendously helpful over the course of my research.

I would also like to thank my DEC Advisors, Prof. Prasanth B. Nair, Prof. Glenn D. Hibbard, and Prof. Peter R. Grant for their constructive feedback during the following project.

Experimental equipment for the work in our lab and participation in conferences were made available by the funding provided by NSERC.

I would also like to thank my colleagues Bharat Bhaga, Qian Zhang, David Platt, Nicholas Ewaschuk, Jialian Wu, and Sandipan Chatterjee for always being available to bounce questions off of and for their help in the lab.

Last but not least, I would like to thank my family and friends for their help and encouragement in my studies.

Contents

List of Tables

List of Figures

Chapter 1

Introduction

1.1 Motivation

Bimaterial lattices are made of two materials and empty space. The low weight and high performance of bimaterial lattices as structural elements motivate their wide use in a variety of aerospace and automotive applications, microelectronics, and civil engineering. Lattices can be designed to have several unique desirable properties and to serve as multifunctional solutions to engineering problems. This thesis explores new concepts for lattices with tailored anisotropic thermal expansion properties. Such lattices can be used as stress-free adapters to mitigate thermal expansion mismatch, as adapters between substrates with complex geometric shapes, and, finally, as thermally driven actuators. This thesis demonstrates that it is possible to combine precise thermal deformations with high stiffness while eliminating thermal mismatch stresses. This combination of properties is unobtainable through other concepts.

The most common lattice structures have tetrahedral, pyramidal, kagome, and honeycomb cell configurations. Various authors (Fan et al., 2008, 2009; Vigliotti and Pasini, 2012; Zhang et al., 2008) studied their mechanical properties: effective elastic moduli, yield strength, local and general buckling, and failure mechanisms. As it was indicated in Gibson and Ashby (1997), lattice structures can provide good energy absorption characteristics and good thermal and acoustic insulation properties. In other works (Abad et al., 2012; Elsayed and Pasini, 2009, 2010; Liu and Lu, 2004; Vigliotti and Pasini, 2015; Wicks and Hutchinson, 2001), design optimization of multifunctional lattice structures was performed for specific applications. Nonlinear constitutive models for lattice materials were created in Vigliotti et al. (2014). The possibility of tailoring acoustic and thermal properties of lattice materials was studied in Chopra and Phani (2011); Phani (2011a,b); Phani and Fleck (2007, 2008); Phani et al. (2006). The idea to use lattice

structures for actuation was expressed and realized in Hutchinson et al. (2003); Leung et al. (2004); Li et al. (2011); Mikulas et al. (1993); Miura (1984a,b); Wicks and Guest (2004).

In this work, we consider a specific class of lattice structures - nonperiodic anisotropic bimaterial lattices composed of nonidentical anisotropic cells. They combine low weight with high stiffness and structural robustness. The key property of these lattices is their ability to attain desirable thermal expansion in different directions. These lattices are designed to be used in ambient conditions with large variations in temperature. Exploited in such conditions, the lattices can mitigate or eliminate stresses due to thermal deformation mismatch in structures made of materials with different coefficients of thermal expansion (CTEs). Alternately, they can be tailored to provide significant deflections of their specific vertices when temperature changes. This can be used for fine tuning of structures or thermal actuation. As thermal actuators they do not need compliant mechanisms and also they do not exhibit aging or hysteresis; that is, their thermal deformation does not depend on thermal history but only on the current temperature. They have a slow response and can create deformations larger than piezoelectics but smaller than shape memory alloy actuators. For all of these applications, they do not experience thermal mismatch stresses when the joints are pinned.

1.2 Isotropic bimaterial lattices with predetermined CTE

Bimaterial lattices made of two materials and empty space and having predetermined negative, zero, or positive CTEs were considered in Jefferson et al. (2009); Lakes (1996, 2007); Sigmund and Torquato (1996, 1997); and Steeves et al. (2007). In these works, it was demonstrated that a lattice with a desirable isotropic CTE can be constructed from cells incorporating two materials with widely differing individual CTEs and empty space. For example, a cellular structure consisting of bi-layered ribs and empty space is proposed in Lakes (1996) (fig. 1.1). The layers have different thickness and are made of materials with different CTEs. As it was indicated by Timoshenko (1925), the ribs flex when temperature changes releasing thermal strain in open space. The formulae for their curvature and length after flexing are obtained by Lakes (1996). The overall CTE of the lattice (fig. 1.1) is exactly equal to the CTE of an individual rib. The slenderer ribs are, the higher lattice CTE is. Also, the lattice CTE increases if the ribs have initial curvature. If the constituent with the higher CTE is on its concave side, an increase in

temperature will cause the rib to straighten, giving rise to a positive CTE for the lattice. Conversely, if the constituent with the higher CTE is on its convex side, an increase in temperature will cause the rib to curve more and become shorter, giving rise to a negative CTE for the lattice. Both lattices in fig. 1.1 have isotropic CTEs; however, the right lattice has anisotropic elastic properties. Later in Lakes (2007), an effective Young's modulus of the lattice was determined and its relation to thermal expansion was found. In Lehman and Lakes (2013), optimality conditions for rib cross section were considered. Three lattices designed using a topology optimization procedure developed by Sigmund

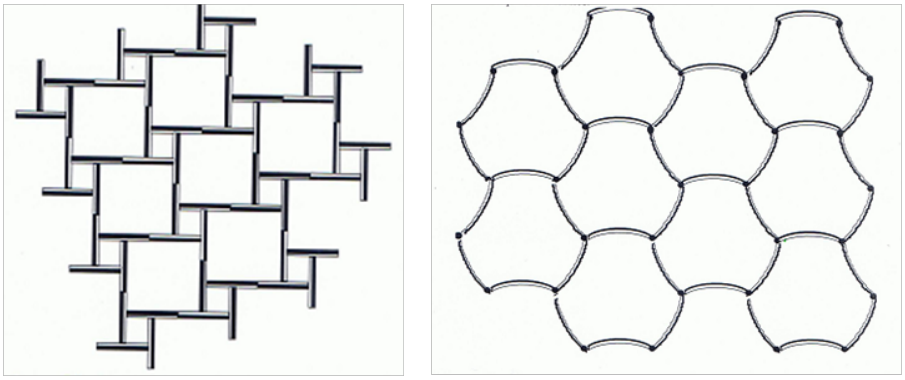

Figure 1.1: Lattices with isotropic CTE consisting of bi-material ribs presented Lakes (1996). The lattice on the right with curved ribs has larger CTE compared to the lattice with straight ribs on the left.

and Torquato (1996, 1997) are presented in fig. 1.2. Tight bounds on the effective thermal

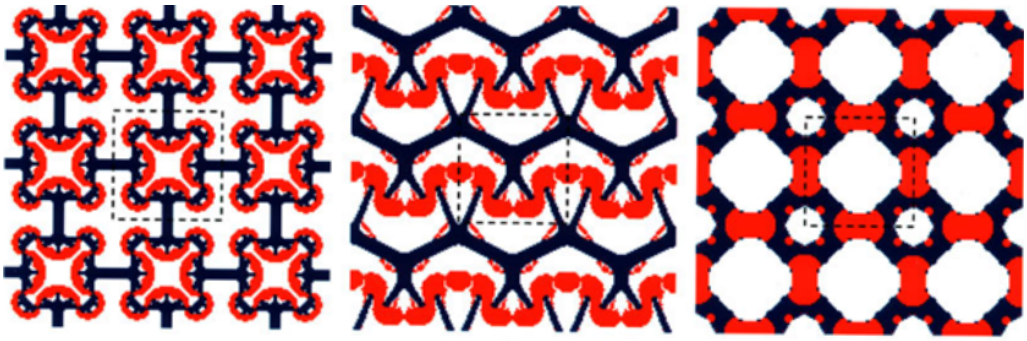

Figure 1.2: Isotropic lattices designed by Sigmund and Torquato (1996); Sigmund and Torquato (1997) using topology optimization. Red is a material with high CTE, black is a material with low CTE, and white is for empty space.

expansion coefficients of isotropic planar three-phase system were obtained in Gibiansky

and Torquato (1997). These bounds can be applied to a bimaterial lattice with the first and the second phases representing lattice materials and the third phase for void space.

A lattice cell based on an equilateral triangle and consisting of a skewed triangle of low CTE material surrounding a triangle of high CTE material combines high stiffness, simple shape, and the ability to attain a desirable CTE (Steeves et al., 2007) (Fig 1.3). Steeves et al. (2007) and Berger et al. (2011) showed that a pin-jointed lattice consisting of these cells is nearly optimally stiff: the mechanical response of this type of lattice is dominated by stretching rather than bending. Such lattices are structurally robust and can be relatively easily manufactured.

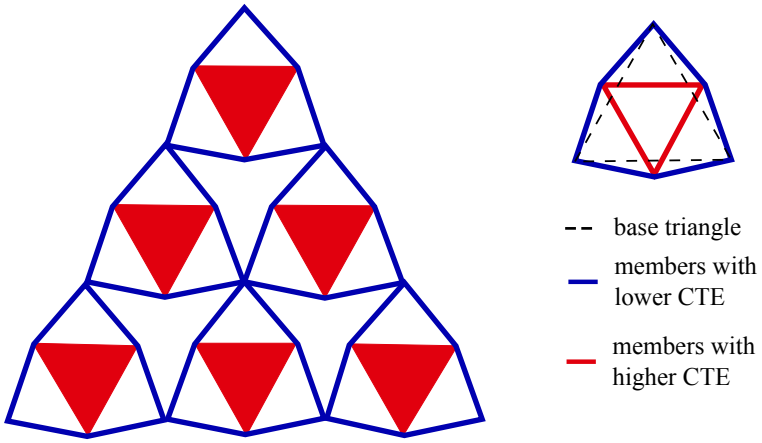

Figure 1.3: Llattice with isotropic CTE designed by Steeves et al. (2007). Each cell is based on equilateral triangle. The members with higher CTE are red, while the members with lower CTE are blue.

Thermally stable bimaterial lattices consisting of the cells suggested by Steeves et al. (2007) were designed, fabricated and tested in Gdoutos et al. (2013). These structures were tuned by varying the CTE of the constituent materials and the unit cell geometry. The micro-scale unit cells were composed of aluminum and titanium and were assembled over a large area to create thin low-CTE foils. A continuous honeycomb-like structure with cell inserts made of material with larger CTE than the cell contours (Jefferson et al., 2009) is shown in fig. 1.4.

In this work, anisotropic lattices consisting of anisotropic cells are designed. Each cell can have three different CTEs in different directions, and the values of the CTEs are determined from the kinematic conditions imposed on the lattice vertices (Toropova and Steeves, 2013a,b, 2014a,b,c, 2015c).

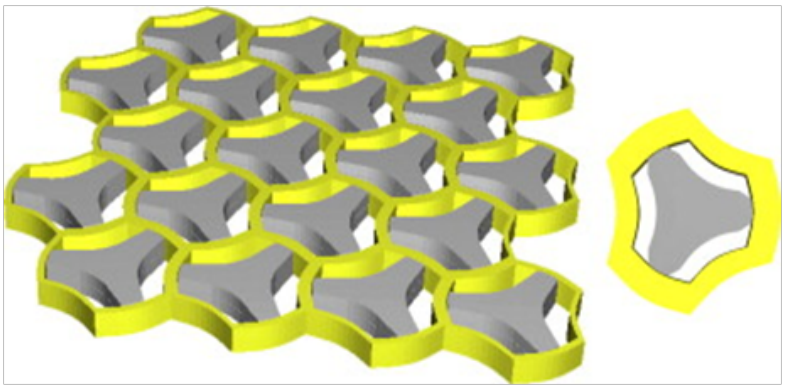

Figure 1.4: Lattice by Jefferson et al. (2009)

1.3 Thermal adapters

Often structures that are used in aerospace, civil engineering and microelectronics experience large cyclic temperature changes. For example, lightweight space systems such as precision satellite structures are exposed to thermal cycling as they pass between direct sunlight and the Earth's shadow (Jassemi-Zargani and Simard, 1999). If connected components of such structures are made of materials with different coefficients of thermal expansion (CTE), they experience mechanical stresses due to thermal expansion mismatch. To mitigate or eliminate thermal stresses, the parts of the structure with differing CTEs, herein referred to as the substrates, can be connected to each other through special transition elements or adapters with anisotropic CTE.

Using composite structures with graded CTEs for joining purposes is not a new concept. For example, Yousefiani et al. (2009a,b) applied it to design a layered injector-chamber attachment component in rocket engines (fig. 1.5). The authors suggested joining approaches such as welding, brazing, or solid state bonding to produce a graded-CTE composite with contoured profile layers (coloured parts in fig. 1.5(a)). In addition, Yousefiani et al. (2009b) used build-up (bottom-up) fabrication approaches such as metal deposition or powder metallurgy to produce a graded-CTE layered composite preform, which was consolidated and heat treated to create the graded-CTE integrated composite billet of near net shape. In Dang (2006), the composite adapters with graded CTE were components of a precision optical assembly to prevent lens misalignment. The adapters are depicted in fig. 1.6 as red rings. The adapter material comprised multiple thin composite material layers, each possessing a CTE slightly different from its two adjacent layers, bonded to form an adapter with CTE gradually varying in the direction perpendicular to the bonding interfaces. Such adapters will bend when subjected to temperature changes,

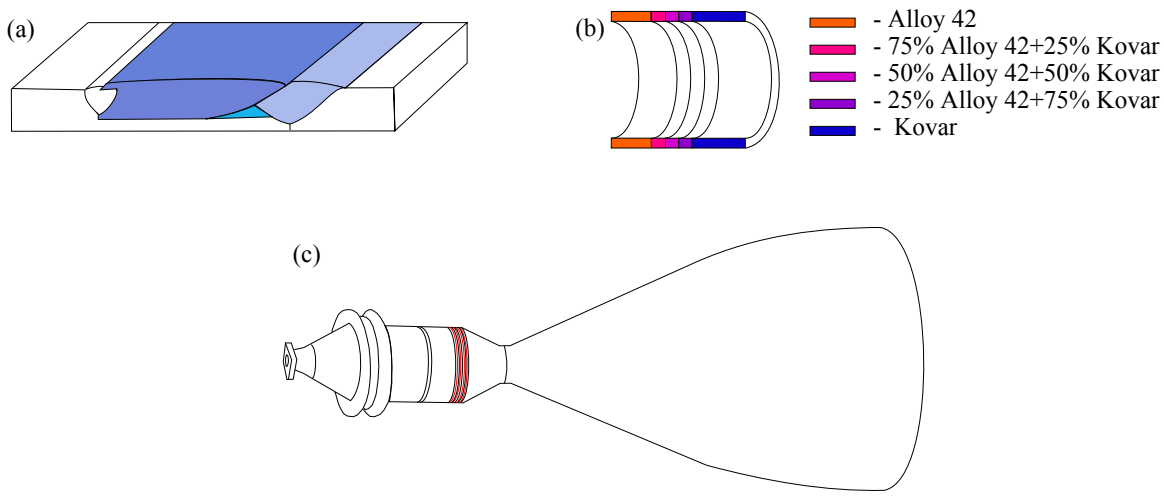

Figure 1.5: Composite adapters (Yousefiani et al., 2009a,b). (a) Composite plate with contoured profile layers having graded CTE. (b) Section view of the layered composite transition ring with graded CTE. (c) Assembled rocket engine structure with transition ring (red).

and deformations of the system must be permitted or thermal stresses will arise if the bending is suppressed. Also, their mechanical properties can be markedly anisotropic leading to the reduction of overall stiffness and strength. An alternative to graded systems is a compliant system, where differential thermal expansion is accommodated by connectors with low stiffness. This has the disadvantage of reducing the overall stiffness of the structure.

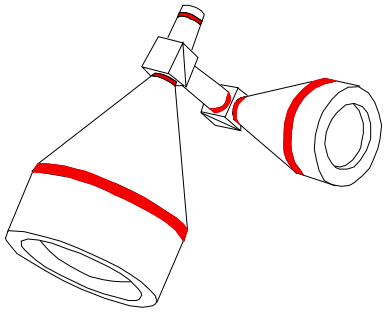

Figure 1.6: Composite adapters by Dang (2006) with graded CTE (red rings) to prevent lens misalignment in precision optical assembly.

In the present work, we suggest a method for connecting dissimilar parts of a structure using planar composite lattices with anisotropic CTE: one edge of the lattice has CTE

that matches the material of the first substrate and the opposite edge of the lattice has a CTE matching the second substrate. The lattice concept created by Steeves et al. (2007) is used to design a lattice adapter with anisotropic CTE. To be anisotropically tunable, each cell can have six different skew angles that provide anisotropic thermal expansion. Also, the cells in the lattice are not identical. As a result, the whole lattice has anisotropic and graded net CTE. The anisotropic thermal expansion of the lattice is analyzed and the equations connecting the cell skew angles with CTE in three directions are derived (Toropova and Steeves, 2013a,b, 2014a,b,c, 2015c). These equations are used to find desirable skew angles for the design of each cell. Then, the design of the whole lattice is performed: three CTEs in each cell are expressed as functions of the CTEs of the substrates. A system for choosing the lattice materials that can provide such CTEs is discussed. Design examples then show how the choice of materials influences the skewness of the cells. This anisotropic lattice concept eliminates both of the problems with other adapter concepts: the lattice remains stiff at all times and, if pin-connected, differential thermal deformations of the substrates are accommodated without generating any thermal stresses either in the lattice or the substrates. Moreover, the anisotropic lattices presented here are scale independent and can be extended to three-dimensional geometries.

1.4 Actuation and shape control

Actuators or intelligent structure technology are widespread in the aerospace, construction, automotive, and machine tool industries (Crawley, 1994). In the review by Irschik (2002), different effects that can be used for actuation are indicated: thermal expansion strains, plastic misfit strains, piezoelectric and piezothermoelectric effects, electrostrictive and electrorheological effects, the effect of pre-stress in structures, and shape memory alloys. A later review by Tzou (1998) describes how active materials including piezoelectrics, electro- and magnetostrictive materials, shape memory alloys, electro- and magnetorheological fluids, polyelectrolyte gels, superconductors, pyroelectrics, photostrictive materials, photoferroelectrics, and magnetooptical materials are used in transducers (sensors/actuators), precision mechatronic systems, and structronic systems. Applications of piezothermoelasticity to smart composite structures are presented in Tauchert et al. (2000). Electro-thermo-mechanical coupling in actuation and shape control systems is studied in Krommer (2000); Krommer and Irschik (2000). In Lee (1990); Lee and Moon (1990), shaped piezoelectric layers are developed and experimentally implemented to excite a specific structural vibrational mode. Piezoceramic composites are considered

for shape control of an antenna reflector by Herold-Schmidt et al. (1996). In Korkmaz (2011), it is indicated that active control is very efficient in tensegrity structures because of their high structural efficiency, i.e. strength-to-weight ratio and high precision control. The possibility of active control of tensegrity systems was originally considered by Djouadi et al. (1998); Oppenheim and Williams (1997); Skelton and de Olivera (2009) and later developed by Skelton et al. (2000) and Liedl et al. (2010). Shape morphing truss-like structures such as tensegrity masts and booms are considered and analyzed by Puig et al. (2010). An active element in a truss structure for use in precision control of large space structures such as orbiting interferometers and segmented mirror telescopes is described by Anderson et al. (1990). It includes an eddy current displacement sensor and an actuator that exploits either piezoelectricity or electrostriction to provide strain due to an electrical input. A compliant cellular truss with tendons used as active elements was suggested by Ramrkahyani et al. (2005) for aircraft structural morphing.

The works cited above describe the range of problems related to actuation and shape control: actuator design, a choice of compliant mechanism, material selection, structural efficiency, and coupling of different effects involved in actuation. These problems can be solved using thermal actuation and tuning that are based on conversion of thermal energy into mechanical movement due to thermal expansion. The solutions to thermally driven actuators are simple, do not need compliant mechanisms, and their industrial implementation is relatively inexpensive. The most common example of thermal actuation is presented by layered composite materials consisting of two and more components with different CTEs (Timoshenko, 1925). A bimetallic strip is a classical example of such a structure (fig. 1.7). This idea was exploited by Haftka and Adelman (1985) where heat-

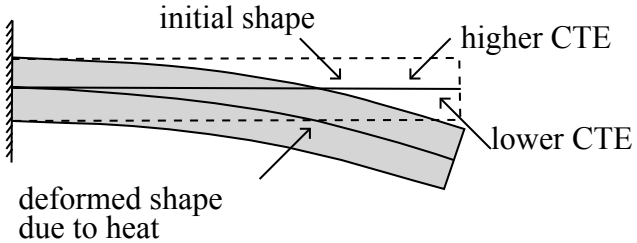

Figure 1.7: Bimetallic strip actuated by temperature.

ing was applied through control elements which had much higher CTE than the main structure. The thermal expansions in control elements caused desirable displacements in flexible space antennas. Generalization of the results was made by Irschik and Pichler (2001) for three-dimensional dynamic shape control problem.

With time, thermal actuators have become more complicated with asymmetric lamination, embedded heat sources (Sehr et al., 2001; Shen and Chen, 2013), carbon fiber reinforced plastics (CFRP) as materials with low CTE (Asanuma et al., 2002) (fig. 1.8), functionally graded materials (Sepiani et al., 2009), etc. The main problem with these

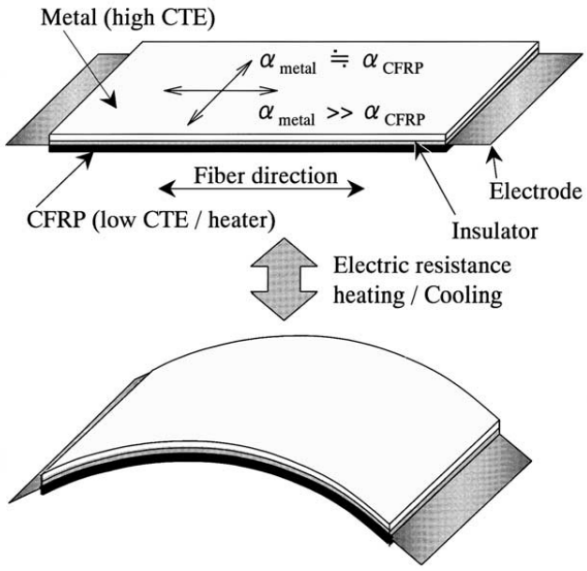

Figure 1.8: Active composite laminate and its actuation (Asanuma et al. (2002)). The upper metal layer of the laminate has CTE α_{metal}, while the lower layer made of unidirectional carbon fiber reinforced plastics (CFRP) has CTE α_{CFRP}. In fiber direction α_{metal} is much higher than α_{CFRP}, but in the transverse direction α_{metal} and α_{CFRP} are close to each other. Heating through the electrode that is between the metal and the CFRP layers actuates the laminate in fiber direction.

actuators is their small deformations. To amplify them, thermal buckling (Lisec et al., 1996; McCarthy et al., 2007; Wittwer et al., 2006) and shape memory alloys can be used.

There is a comparatively large number of publications devoted to thermal microactuators. For example, some electrothermal and thermomechanical actuators are designed, studied, and optimized by Chen and Culpepper (2006); Geisberger et al. (2003); Huang and Lee (1999); Jungen et al. (2006); Lee and Wu (2005); Michael et al. (2008); Que et al. (2001); Shimamura et al. (2006). The possibility of developing MEMS thermal actuators that can be activated with an external heat source was studied by Varona et al. (2007). The design and fabrication of a novel micromirror actuation system consisting of two paralleled bimorph actuators that bend in opposite directions for rotational control of the micromirror, was reported by Kim et al. (2010). An electrothermal microgripper was designed and simulated by Kaur et al. (2013). Thermal actuation with electrical heating applied to deformable mirrors was reported by Vdovin and Loktev (2002) and

later by Huang et al. (2015) where thermoelectric coolers provided upward and downward surface control. An incandescent lamp was used for heating a thermally driven adaptive mirror by Michel et al. (2004). The silicone elastomer material Sylgard 184 with large CTE of 310 ppm/°C was used by Reinert and Luthy (2005) for thermo-optical actuation of adaptive mirrors.

In the work presented here, we perform shape control and thermal actuation using anisotropic bimaterial lattices. Their structure allows us to design them with desirable CTEs not only along the sides of the base triangle but in any direction. For example, fine tuning of optical lenses can be achieved through a bimaterial lattice forming a polygonal ring connector with cells extending along their heights. The idea of using large negative and positive lattice CTEs along the cell heights was applied to the design of thermal actuators (Toropova and Steeves, 2015a,b). For this, two types of cells with negative and positive CTEs along their heights were used. If the material of the internal triangle has a CTE larger than the CTE of an external hexagon, such a cell has negative CTE along its height. If the material of the internal triangle has a CTE less than the CTE of an external hexagon, the cell behaves conversely. By combining cells in different configurations, we design several actuators - a switch, tweezers, and a valve. Amplification of displacements was achieved by the use of lattice materials with a large ratio of their CTEs and nonequilateral base triangles for cells. In terms of overall performance, the actuators are slow but do not depend on their thermal history, i.e. they do not exhibit hysteresis. The forces and deflections they achieve compare favorably with piezoelectrics and SMAs.

The thesis is organized in 6 chapters. In Chapter 2, adaptive anisotropic bimaterial lattices to eliminate thermal expansion mismatch stresses between two substrates with different CTEs are designed. Cells of the lattices are based on equilateral triangle. The influence of a cell material choice on the overall lattice shape is demonstrated by several examples. A general algorithm of lattices design is elaborated. Adaptive lattices of more complicated configuration with cells based on nonequilateral triangles are considered in Chapter 3. Also, a general algorithm of the increase of lattice structural efficiency is presented in this chapter. Bimaterial lattices as mechanisms for fine tuning or thermal actuation are considered in Chapter 4. Thermally driven a switch, tweezers, and a valve are designed. Two different types of cells are used providing desirable negative or positive deflections of lattice vertices. In Chapter 5, the experimental methodology used in this research is described, and experimentally measured cell CTEs are compared with analytically predicted values. In Chapter 6, structural analysis of lattice cells using rod finite elements for pin-jointed cells and frame finite elements for cells with rigid joints

accounting for the cross sectional area of cell members is performed. In the last chapter with Conclusions, the main contributions of the research work are highlighted and the avenues for the future work are outlined.

To date, the work contained in this thesis has been published in six conference papers and three peer reviewed journal papers.

Conference papers:

M. M. Toropova and C. A. Steeves. Composite Lattices With Anisotropic Coefficient of Thermal Expansion, Proceedings of the 60th CASI Aeronautics Conference and AGM,Toronto, Ontario, April 30-May 2, 2013.

M. M. Toropova and C. A. Steeves. Composite Lattices with Anisotropic Coefficient of Thermal Expansion, Proceedings of the 4th Canadian Conference on Nonlinear Solid Mechanics (CanCNSM 2013) McGill University, Montreal, Canada, July 23-26, 2013.

M. M. Toropova and C. A. Steeves. Design of composite bi-material lattice adapters, Proceedings of the 1st International Conference on Mechanics of Composites , Stony Brook University, USA, June 8-12, 2014.

M. M. Toropova and C. A. Steeves. Adaptive bi-material lattices to mitigate thermal expansion mismatch in satellite structures, Proceedings of the 65th International Astronautical Congress, Toronto, Canada, September 29 October 3, 2014.

M. M. Toropova and C. A. Steeves. Controlling thermal deformation through the use of lattice structures, Proceedings of the 62nd CASI Aeronautics Conference and AGM 3rd CARDN Conference, Montreal, Canada, May 19-21, 2015.

M. M. Toropova and C. A. Steeves. Thermal Actuation Through Bimaterial Lattices, Proceedings of ASME Conference on Smart Materials, Adaptive Structures and Intelligent Systems SMASIS, Colorado Springs, USA, September 21-23, 2015.

Journal papers:

M. M. Toropova and C. A. Steeves. Bimaterial lattices with anisotropic thermal expansion, *Journal of Mechanics of Materials and Structures*, v. 9, N 2, 227-244, 2014.

M. M. Toropova and C. A. Steeves. Adaptive bimaterial lattices to mitigate thermal expansion mismatch stresses in satellite structures, *Acta Astronautica*, v. 113, 132-141, 2015.

M. M. Toropova and C. A. Steeves. Bimaterial lattices as thermal adapters and actuators, *Smart Materials and Structures*, 2016, accepted for publication.

Chapter 2

One-row adaptive bimaterial lattices

In this chapter, the fundamental concepts and models of anisotropic lattices will be developed [1] [2]. These represent a significant conceptual departure from Steeves et al. (2007), which was restricted to isotropic systems. Anisotropy enables a much wider range of desirable behaviours which will be elucidated through the course of this thesis. Because each cell can have six different skew angles (fig. 2.1), tailored anisotropic thermal expansion is enabled. Also, the cells in the lattice are not identical. As a result, the whole lattice has varying gradually anisotropic thermal expansion that is tunable as a graded net. To analyze the anisotropic thermal expansion of the whole lattice, the equations connecting the cell skew angles with CTE in three directions are derived. These equations are used to find desirable skew angles for the design of each cell. Then, the design of the whole lattice is performed: three CTEs in each cell are found as functions of the CTEs of the substrates. A system for choosing the lattice materials that can provide such CTEs is discussed. Design examples then show how the choice of materials influences the skewness of the cells. This anisotropic lattice concept eliminates both of the problems with other adapter concepts: the lattice remains stiff at all times and, if pin-connected, differential thermal deformations of the substrates are accommodated without generating any thermal stresses either in the lattice or the substrates. Moreover, the anisotropic lattices presented here are scale independent.

[1] M MToropova and C A Steeves. Composite lattices with anisotropic coefficient of thermal expansion. The 4th Canadian Conference on Nonlinear Solid Mechanics (CanCNSM 2013) McGill University, Montreal, Canada, July 23-26, 2013.

[2] M M Toropova and C A Steeves. Bimaterial lattices with anisotropic thermal expansion. Journal of Mechanics of Materials and Structures, 9(2):227-244, 2014.

2.1 Formulation of the problem

Consider two adjoining planar parts of a structure; name them substrate 1 and substrate 2. Suppose that substrates 1 and 2 are made of materials with different CTEs, A_1 and A_2, respectively. We would like to join these plates by a planar interfacial one-row lattice that has the CTE of the first substrate A_1 on the edge connected to the first plate and the CTE of the second substrate A_2 on the edge adjacent to the second plate; this eliminates thermal stresses in the substrates during thermal excursions. In addition, the lattice itself should experience no internal thermal stresses during temperature changes. For this purpose, the lattice with cells described by Steeves et al. (2007) is used; it is based on a virtual triangle ACE and consists of an irregular hexagon $ABCDEF$ made of a material with lower CTE α_1 and connected with an internal triangle BDF made of a material with higher CTE α_2 (fig. 2.1). The internal triangle BDF is pin-connected to the hexagon. In such a cell, the members of the hexagon rotate with increasing temperature and accommodate the overall cell expansion Evans et al. (1998). Adjacent cells of the lattice, connected at A, C and E, also have pin-joints between each other and with the substrates (fig. 2.2), such that the whole structure is free of bending and thermal expansion mismatch stresses.

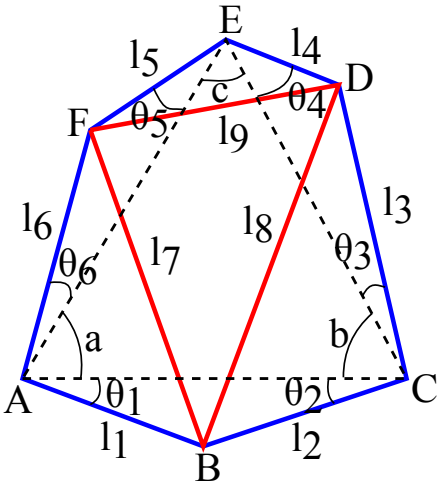

Figure 2.1: One cell of a lattice. The members AB, BC, CD, DE, EF, and AF have lower CTE, depicted in blue. The members BD, DF, BF have higher CTE, depicted in red. The equilateral triangle ACE upon which the cell is based is shown as a dashed line. The skew angles, θ_1, θ_2, θ_3, θ_4, θ_5, θ_6, are the angles by which the unit cell strut orientation differ from those of an equilateral triangle.

When temperature changes, the lengths of all members $l_1 = AB$, $l_2 = BC$, $l_3 = CD$, $l_4 = DE$, $l_5 = EF$, and $l_6 = AF$, $l_7 = FB$, $l_8 = BD$, $l_9 = FD$, have an increment dl_i,

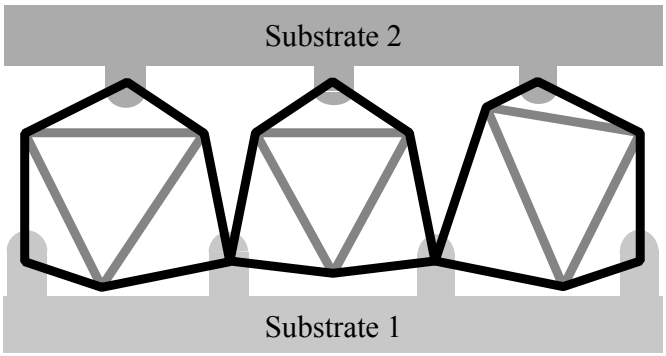

Figure 2.2: A planar anisotropic lattice connecting two substrates with different coefficients of thermal expansion. The lattice has net anisotropic thermal expansion, and each individual cell has net anisotropic thermal expansion.

$dl_i = l_i\alpha_1 dT$, $i = (\overline{1,6})$ and $dl_i = l_i\alpha_2 dT$, $i = (\overline{7,9})$. As a result, the distances $AC = L_1$, $CE = L_2$, $AE = L_3$ also change: $dL_1 = \overline{\alpha}_1 L_1 dT$, $dL_2 = \overline{\alpha}_2 L_2 dT$, $dL_3 = \overline{\alpha}_3 L_3 dT$, where T is temperature and $\overline{\alpha}_i$, $i = 1, 2, 3$ are the CTEs of the cell along AC, CE, and AE, respectively. However, the members of the internal triangle extend with different CTE compared to the members of the hexagon, which leads to their rotation and a change in the skew angles $d\theta_j$, $j = (\overline{1,6})$ (fig. 2.3). Because the skew angles can be independent, the three CTEs of a cell $\overline{\alpha}_i$, $i = 1, 2, 3$ can be different. Thus, the cell can be designed to have anisotropic thermal expansion.

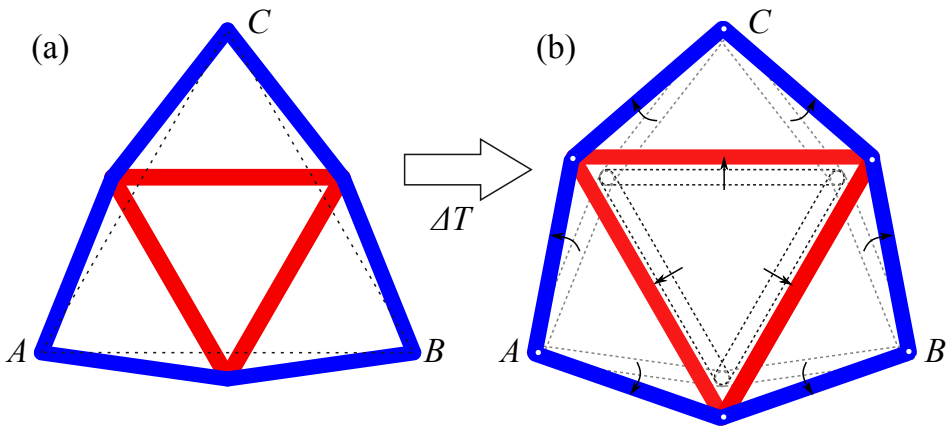

Figure 2.3: Sketch of the kinematics of the thermal expansion of a symmetric bimaterial lattice cell. This unit cell has isotropic thermal expansion behaviour. The dotted lines in the right figure show the initial location of the members. As temperature increases, all the members expand, but because the red members expand more, they push the blue members outward, causing them to rotate. This rotation accommodates their expansion.

By choosing the angles θ_i, $i = 1, 2, 3, 4, 5, 6$, we can influence the change of dL_1, dL_2,

dL_3 in each cell and provide different changes of distances between vertices of the cells and hence different CTEs on the bottom and top levels of the lattice (fig. 2.4). To design such a lattice, relations between CTEs $\overline{\alpha}_i, i = 1, 2, 3$ and angles $\theta_j, j = 1, 2, 3, 4, 5, 6$ have to be obtained.

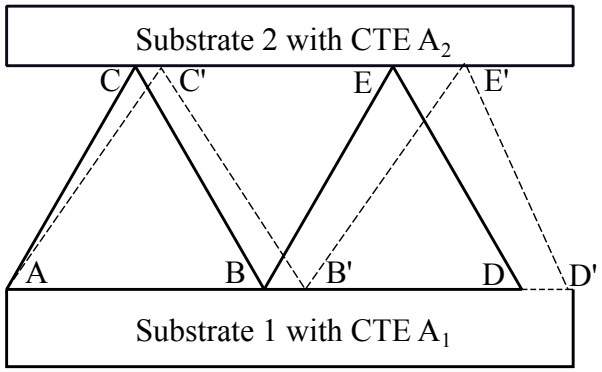

Figure 2.4: Lattice design: base equilateral triangles of two cells. During thermal expansion, the original points translate from, for example, B to B'. The lattice cells must be designed to accommodate the changing distances between the points.

2.2 General formulae

The undeformed lengths of the constituent members of a cell (fig. 2.1) are:

$$\begin{aligned} &l_1 = L_1 f_1(\theta_1, \theta_2), \qquad l_2 = L_1 f_2(\theta_1, \theta_2), \qquad l_3 = L_2 f_3(\theta_3, \theta_4), \\ &l_4 = L_2 f_4(\theta_3, \theta_4), \qquad l_5 = L_3 f_5(\theta_5, \theta_6), \qquad l_6 = L_3 f_6(\theta_5, \theta_6), \end{aligned} \tag{2.1}$$

where

$$\begin{aligned} &f_1 = \frac{\sin\theta_2}{\sin(\theta_1+\theta_2)}, \qquad f_2 = \frac{\sin\theta_1}{\sin(\theta_1+\theta_2)}, \qquad f_3 = \frac{\sin\theta_4}{\sin(\theta_3+\theta_4)}, \\ &f_4 = \frac{\sin\theta_3}{\sin(\theta_3+\theta_4)}, \qquad f_5 = \frac{\sin\theta_6}{\sin(\theta_5+\theta_6)}, \qquad f_6 = \frac{\sin\theta_5}{\sin(\theta_5+\theta_6)}. \end{aligned}$$

From (2.1), the differential relations are obtained:

$$\begin{aligned} &\frac{1}{L}dl_1(1-\frac{\overline{\alpha}_1}{\alpha_1}) = f'_{1_{\theta_1}}d\theta_1 + f'_{1_{\theta_2}}d\theta_2, \quad \frac{1}{L}dl_2(1-\frac{\overline{\alpha}_1}{\alpha_1}) = f'_{2_{\theta_1}}d\theta_1 + f'_{2_{\theta_2}}d\theta_2, \\ &\frac{1}{L}dl_3(1-\frac{\overline{\alpha}_2}{\alpha_1}) = f'_{3_{\theta_3}}d\theta_3 + f'_{3_{\theta_4}}d\theta_4, \quad \frac{1}{L}dl_4(1-\frac{\overline{\alpha}_2}{\alpha_1}) = f'_{4_{\theta_3}}d\theta_3 + f'_{4_{\theta_4}}d\theta_4, \\ &\frac{1}{L}dl_5(1-\frac{\overline{\alpha}_3}{\alpha_1}) = f'_{5_{\theta_5}}d\theta_5 + f'_{5_{\theta_6}}d\theta_6, \quad \frac{1}{L}dl_6(1-\frac{\overline{\alpha}_3}{\alpha_1}) = f'_{6_{\theta_5}}d\theta_5 + f'_{6_{\theta_6}}d\theta_6. \end{aligned} \tag{2.2}$$

where $f'_{i_{\theta_j}}$, $i, j = 1, 2, 3, 4, 5, 6$ is a partial derivative of the function f_i with respect to the angle θ_j.

The length of three members of the internal triangle can be expressed as:

$$\begin{aligned} FB = l_7 &= (L_1^2 f_1^2 + L_3^2 f_6^2 - 2L_1 L_3 f_1 f_6 \cos A')^{1/2}, \\ BD = l_8 &= (L_1^2 f_2^2 + L_2^2 f_3^2 - 2L_1 L_2 f_2 f_3 \cos B')^{1/2}, \\ DF = l_9 &= (L_2^2 f_4^2 + L_3^2 f_5^2 - 2L_2 L_3 f_4 f_5 \cos C')^{1/2}, \end{aligned} \tag{2.3}$$

$$A' = \theta_1 + \theta_6 + a, \qquad B' = \theta_2 + \theta_3 + b, \qquad C' = \theta_4 + \theta_5 + c$$

where a, b, c are the angles in the base triangle ACE (fig. 2.1). From (2.3), the following relations are found

$$\begin{aligned} l_7 dl_7 &= (l_1 - l_6 \cos A')dl_1 + (l_6 - l_1 \cos A')dl_6 + l_1 l_6 \sin(A'(d\theta_1 + d\theta_6 + da), \\ l_8 dl_8 &= (l_2 - l_3 \cos B')dl_2 + (l_3 - l_2 \cos B')dl_3 + l_2 l_3 \sin(B'(d\theta_2 + d\theta_3 + db), \\ l_9 dl_9 &= (l_4 - l_5 \cos C')dl_4 + (l_5 - l_4 \cos C')dl_5 + l_4 l_5 \sin(C'(d\theta_4 + d\theta_5 + dc). \end{aligned} \tag{2.4}$$

where da, db, and dc are the differentials of the angles in the base triangle that change when temperature changes (fig. 2.4).

In this chapter, it is assumed that the triangle ACE is equilateral : $L_1 = L_2 = L_3 = L$ and $\angle a = \angle b = \angle c = 60°$ and the skew angles adjacent to the same side of the base triangle are equal to each other, i.e., $\theta_1 = \theta_2 = t_1$, $\theta_3 = \theta_4 = t_2$, $\theta_5 = \theta_6 = t_3$ (fig. 2.5). So, from (2.2), we can obtain

$$\begin{aligned} dt_1 &= (\alpha_1 - \overline{\alpha}_1) \cot t_1 dT, \\ dt_2 &= (\alpha_1 - \overline{\alpha}_2) \cot t_2 dT, \\ dt_3 &= (\alpha_1 - \overline{\alpha}_3) \cot t_3 dT. \end{aligned} \tag{2.5}$$

To obtain da, db, dc, the relations

$$L_2 = L_1 \frac{\sin a}{\sin(a+b)}, \quad L_3 = L_1 \frac{\sin b}{\sin(a+b)}$$

are used, from which the derivatives dL_2 and dl_3 can be found as

$$\begin{aligned} dL_2 &= dL_1 \frac{\sin a}{\sin(a+b)} + L_1 \left(\frac{\cos a}{\sin(a+b)} da - \frac{\sin a \cos(a+b)}{\sin(a+b)^2} (da + db) \right), \\ dL_3 &= dL_1 \frac{\sin b}{\sin(a+b)} + L_1 \left(\frac{\cos b}{\sin(a+b)} db - \frac{\sin b \cos(a+b)}{\sin(a+b)^2} (da + db) \right). \end{aligned}$$

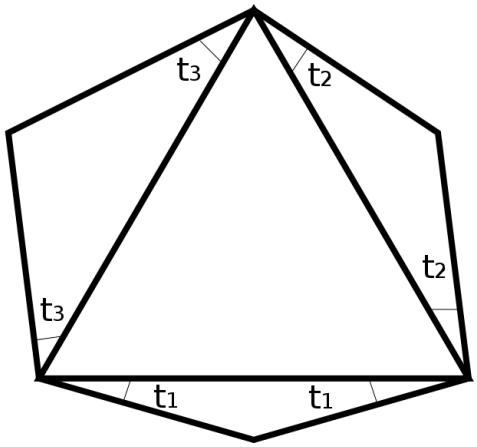

Figure 2.5: A cell with three independent skew angles. The original six skew angles are replaced by $\theta_1 = \theta_2 = t_1$, $\theta_3 = \theta_4 = t_2$, $\theta_5 = \theta_6 = t_3$.

From these equations, da, db, and dc can be expressed through $dL_1 = L_1\overline{\alpha}_1 dT$, $dL_2 = L_2\overline{\alpha}_2 dT$, and $dL_3 = L_3\overline{\alpha}_3 dT$ as:

$$\begin{aligned} da &= \frac{dT}{\sin b}\left(\frac{L_3}{L_1}\overline{\alpha}_3\cos(a+b) + \frac{L_2}{L_1}\overline{\alpha}_2 - \cos b\ \overline{\alpha}_1\right), \\ db &= \frac{dT}{\sin a}\left(\frac{L_2}{L_1}\overline{\alpha}_2\cos(a+b) + \frac{L_3}{L_1}\overline{\alpha}_3 - \cos a\ \overline{\alpha}_1\right), \\ dc &= -da - db. \end{aligned} \tag{2.6}$$

Substituting (2.5) and (2.6) into (2.4) and performing all necessary transformations, three nonlinear equations linking the three skew angles t_i, with the three normalized thermal expansion coefficients along the lines AC, CE, and AE in the skewed triangle are obtained:

$$\begin{aligned} -\frac{\overline{\alpha}_1}{\alpha_1}(\cot t_1 + \cot b) + \frac{\overline{\alpha}_2}{\alpha_1}\frac{1}{\sin b} + \frac{\overline{\alpha}_3}{\alpha_1}\left(\frac{\cos(a+b)}{\sin b} - \cot t_3\right) = \\ \frac{1}{\sin A'}(\frac{\alpha_2}{\alpha_1} - 1)(\frac{\cos t_3}{\cos t_1} + \frac{\cos t_1}{\cos t_3} - 2\cos A') - \cot t_1 - \cot t_3, \\ -\frac{\overline{\alpha}_1}{\alpha_1}(\cot t_1 + \cot a) + \frac{\overline{\alpha}_2}{\alpha_1}\left(\frac{\cos(a+b)}{\sin a} - \cot t_2\right) + \frac{\overline{\alpha}_3}{\alpha_1}\frac{1}{\sin a} = \\ \frac{1}{\sin B'}(\frac{\alpha_2}{\alpha_1} - 1)(\frac{\cos t_2}{\cos t_1} + \frac{\cos t_1}{\cos t_2} - 2\cos B') - \cot t_1 - \cot t_2, \\ \frac{\overline{\alpha}_1}{\alpha_1}(\cot a + \cot b) - \frac{\overline{\alpha}_2}{\alpha_1}\left(\frac{\cot b\sin(a+b)}{\sin a} + \cot t_2\right) - \frac{\overline{\alpha}_3}{\alpha_1}\left(\frac{\cot a\sin(a+b)}{\sin b} + \cot t_3\right) = \\ \frac{1}{\sin C'}(\frac{\alpha_2}{\alpha_1} - 1)(\frac{\cos t_3}{\cos t_2} + \frac{\cos t_2}{\cos t_3} - 2\cos C') - \cot t_2 - \cot t_3, \end{aligned} \tag{2.7}$$

The equations (2.7) are scale independent, contain the ratio α_2/α_1 as a parameter, and couple three normalized CTEs in a cell $\overline{\alpha}_1/\alpha_1$, $\overline{\alpha}_2/\alpha_1$, and $\overline{\alpha}_3/\alpha_1$. If the skew angles are known, these three CTEs can be calculated using the following formulae:

$$\frac{\overline{\alpha}_1}{\alpha_1} = \frac{\Delta_1}{\Delta}, \quad \frac{\overline{\alpha}_2}{\alpha_1} = \frac{\Delta_2}{\Delta}, \quad \frac{\overline{\alpha}_3}{\alpha_1} = \frac{\Delta_3}{\Delta}$$

where

$$\begin{aligned}
\Delta &= c_{11}c_{22}c_{33} + c_{21}c_{32}c_{13} + c_{12}c_{23}c_{31},\\
\Delta_1 &= F_1(c_{22}c_{33} - c_{32}c_{23}) + F_2(c_{13}c_{32} - c_{12}c_{33}) - F_3(c_{22}c_{13} - c_{12}c_{23}),\\
\Delta_2 &= F_2(c_{11}c_{33} - c_{13}c_{31}) + F_3(c_{13}c_{21} - c_{11}c_{23} - F_1(c_{21}c_{33} - c_{31}c_{23}),\\
\Delta_3 &= F_3(c_{11}c_{22} - c_{21}c_{12}) + F_1(c_{21}c_{32} - c_{31}c_{22}) - F_2(c_{11}c_{32} - c_{31}c_{12}),
\end{aligned} \tag{2.8}$$

$$\begin{aligned}
c_{11} &= -\cot b - \cot t_1,\\
c_{12} &= \frac{1}{\sin b},\\
c_{13} &= \frac{\cos(a+b)}{\sin b} - \cot_3,\\
c_{21} &= -\cot a - \cot t_1,\\
c_{22} &= \frac{\cos(a+b)}{\sin a} - \cot t_2,\\
c_{23} &= \frac{1}{\sin a},\\
c_{31} &= \cot a + \cot b,\\
c_{32} &= -\cot t_2 - \cot b\frac{\sin(a+b)}{\sin a},\\
c_{33} &= -\cot t_3 - \cot a\frac{\sin(a+b)}{\sin b},
\end{aligned} \tag{2.9}$$

$$\begin{aligned}
F_1 &= -\frac{1}{\sin A''}(1 - \frac{\alpha_2}{\alpha_1})(\frac{\cos t_1}{\cos t_3} + \frac{\cos t_3}{\cos t_1} - 2\cos A'') - \cot t_1 - \cot t_3,\\
F_2 &= -\frac{1}{\sin B''}(1 - \frac{\alpha_2}{\alpha_1})(\frac{\cos t_1}{\cos t_2} + \frac{\cos t_2}{\cos t_1} - 2\cos B'') - \cot t_1 - \cot t_2,\\
F_3 &= -\frac{1}{\sin C''}(1 - \frac{\alpha_2}{\alpha_1})(\frac{\cos t_2}{\cos t_3} + \frac{\cos t_3}{\cos t_2} - 2\cos C'') - \cot t_2 - \cot t_3,
\end{aligned} \tag{2.10}$$

In designing anisotropic lattices, it is necessary to solve the inverse problem of finding

the skew angles when the values of three CTEs $\overline{\alpha}_1$, $\overline{\alpha}_2$, and $\overline{\alpha}_3$ in each cell are known. If a cell has only three different skew angles (this case is considered in this chapter), three equations are enough to solve the inverse problem. In mathematical sense, the solutions are combined from periodic functions and hence there are an infinite number of them, but after accounting for the practical restrictions on skew angles the solution can be considered unique.

From equation (2.7), it is seen that if any $t_i = 0$, $i = 1, 2, 3$, then $\overline{\alpha}_i = \alpha_1$, and the two other skew angles do not influence it. If all the skew angles in a cell with an equilateral base triangle are equal to θ, then the cell is isotropic with a constant coefficient of thermal expansion in all directions equal to $\overline{\alpha}$, and these three equations can be transformed into the equation for the expansion coefficient obtained by Steeves et al. (2007):

$$\frac{\overline{\alpha}}{\alpha_1} = \frac{1 - 0.5(\alpha_2/\alpha_1)\sin(2\theta)(1/\sqrt{3} + \tan\theta)}{1 - 0.5\sin(2\theta)(1/\sqrt{3} + \tan\theta)}. \tag{2.11}$$

The equation can be rewritten in more compact form

$$\frac{\overline{\alpha}}{\alpha_1} = 1 + (1 - \frac{\alpha_2}{\alpha_1})\tan\theta\tan(30^\circ + \theta).$$

In the isotropic configuration, the maximum of the function $\overline{\alpha}/\alpha_1$ is reached at $\theta = -15^\circ$; at $\theta > -15^\circ$ the function decreases (see fig. 2.6). To avoid cell overlapping, we consider skew angles in the range $[-15^\circ, 30^\circ]$ though if the skew angle is on the right or the left edges of the lattice it can be greater than 30°.

Based on the formulae (2.7), fig. 2.6 illustrates the coupling of three normalized CTEs $\overline{\alpha}_i/\alpha_1$, $i = 1, 2, 3$ in a cell composed of titanium alloy (Ti-6Al-4V Grade 5) and magnesium alloy (AZ81A type) at three different sets of values $t_1 = 30^\circ$, $t_2 = 20^\circ$; $t_1 = 15^\circ$, $t_2 = 20^\circ$; $t_1 = -5^\circ$, $t_2 = 20^\circ$ and the ratio $\alpha_2/\alpha_1 = 3.26$, which corresponds to the ratio of the CTEs of magnesium alloy (28 ppm/°C) and titanium alloy (8.6 ppm/°C). These materials are chosen to maximize the ratio of their CTEs. The curves in figure (2.6) show that coupling reduces the range of three cell CTEs that can satisfy the equations (2.7) compared to the isotropic case.

2.3 Lattice design

In this section, planar, one-row lattices are considered. We can design lattices by designating the points on the substrates to which the lattice will be attached, and following those points as the temperature changes. This will provide the changes in the lengths of

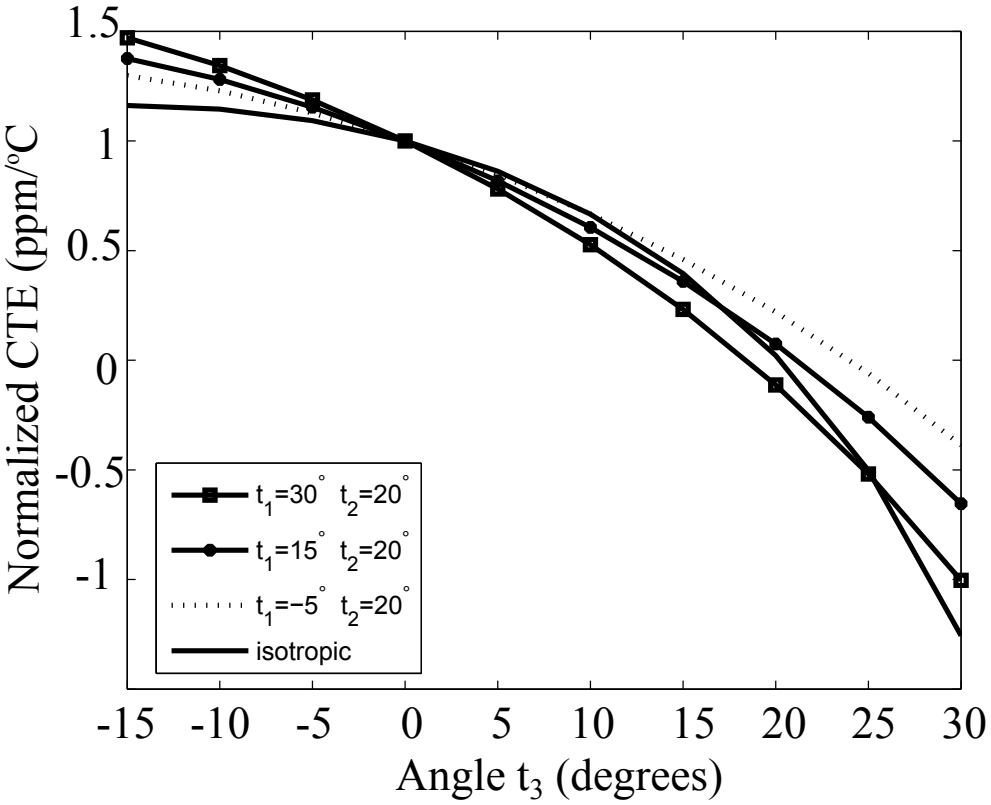

Figure 2.6: The influence of two skew angles on $\bar{\alpha_3}/\alpha_1$. $\alpha_2/\alpha_1 = 3.26$, which correspond to the ratio of the CTEs of magnesium alloy and titanium alloy.

the sides of the equilateral triangles upon which the lattice cells are based, to which the changing shapes of the lattice cells must be matched. For example, fig. 2.4 shows the base triangles of two cells. Suppose the point A is fixed. When the temperature changes, the other points B, C, D, E move to the positions B', C', D', E', respectively. The new distances AB', $B'D'$, $C'E'$ can be expressed in terms of the side length L and three unknown CTEs of each cell. The following four conditions on the shape of the lattice after temperature changes are sufficient to find three CTEs for each cell:

1. the distances between vertices connected to substrate 1 must be equal to $L(1 + A_1 dT)$;

2. the distances between vertices connected to substrate 2 must be equal to $L(1 + A_2 dT)$;

3. the distance between substrates, H, is fixed and independent of temperature; and

4. the lattice has a line of symmetry.

The third condition is arbitrary; here, constant H is chosen, although $\Delta H > 0$ and $\Delta H < 0$ may alternatively be selected without changing the overall process (Chapter 3 and 4).

Using these conditions and deriving formulae for $\overline{\alpha}_i$, $i = 1, 2, 3$, terms with $\overline{\alpha}_i^2$ are neglected (which is reasonable because $\overline{\alpha}_i$ are small, typically of magnitude 10^{-6}). As a result, the formulae for $\overline{\alpha}_1$, $\overline{\alpha}_2$, $\overline{\alpha}_3$ in each cell of two-cell, three-cell, and n-cell lattices as functions of the CTEs of substrates A_1 and A_2 are obtained.

To work with several cells, denote $\alpha_{i1} = \overline{\alpha}_1$, $\alpha_{i2} = \overline{\alpha}_2$, $\alpha_{i3} = \overline{\alpha}_3$, where i is the number of the cell in the row (the skeleton of a lattice is depicted in fig. 2.7). For example, $i = 1$ for cell ABC and $i = 2$ for BDE. Along AB and BD $j = 1$, along BC and DE $j = 2$, and along AC and BE $j = 3$. Consider a lattice consisting of two cells ABC

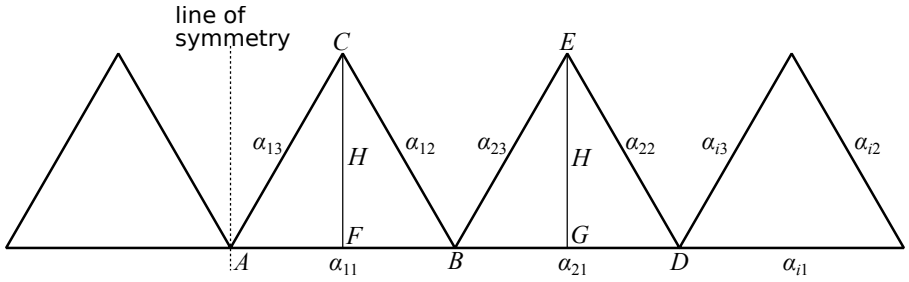

Figure 2.7: Designation of CTEs in a multi-cell lattice. Note that the lines do not represent actual cell members; these lines refer to the virtual equilateral triangles upon which the cells are based, shown in fig. 2.1 as dashed lines. The cell vertices are A to E, while the mid-points on the lower face of the cell are F and G. H is the height of the cells. If the lattice has a line of symmetry, it would exist as the dashed line with additional cells to the left.

and BDE (fig. 2.7). The lattice is pin-connected at A, B, and D to a substrate with CTE A_1 while at points C and E it is pin-connected to a substrate with CTE A_2. At the initial state $AB = BC = AC = BD = DE = BE = L$. When the temperature changes, the lengths of these segments become $L(1 + \alpha_{ij}dT)$. The first substrate and the bottom level of the lattice have the same CTE (condition 1), $\alpha_{11} = \alpha_{21} = A_1$. Similarly, when temperature changes, the distance between points C and E changes according to the formula $L(1 + A_2dT)$ (condition 2). Denote $FB = x$. Then, for the first cell:

$$L^2(1 + \alpha_{12}dT)^2 - x^2 = L^2(1 + \alpha_{13}dT)^2 - (L(1 + \alpha_{11}dT) - x)^2.$$

Neglecting terms with α_{ij}^2, the following relation is obtained

$$x = 0.5L(1 + (\alpha_{11} + 2\alpha_{12} - 2\alpha_{13})dT). \tag{2.12}$$

Using this formula, we can find from the second cell

$$BG = 0.5L(1 + (\alpha_{21} - 2\alpha_{22} + 2\alpha_{23})dT).$$

Thus, when the temperature changes, the distance between points C and E changes according to

$$CE = L(1 + (\alpha_{12} - \alpha_{13} - \alpha_{22} + \alpha_{23} + A_1)dT).$$

Hence,

$$A_2 = \alpha_{12} - \alpha_{13} - \alpha_{22} + \alpha_{23} + A_1.$$

Also, we would like to design a lattice that does not expand along FC and GE, so that the lattice cell height H remains constant when temperature changes (condition 3). Applying the approach used above, for the first cell, for example, it can be written:

$$(H + dH)^2 = L^2(1 + \alpha_{12}dT)^2 - 0.25L^2(1 + (2\alpha_{12} - 2\alpha_{13} + \alpha_{11})dT)^2 = \\ (0.5\sqrt{3}L(1 + 2/3(\alpha_{12} + \alpha_{13} - 0.5\alpha_{11})dT))^2.$$

Thus, the CTE along cells heights FC and GE is $\alpha_H = \frac{2}{3}(\alpha_{12} + \alpha_{13} - 0.5\alpha_{11})$. In this case,

$$\alpha_{12} + \alpha_{13} - 0.5\alpha_{11} = 0.$$

Finally, for more uniform deformation of the lattice, symmetry can be imposed through $\alpha_{12} = \alpha_{23}$ and $\alpha_{13} = \alpha_{22}$ (condition 4).

For a lattice consisting of two symmetric cells, three CTEs in each cell can be found as functions of the CTEs of the substrates:

$$\begin{aligned} \alpha_{11} &= \alpha_{21} = A_1, \\ \alpha_{12} &= \alpha_{23} = 0.25A_2, \\ \alpha_{13} &= \alpha_{22} = 0.5A_1 - 0.25A_2. \end{aligned} \tag{2.13}$$

For a three-cell lattice similar formulae are obtained:

$$\begin{aligned} \alpha_{11} &= \alpha_{21} = \alpha_{31} = A_1, \\ \alpha_{12} &= \alpha_{33} = 0.5A_2 - 0.25A_1, \\ \alpha_{13} &= \alpha_{32} = 0.75A_1 - 0.5A_2, \\ \alpha_{22} &= \alpha_{23} = 0.25A_1. \end{aligned} \tag{2.14}$$

If the lattice contains $2n$ cells, $n = 2, 3, 4...$ and is symmetrical with respect to the vertical line passing through one of the bottom vertices (see the line of symmetry in fig. 2.7) the formulae for cells lying to the right of the symmetry line are:

$$\begin{aligned} \alpha_{i1} &= A_1, \\ \alpha_{i2} &= 0.5iA_1 - 0.25(2i-1)A_2, \\ \alpha_{i3} &= 0.25(2i-1)A_2 - 0.5(i-1)A_1, \end{aligned} \tag{2.15}$$

where $i = 1, 2, ...n$.

If a lattice of more complex shape or just a lattice without the vertical line of symmetry or consisting, for example, of an odd number of cells is designed, the formulae for the cells CTEs can be obtained in similar way. If two substrates are connected by a one-row lattice with three cells or more, they also can be connected by a lattice containing two or more rows. This may be advantageous if a lattice possessing a particular ratio of width to height is preferable.

2.4 Cells with weak anisotropy

We consider anisotropy weak if the change of angles in the base triangle (da, db, dc) weakly influences the values of skew angles for given three cell CTEs and therefore can be neglected. An example of weak anisotropy will be considered in Problem 1, Section 2.6. All results presented in this section pertain to the case of weak anisotropy. However, analogous results for the cells with strong anisotropy can be obtained in similar way if there is additional information about the cell skewness.

For cells with low anisotropy and consequently low coupling, the range Ω which defines the upper and lower boundaries for cell CTEs can be found from equation (2.11). In fig. 2.8, it is seen that the interval Ω increases with respect to the ratio α_2/α_1. Hence, proper choice of the ratio α_2/α_1 can provide the existence of the solution t_1, t_2, t_3 of the equations (2.7) for all CTEs determined from kinematic conditions (2.13) or (2.14) or (2.15). In other words, to select lattice materials, such a ratio α_2/α_1 that all CTEs belong to the range Ω (fig. 2.8) must be chosen.

For a two-cell lattice, all values must belong to the interval Ω, and the CTEs, α_1 and α_2, of the two materials that comprise the lattice are restricted by the following

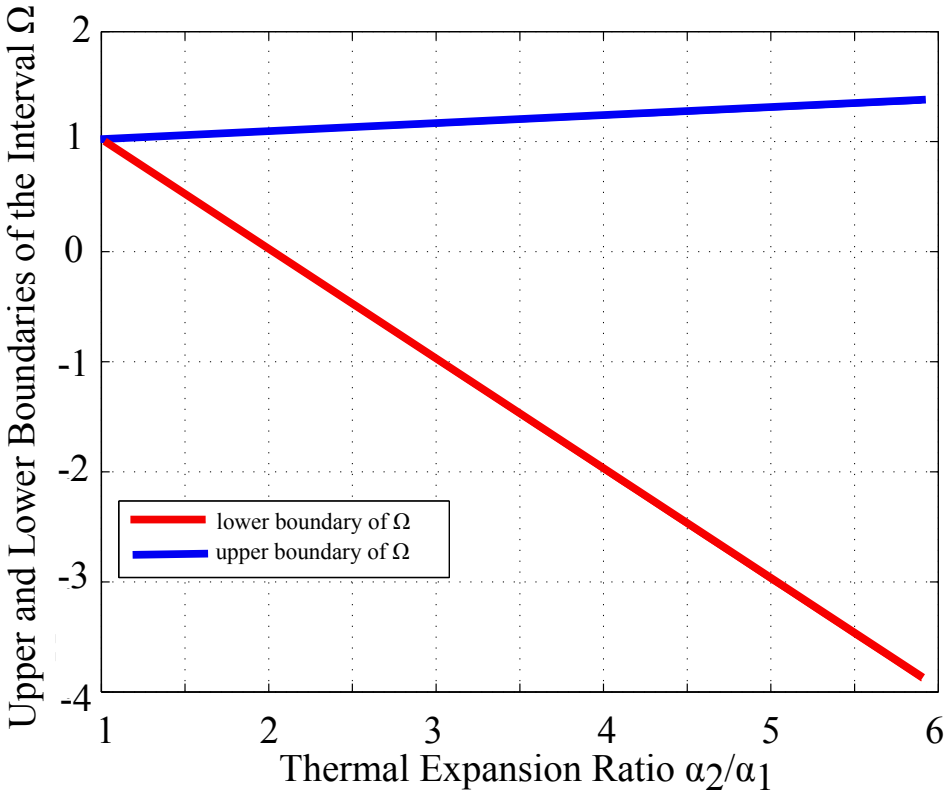

Figure 2.8: Upper and lower boundaries of the normalized CTE, giving the range Ω, as a function of the ratio α_2/α_1. The range of CTEs that can be obtained by a lattice made of materials with known ratio α_2/α_1 is given by the interval between the red and blue lines.

inequalities:

$$\begin{aligned} \alpha_2 + A_1 &> 2\alpha_1, \\ \alpha_2 + 0.25A_2 &> 2\alpha_1, \\ \alpha_2 + 0.5A_1 - 0.25A_2 &> 2\alpha_1, \\ \alpha_2 + 12.93\alpha_1 &> 13.93A_1, \\ \alpha_2 + 12.93\alpha_1 &> 3.48A_2, \\ \alpha_2 + 12.93\alpha_1 &> 6.97A_1 - 3.48A_2. \end{aligned} \tag{2.16}$$

For a three-cell lattice, the conditions on the CTEs of the materials comprising the

lattice are:

$$\begin{aligned} \alpha_2 + 0.25A_1 &> 2\alpha_1, \\ \alpha_2 + 0.5A_2 - 0.25A_1 &> 2\alpha_1, \\ \alpha_2 + 0.75A_1 - 0.5A_2 &> 2\alpha_1, \\ \alpha_2 + 12.93\alpha_1 &> 13.93A_1, \\ \alpha_2 + 12.93\alpha_1 &> 6.97A_2 - 3.48A_1, \\ \alpha_2 + 12.93\alpha_1 &> 10.45A_1 - 6.97A_2. \end{aligned} \tag{2.17}$$

For an n-cell lattice, the conditions for the lattice materials are:

$$\begin{aligned} \alpha_2 + A_1 &> 2\alpha_1, \\ \alpha_2 - 0.25A_2 + 0.5A_1 + 0.5i(A_2 - A_1) &> 2\alpha_1, \\ \alpha_2 + 12.93\alpha_1 &> 13.93A_1, \\ \alpha_2 + 12.93\alpha_1 + 6.97i(A_2 - A_1) &> 3.48A_2. \end{aligned} \tag{2.18}$$

Two additional analogous conditions define the maximum number of cells that the lattice made of these materials can contain:

$$\begin{aligned} n &< \frac{2\alpha_2 + 0.5A_2 - 4\alpha_1}{A_2 - A_1} \\ n &< \frac{0.5A_2 + 0.14\alpha_2 + 1.86\alpha_1 - A_1}{A_2 - A_1}. \end{aligned} \tag{2.19}$$

These inequalities provide that all CTEs in an n-cell lattice belong to the range Ω. More precise conditions for the CTEs of two-, three- , and n-cell lattices can be obtained from strongly anisotropic cells (2.7), but this is only possible if additional information for the lattice shape is known, i.e., if the skew angles adjacent to two sides of the base triangle are the same and the skew angles adjacent to the third side of the base triangle are close to zero (these kind of cells will be used for the design of actuators).

2.5 General algorithm of lattice design

Assembling all the reasoning presented in the previous sections, the following algorithm is proposed for lattice tailoring:

1. Choose the initial number of cells in the lattice.

2. Locate all vertices where cells connect to each other or the substrates.

3. Using the formulae (2.13), (2.14), or (2.15), find the CTEs α_{ij} in all cells of the lattice as functions of the substrate CTEs A_1 and A_2.

4. The relations (2.16), (2.13), (2.18) can be used for the initial choice of lattice material CTEs and their ratio α_2/α_1.

5. Check the existence of solutions to equations (2.7) at calculated values of normalized CTEs of the current cell $\overline{\alpha}_i/\alpha_1 = \alpha_{ij}/\alpha_1$, $i = 1, 2, 3$ and the chosen ratio of α_2/α_1.

6. If the solution exists, find the skew angles of the current cell. Then repeat the previous step with the next cell of the lattice.

7. If the solution does not exist, there are three options

   (a) Choose lattice materials with a higher value of the ratio α_2/α_1.

   (b) Use unequal negative skew angles adjacent to the cell members in order to provide a wider range of cell CTEs.

   (c) Reduce the number of cells in the lattice.

8. After step 6, repeat step 4.

9. The lattice design halts when this procedure is performed for all cells in the lattice. If the lattice can be successfully designed, it may be possible to increase the number of units cells and redesign the lattice, beginning at step 1.

The initial number of lattice cells is determined heuristically, accounting for the geometry of the substrates and the difference between their CTEs. The larger the difference, the fewer cells the lattice can contain. Problem 6 from the next section will illustrate this. The final number of cells is determined through item 7(c) in the design algorithm.

2.6 Examples

This section describes the design of several lattices made of different materials and connecting substrates with different CTEs. The examples show how the CTEs of the lattice and the substrate materials, along with the number of cells, influence the lattice shape. This information is essential for proper selection of lattice and substrate materials in the design of thermal actuators (Chapter 4).

The materials and their CTEs that are used in this section are presented below:

Table 2.1: Material CTEs

Materials	CTE (ppm/°C)	Young's modulus (GPa)	Poisson's ratio
Aluminum	22.2	70	0.33
Austenitic stainless steel (304)	17.3	193	0.29
Brass	18.7	97	0.35
Ferritic stainless steel	9.9	190	0.275
Kovar	5.5	138	0.317
Magnesium alloy (AZ81A type)	28.0	45	0.34
Titanium alloy (Ti-6Al-4V Grade 5)	8.6	116	0.342
Torlon 4203L	30.6	4.0	0.45
Zirconium	5.7	88	0.34

Problem 1: This is an example of connecting titanium and stainless steel substrates with a two-cell lattice made of titanium and magnesium alloy, such that $\alpha_2/\alpha_1 = 3.26$. From equations (2.13), we find: $\alpha_{11}/\alpha_1 = \alpha_{21}/\alpha_1 = A_1/\alpha_1 = 1$, $\alpha_{12}/\alpha_1 = \alpha_{23}/\alpha_1 = 0.25A_2/\alpha_1 = 0.5$, $\alpha_{13}/\alpha_1 = \alpha_{23}/\alpha_1 = 0.5A_1/\alpha_1 - 0.25A_2 = 0$. Now, using formulae (2.7), the skew angles in the left cell can be calculated as $t_1 = 0.0°$, $t_2 = 13°$, $t_3 = 24.9°$ (fig. 2.9). These values are found from the equations accounting for strong anisotropy. If the change of the angles in the base triangle were not considered, the skew angles would be $t_1 = 0.0°$, $t_2 = 13°$, $t_3 = 20.6°$. So, the anisotropy can be treated as weak and the inequalities (2.16) can be used to define a region of allowable values of α_1 and α_2; the region is plotted in fig. 2.10. For this case, the third and the forth inequalities in (2.16) are the most restrictive. Their intersection provides a minimum of $\alpha_2 = 16.1$ ppm/°C, with corresponding $\alpha_1 = 8.0$ ppm/°C.

The utility of the lattice adapter can be illustrated by this example. For comparison, a bimetallic strip consisting of titanium and stainless steel layers of the same thickness welded together and uniformly heated by 100°C will be bent due to thermal expansion mismatch (Timoshenko, 1925). The maximum stress during heating of this bimetallic strip as calculated in Timoshenko (1925) is 50 MPa. The pin-connected lattice adapter described here experiences no thermal mismatch stress.

Problem 2: The same lattice materials can be used to connect other substrates, which have CTEs that are more widely different, for example, zirconium and brass. In this case, $\alpha_{11}/\alpha_1 = \alpha_{21}/\alpha_1 = A_1/\alpha_1 = 0.66$, $\alpha_{12}/\alpha_1 = \alpha_{23}/\alpha_1 = 0.25A_2/\alpha_1 = 0.54$, $\alpha_{13}/\alpha_1 = \alpha_{23}/\alpha_1 = 0.5A_1/\alpha_1 - 0.25A_2 = -0.21$. The skew angles for the left cell are $t_1 = 8.3°$,

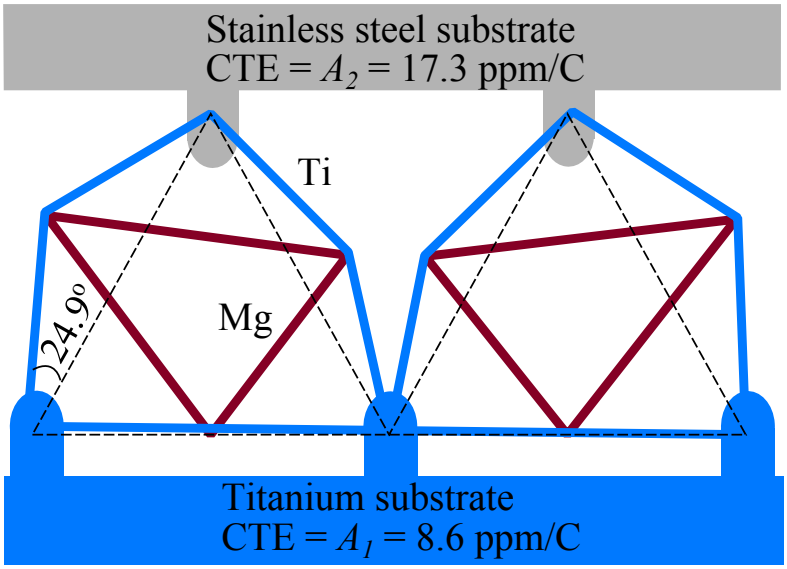

Figure 2.9: Problem 1: Two-cell magnesium alloy-titanium lattice to connect titanium and stainless steel substrates.

$t_2 = 11°$, $t_3 = 27.5°$ (fig. 2.11). It is seen that skew angles of the lattice cells are greater than those from Problem 1. While zirconium and brass are unlikely candidates for lattice construction, their widely differing CTEs make them good example materials.

Problem 3: We can connect the same substrates as Problem 2 using other materials for the lattice, for example a Kovar (iron-nickel cobalt alloy) and a magnesium alloy (AZ81A type). Using the equations (2.13), we have $\alpha_{11}/\alpha_1 = \alpha_{21}/\alpha_1 = A_1/\alpha_1 = 1.03$, $\alpha_{12}/\alpha_1 = \alpha_{23}/\alpha_1 = 0.25A_2/\alpha_1 = 0.85$, $\alpha_{13}/\alpha_1 = \alpha_{23}/\alpha_1 = 0.5A_1/\alpha_1 - 0.25A_2 = -0.33$. From formulae (2.7), the skew angles in the left cell can be calculated as $t_1 = -0.5°$, $t_2 = 2.6°$, $t_3 = 21.85°$ (fig. 2.12). In this lattice, the ratio α_2/α_1 is greater than in the lattices of the previous problems, which is why the lattice cells are less skewed.

In the next problems, bimaterial lattices with high anisotropy are designed based on an equilateral triangle.

Problem 4: A two-cell aluminum-titanium lattice connecting aluminum and titanium substrates can be designed if large skew angles are acceptable. So, $\alpha_2/\alpha_1 = 2.58$ and $\alpha_{11}/\alpha_1 = \alpha_{21}/\alpha_1 = A_1/\alpha_1 = 1$, $\alpha_{12}/\alpha_1 = \alpha_{23}/\alpha_1 = 0.25A_2/\alpha_1 = 0.645$, $\alpha_{13}/\alpha_1 = \alpha_{23}/\alpha_1 = 0.5A_1/\alpha_1 - 0.25A_2 = -0.145$. The skew angles for the left cell are $t_1 = 0°$, $t_2 = 11.35°$, $t_3 = 34.94°$ (fig. 2.13). Here, $t_3 > 30°$ is allowed because these are the exterior sides of the lattice and hence there are no adjacent cells to cause interference. It does however make the addition of further cells impossible.

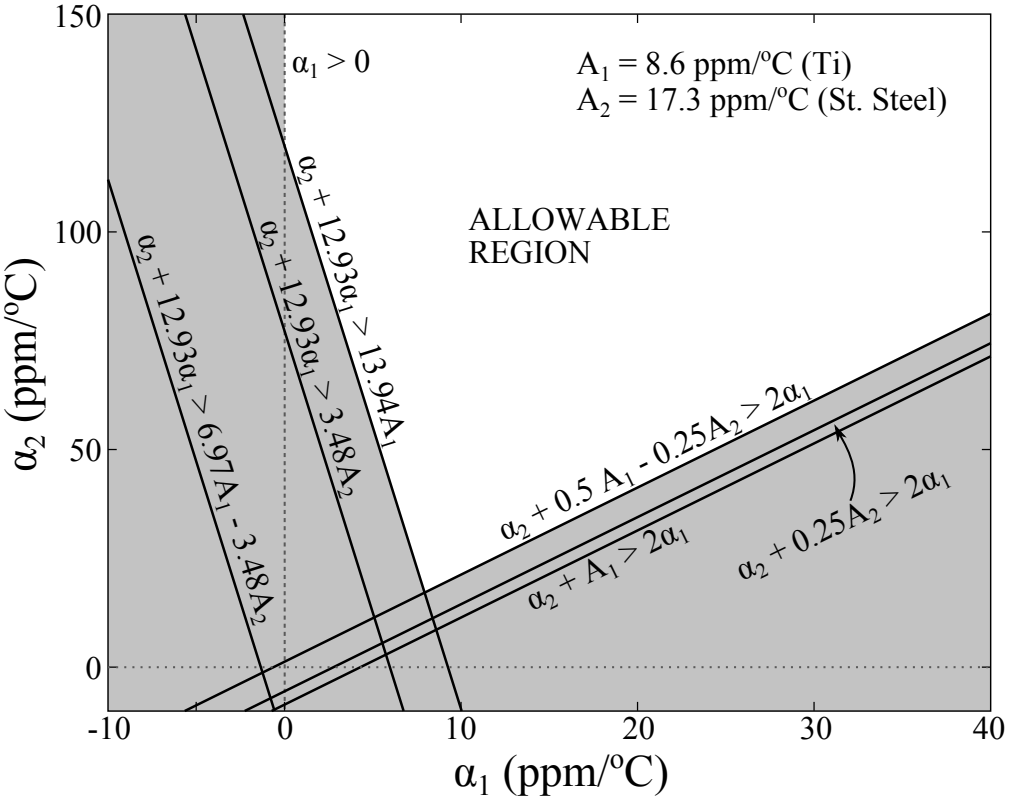

Figure 2.10: Problem 1: The white region indicates the ranges for the CTEs of the lattice materials that can be used to design the lattice for Problem 1. The lines defining the allowable region are the inequalities in equation (2.16). Note the difference in the scales of the two axes; for small or moderately large values of α_1, very large values of α_2 are implied.

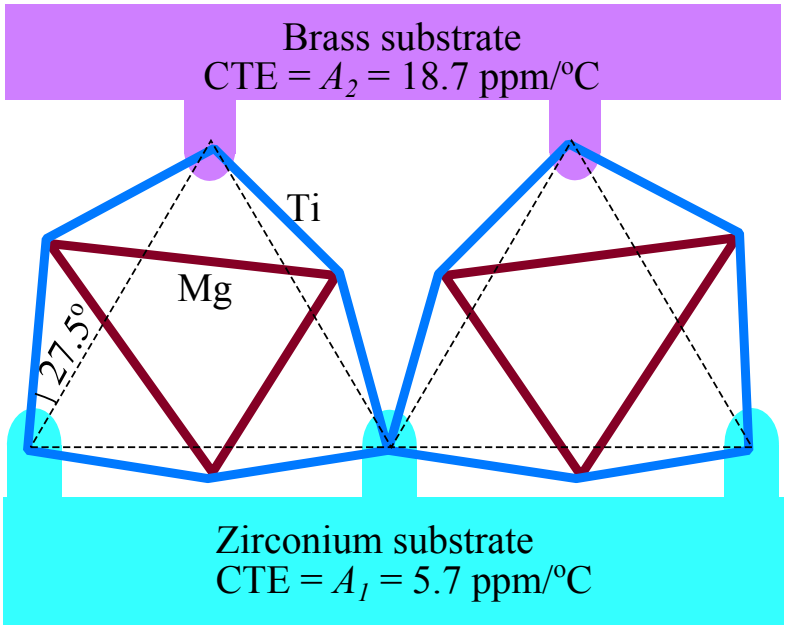

Figure 2.11: Problem 2: Two-cell magnesium-titanium lattice to connect zirconium and brass substrates.

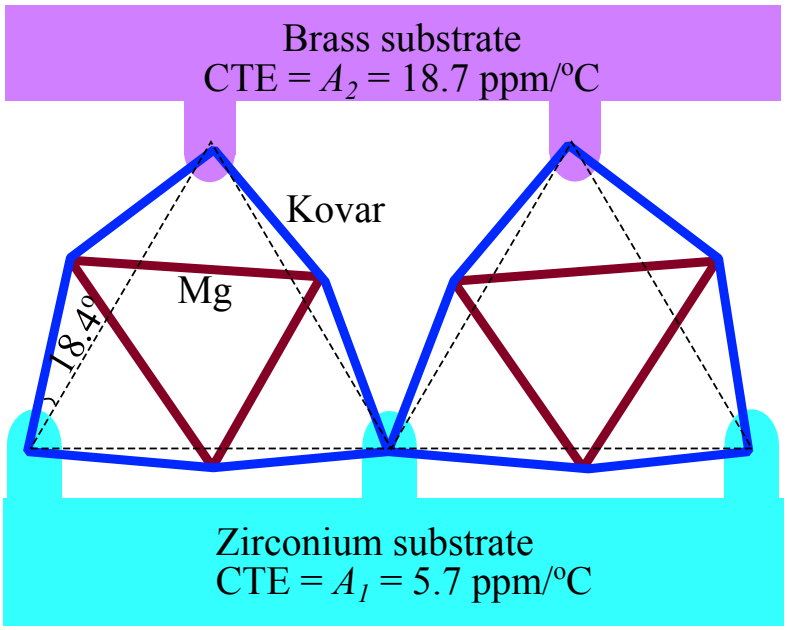

Figure 2.12: Problem 3: Two-cell magnesium alloy-Kovar lattice to connect zirconium and brass substrates.

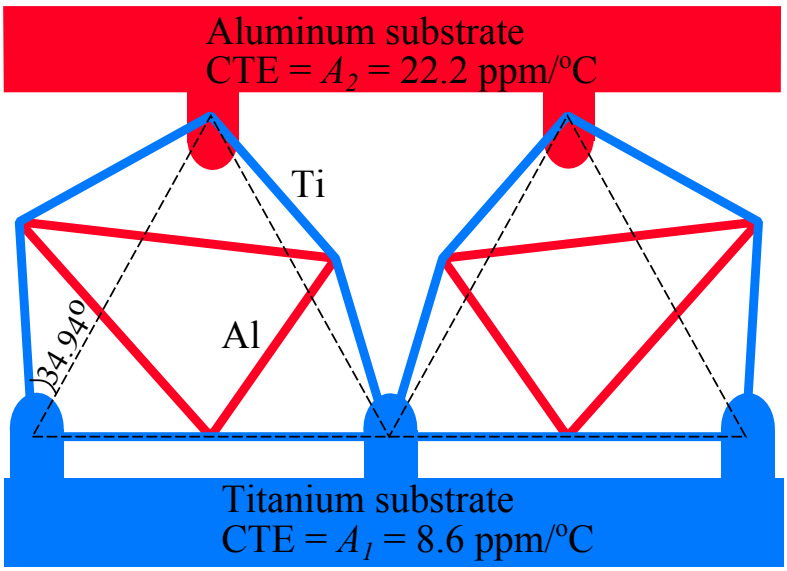

Figure 2.13: Problem 4: Two-cell titanium-magnesium alloy lattice to connect titanium and aluminum substrates.

Problem 5: In this problem, we design a three-cell magnesium-titanium lattice connecting aluminum and titanium substrates. Using formulae (2.14), we find: $\alpha_{11}/\alpha_1 = \alpha_{21}/\alpha_1 = \alpha_{31}/\alpha_1 = 1$, $\alpha_{12}/\alpha_1 = \alpha_{33}/\alpha_1 = 1.04$, $\alpha_{13}/\alpha_1 = \alpha_{32}/\alpha_1 = -0.54$, $\alpha_{22}/\alpha_1 = \alpha_{23}/\alpha_1 = 0.25$. The skew angles for the first cell on the left are $t_1 = 0.0°$, $t_2 = -1.0°$, $t_3 = 36.8°$. The skew angles for the second cell are $t_1 = 0.0°$, $t_2 = 19.1°$, $t_3 = 19.1°$ (fig. 2.14). The skew angles t_3 in the first cell on the left and the t_2 in last cell on the right are greater than 30°. In this case, it is admissible because these skew angles do not cause overlapping with adjoining lattice cells, but limits to the number of cells in this lattice to three.

Problem 6: If the substrate materials have CTEs that are relatively similar (A_2/A_1 is less than approximately 2), a lattice consisting of four cells and more can be designed. For example, suppose we would like to connect titanium and stainless steel substrates with a magnesium-titanium lattice. For such materials, the maximum total number of cells in the lattice is 4, according to inequalities (2.19). Using formulae (2.15), we have: $\alpha_{11}/\alpha_1 = \alpha_{21}/\alpha_1 = 1$, $\alpha_{12}/\alpha_1 = 0.5A_1/\alpha_1 - 0.25A_2/\alpha_1 = 0.03$, $\alpha_{13}/\alpha_1 = 0.25A_2/\alpha_1 = 0.5$, $\alpha_{22}/\alpha_1 = A_1/\alpha_1 - 0.75A_2/\alpha_1 = -0.5$, $\alpha_{23}/\alpha_1 = 0.75A_2/\alpha_1 - 0.5A_1/\alpha_1 = 1.0$. Now, using the equations (2.7), for cell 1: $t_1 = 0.0°$, $t_2 = 24.45°$, $t_3 = 13°$. For cell 2: $t_1 = 0.0°$, $t_2 = 35.9°$, $t_3 = 0.0°$ (fig. 2.15). The two other cells are symmetric with respect to the vertical line passing through the middle of the lattice. If the substrates were titanium ($A_1 = 8.6$ ppm/°C) and ferritic stainless steel ($A_2 = 9.9$ ppm/°C), then the maximum

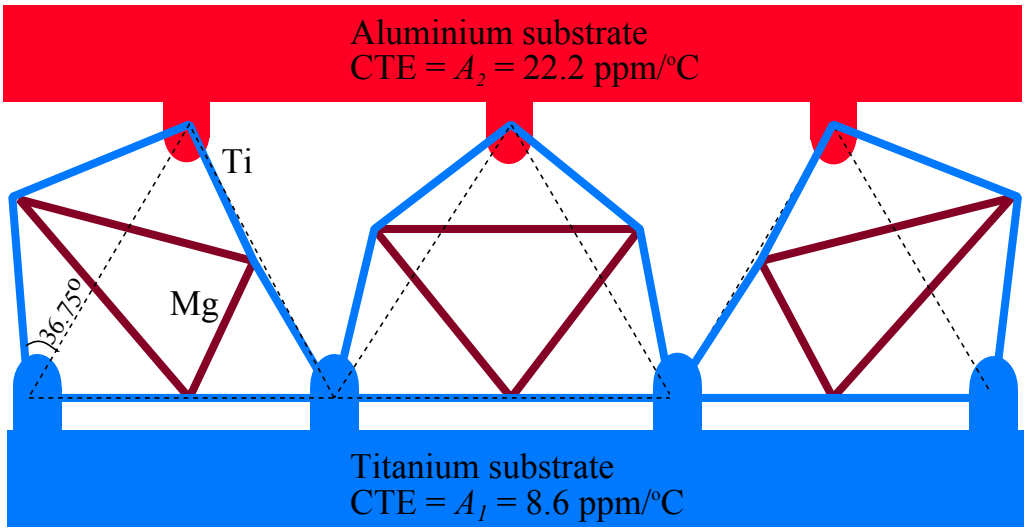

Figure 2.14: Problem 5: Three-cell titanium-magnesium alloy lattice to connect titanium and aluminum substrates.

number of the cells in the lattice would be 22.

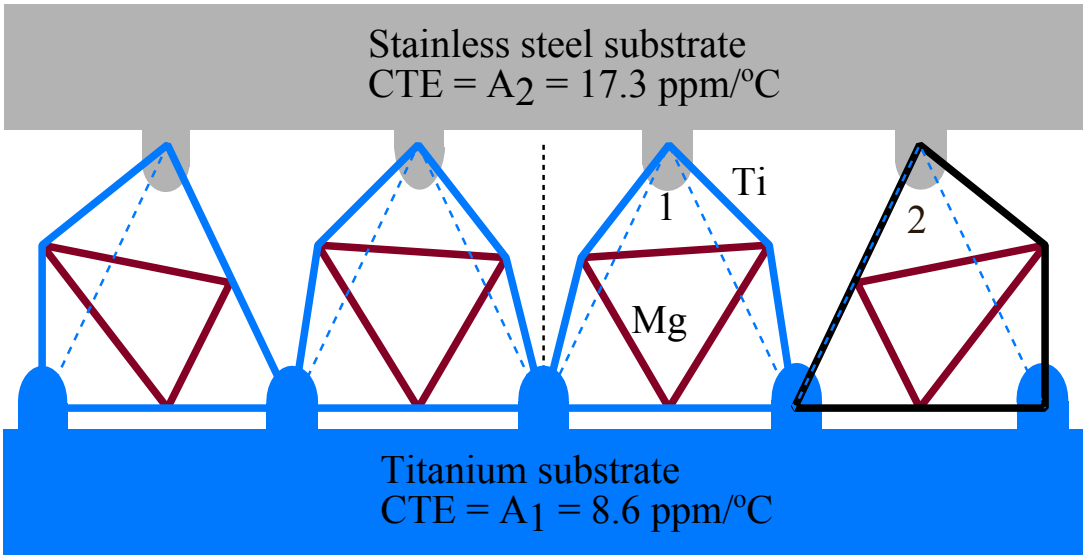

Figure 2.15: Problem 6: Four-cell magnesium alloy-titanium lattice for stainless steel and titanium substrates.

2.7 Concluding remarks

The anisotropic planar lattices described in this chapter provide a structural option for connecting materials with differeng CTEs without generating thermal stresses during temperature excursions. Combining cells with anisotropic CTEs into a pin-jointed lattice

provides the capability to achieve desirable, and differing, CTEs on the bottom and top edges of the lattice. The solutions to the problems considered above show that the more the substrate CTEs differ, the more the lattice cells are skewed. On the other hand, the higher the ratio of CTEs of the lattice materials, the less the cells of the lattice are skewed. Also, different negative skew angles adjacent to the same side of the cell can provide a wider range of CTEs compared to corresponding skew angles equal to each other. The larger the difference between substrate CTEs is, the fewer cells a lattice can contain.

Chapter 3

Advanced adaptive bimaterial lattices

In this chapter, we consider the design of adaptive lattices with more complicated shapes than the lattices considered in Chapter 2 [1] [2] [3]. Earlier, we derived equations connecting three CTEs in a cell with three skew angles for an equilateral base triangle. First, we will generalize these equations for cells based on triangles with arbitrary angles and six independent skew angles. Second, we will design two-row lattices, an angled lattice that can be used to mount a cantilever on the main body of a structure, a non-planar hexagonal lattice connecting two circular disks that can be used for lens alignment, and two lattices that not only mitigate stresses due to thermal expansion mismatch but also compensate thermal expansion of substrates along the lattice height: a lattice controlling total deflection of a structure and a lattice connected a shaft and a collar. Third, we study the structural efficiency of a lattice cell under uniaxial loading and examine ways to increase it. It is important because structural efficiency reduces in cells with high anisotropy. However, three CTEs in each cell can be attained by different combination of six skew angles, from which we choose that one providing the best structural efficiency.

[1] M M Toropova and C A Steeves. Design of composite bi-material lattice adapters. 1st International Conference on Mechanics of Composites , Stony Brook University, USA, June 8-12 , 2014.

[2] M M Toropova and C A Steeves. Adaptive bi-material lattices to mitigate thermal expansion mismatch in satellite structures. 65th International Astronautical Congress, Toronto, Canada, September 29 October 3, 2014.

[3] M M Toropova and C A Steeves. Adaptive bimaterial lattices to mitigate thermal expan- sion mismatch stresses in satellite structures. Acta Astronautica, 113:132-141, 2015.

3.1 Cell design

A typical cell of the lattice is designed based on a virtual triangle ACE that can have different angles a, b, and c and side lengths L_1, L_2, and L_3 (fig. 3.1). Physically, the cell consists of a hexagon $ABCDEF$ made of a material with CTE α_1 and pin-connected to an internal unskewed triangle BDF made of a material with CTE α_2 Toropova and Steeves (2015c). The skew angles of the hexagon are denoted as θ_1, θ_2, θ_3, θ_4, θ_5, and θ_6.

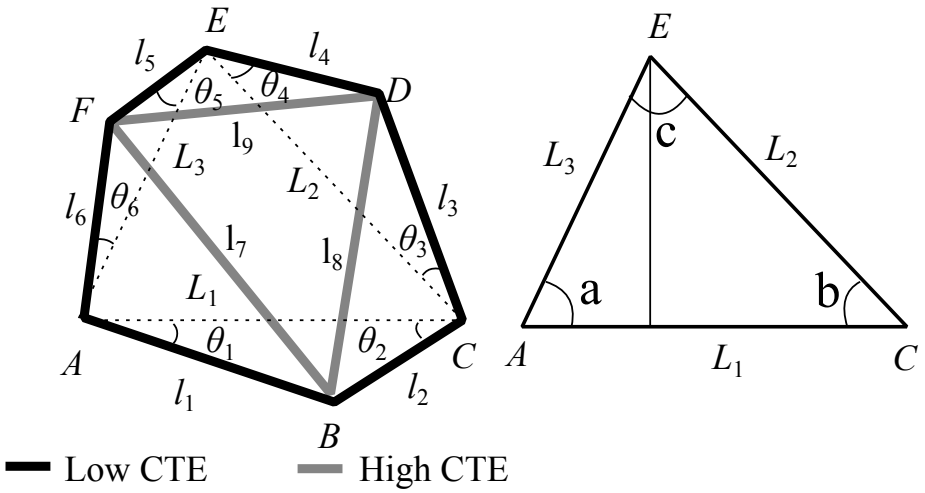

Figure 3.1: One cell of an anisotropic lattice. The members AB, BC, CD, DE, EF, and AF have low CTE, depicted in black. The members BD, DF, BF have higher CTE, depicted in grey. θ_1, θ_2, θ_3, θ_4, θ_5, θ_6, are skew angles of the physical skewed hexagon. The virtual triangle upon which the cell is based is shown as a dashed line on the left and as solid line on the right. It is the relative movement of the vertices of the virtual triangle that defines the effective thermal expansion of the lattice.

When the temperature changes, all members expand according to their CTE: $dl_i = l_i\alpha_1 dT$, $i = (\overline{1,6})$ and $dl_i = l_i\alpha_2 dT$, $i = (\overline{7,9})$. The members of the hexagon rotate, which accommodates (or amplifies) the effect of their extension. Because the skew angles are different, the side lengths of the base triangle change with different rate $dL_1 = \overline{\alpha}_1 L_1 dT$, $dL_2 = \overline{\alpha}_2 L_2 dT$, $dL_3 = \overline{\alpha}_3 L_3 dT$ where $\overline{\alpha}_1$, $\overline{\alpha}_2$, $\overline{\alpha}_3$ are three cell CTEs along the lines AC, CE, and AE, respectively, and T is temperature (fig. 3.2). It means that the cell has anisotropic thermal expansion. Also, because the vertices can be moved deterministically, the cell behaves like a thermal actuator.

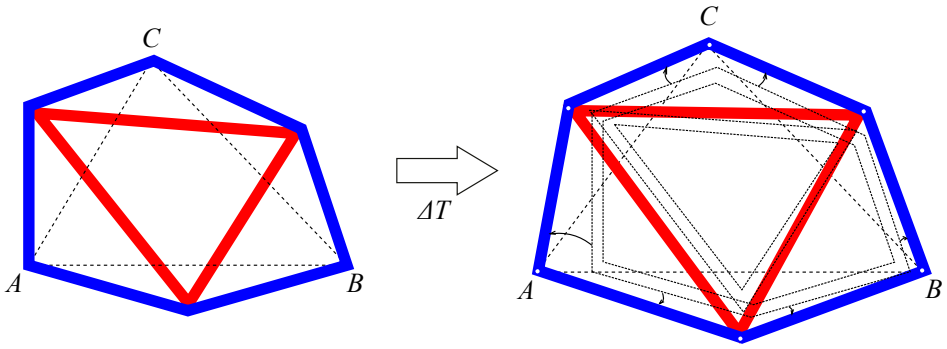

Figure 3.2: Sketch of the kinematics of the thermal expansion of an anisotropic bimaterial lattice cell.

Repeating the procedure described in Chapter 2 and accounting for

$$\frac{l_7^2}{l_1 l_6 \sin A'}(\alpha_2 - \alpha_1)dT = d\theta_1 + d\theta_6 + da,$$
$$\frac{l_8^2}{l_2 l_3 \sin B'}(\alpha_2 - \alpha_1)dT = d\theta_2 + d\theta_3 + db,$$
$$\frac{l_9^2}{l_4 l_5 \sin C'}(\alpha_2 - \alpha_1)dT = d\theta_4 + d\theta_5 + dc,$$

we obtain three nonlinear equations linking the six skew angles θ_i with three normalized thermal expansion coefficients along the lines AC, CE, and AE in the skewed triangle where $L_1 = AC$, $L_2 = CE$, and $L_3 = AE$:

$$\begin{aligned}
-\frac{\overline{\alpha}_1}{\alpha_1}(\cot\theta_2 + \cot b) + \frac{\overline{\alpha}_2}{\alpha_1}\frac{L_2}{L_1}\frac{1}{\sin b} + \frac{\overline{\alpha}_3}{\alpha_1}\left(\frac{L_3}{L_1}\frac{\cos(a+b)}{\sin b} - \cot\theta_5\right) = \\
\frac{1}{\sin A'}(\frac{\alpha_2}{\alpha_1} - 1)(\frac{l_1}{l_6} + \frac{l_6}{l_1} - 2\cos A') - \cot\theta_2 - \cot\theta_5, \\
-\frac{\overline{\alpha}_1}{\alpha_1}(\cot\theta_1 + \cot a) + \frac{\overline{\alpha}_2}{\alpha_1}\left(\frac{L_2}{L_1}\frac{\cos(a+b)}{\sin a} - \cot\theta_4\right) + \frac{\overline{\alpha}_3}{\alpha_1}\frac{L_3}{L_1}\frac{1}{\sin a} = \\
\frac{1}{\sin B'}(\frac{\alpha_2}{\alpha_1} - 1)(\frac{l_2}{l_3} + \frac{l_3}{l_2} - 2\cos B') - \cot\theta_1 - \cot\theta_4, \\
\frac{\overline{\alpha}_1}{\alpha_1}(\cot a + \cot b) - \frac{\overline{\alpha}_2}{\alpha_1}\left(\frac{L_2}{L_1}\frac{\cot b\sin(a+b)}{\sin a} + \cot\theta_3\right) - \\
\frac{\overline{\alpha}_3}{\alpha_1}\left(\frac{L_3}{L_1}\frac{\cot a\sin(a+b)}{\sin b} + \cot\theta_6\right) = \\
\frac{1}{\sin C'}(\frac{\alpha_2}{\alpha_1} - 1)(\frac{l_4}{l_5} + \frac{l_5}{l_4} - 2\cos C') - \cot\theta_3 - \cot\theta_6,
\end{aligned} \tag{3.1}$$

Equations (3.1) are scale independent and contain the ratio α_2/α_1 as a parameter. The coupling of three normalized CTEs in a cell ($\overline{\alpha}_1/\alpha_1$, $\overline{\alpha}_2/\alpha_1$, and $\overline{\alpha}_3/\alpha_1$) is strong. Also, equations (3.1) define the range for each $\overline{\alpha}_1/\alpha_1$, $\overline{\alpha}_2/\alpha_1$, and $\overline{\alpha}_3/\alpha_1$. The equations (3.1) are linear with respect to $\overline{\alpha}_i/\alpha_1$, $i = 1, 2, 3$, but their dependence on the skew angles is nonlinear. If the skew angles are known, three CTEs of a cell can be calculated by a number of different ways, for example, by using Kramer's method. If any skew angle $t_i = 0$, they must be solved with $t_i \to 0$ to avoid division by zero.

3.2 Design of two-row lattices with cell rotation

In Chapter 2, we designed one-row lattices consisting of two, three, or n cells. However, as it was shown, the maximum number of cells was limited because the total deflections that must be accommodated increase with lattice length and with the increase in the difference between the CTEs of substrate materials. To design a lattice that mitigates thermal mismatch stresses between substrates with a large difference in CTEs, several strategies can be employed. First, lattice materials with larger α_2/α_1 ratios can be chosen. Negative nonequal skew angles adjacent to the same side of the base triangle also increase cell CTEs. A third method to connect substrates with large differences in CTEs is to use two-row lattices, where the lower row is designed as if it connects two substrates with the same CTE, and the heights of both rows remain independent of temperature: the number of cells in the upper row is one less than in the lower row. Note that, as will be shown in Section 3.5, connecting two specific substrates with a two-row lattice may provide better structural efficiency than a one-row lattice. A fourth, more powerful, strategy to connect substrates with significant difference in their CTEs is to use two-row lattices with cell rotation. The restriction that the height of the cells remains constant is relaxed, enabling individual cells to rotate. This can be used to increase the effective CTEs that can be generated on the lattice boundaries. To clarify the basic principles of their design, we analyze cells based on equilateral triangles with skew angles adjacent to the same side equal to each other. The lattices have a vertical line of symmetry and connect two substrates with constant separation H. Particular cells in both rows can change their heights h. Such lattices can be used to connect substrates with a large difference in CTEs.

1. First, consider a lattice consisting of three cells in the lower row and two cells in the upper row. Its skeleton is depicted on fig. 3.3. Suppose that the first cell in the lower row shrinks along the height CF with the CTE $-\alpha_h$, and the second cell extends along the height EG with the CTE α_h. The third cell in the lower row behaves like the first

because of symmetry. After heating the points A, B, C, D, E, F, M, and N become A', B', C', D', E', F', M', and N' respectively. This allows the cells in the upper row to acquire additional rotation and provide greater extension between the vertices M and N that connected to the substrate 2. Dashed lines show the positions of the cells after heating.

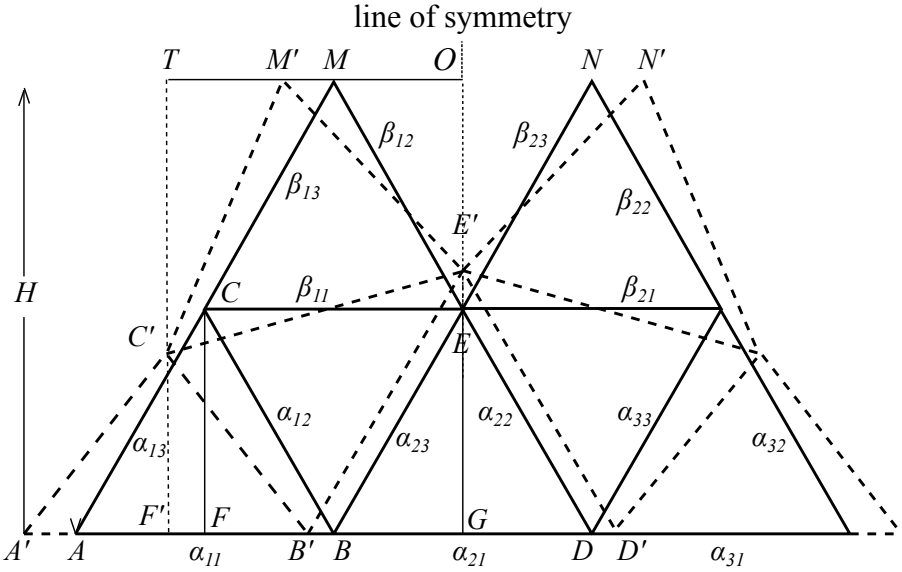

Figure 3.3: The virtual cells of a two row lattice with five cells showing cell rotation. The solid lines show the initial position of the virtual lattice, while the dashed lines show the configuration after thermal changes. Note that the two cells in the top row rotate in addition to changing shape due to thermal expansion.

To obtain the formulae for the calculation of three CTEs in each cell of the lattice, we need nomenclature to identify the different CTEs of the lattice cells. Denote by α_{ij} the CTEs in the cells of the lower row: the first index i indicates the number of a cell in the row and the second index indicates the number of the CTE in the cell. For example, in the cell ABC, α_{11} is the CTE along AB, α_{12} is the CTE along BC, and α_{13} is the CTE along AC. To identify the CTEs of the upper row cells, we introduce β_{ij} with indices i and j having the same meaning as for α_{ij} (fig. 3.3). In the design of the lattice, suppose that

$$\beta_{11} = \beta_{21} = \alpha_{11} = \alpha_{21} = \alpha_{31} = A_1. \tag{3.2}$$

For the remaining α_{ij}, the formulae derived in Toropova and Steeves (2014c) for a three-

cell one-row lattice where $A_1 = A_2$ and $\alpha_h \neq 0$ can be used. Therefore, we have

$$\alpha_{12} = \alpha_{13} = \alpha_{32} = \alpha_{33} = 0.25A_1 - 0.75\alpha_h, \tag{3.3}$$
$$\alpha_{22} = \alpha_{23} = 0.25A_1 + 0.75\alpha_h,$$

In the second row, $(M'O)^2 = L^2(1 + \beta_{12}dT)^2 - 0.75L^2(1 - \alpha_h dT)^2 = (0.5L(1 + (4\beta_{12} + 3\alpha_h)dT))^2$, where L is the side length of the base triangle of the lattice cells and dT is the increment of temperature. On the other hand, because the distance between points M and N extends with the CTE A_2, $M'O = 0.5L(1 + A_2 dT)$. Hence, neglecting terms with dT^2, we have

$$\beta_{12} = \beta_{23} = 0.25A_2 - 0.75\alpha_h, \tag{3.4}$$

Similarly, $(TM')^2 = L^2(1 + \beta_{13}dT)^2 - 0.75L^2(1 + \alpha_h dT)^2 = (0.5L(1 + (4\beta_{13} - 3\alpha_h)dT))^2$. Thus, when temperature changes, $TO = L(1 + A_1 dT) = 0.5L(1 + (4\beta_{13} - 3\alpha_h dT) + 0.5L(1 + (4\beta_{12} + 3\alpha_h)dT)$. Therefore,

$$\beta_{13} = \beta_{22} = 0.5A_1 - 0.25A_2 + 0.75\alpha_h. \tag{3.5}$$

If $\alpha_h \equiv 0$, the formulae (3.4-3.5) coincide with the formulae for two-cell one-row lattice obtained in Toropova and Steeves (2014c).

2. Consider a lattice containing four cells in the lower row and three cells in the upper row. Its skeleton is shown in fig. 3.4. Suppose that the first and the fourth cells in the lower row shrink along their heights with the CTE $-\alpha_h$, while the second and the third cells extend along their heights with the CTE α_h. After heating, the lattice cells will have the position indicated by dashed lines. To find α_{ij}, we can use the formulae (2.15) for $2n$-cell one-row lattices at $A_1 = A_2$ and $\alpha_h \equiv 0$:

$$\alpha_{12} = \alpha_{13} = \alpha_{42} = \alpha_{43} = 0.25A_1 - 0.75\alpha_h, \tag{3.6}$$
$$\alpha_{22} = \alpha_{23} = \alpha_{32} = \alpha_{33} = 0.25A_1 + 0.75\alpha_h. \tag{3.7}$$

Similar to a five-cell lattice, we design a seven-cell lattice with the lower row as if it connects two substrates with the same CTE, therefore

$$\beta_{11} = \beta_{21} = \beta_{31} = \alpha_{11} = \alpha_{21} = \alpha_{31} = \alpha_{41} = A_1. \tag{3.8}$$

Using the results obtained above, we write $M'N + NO = 0.5L(1 + (4\beta_{12} + 3\alpha_h)dT) +$

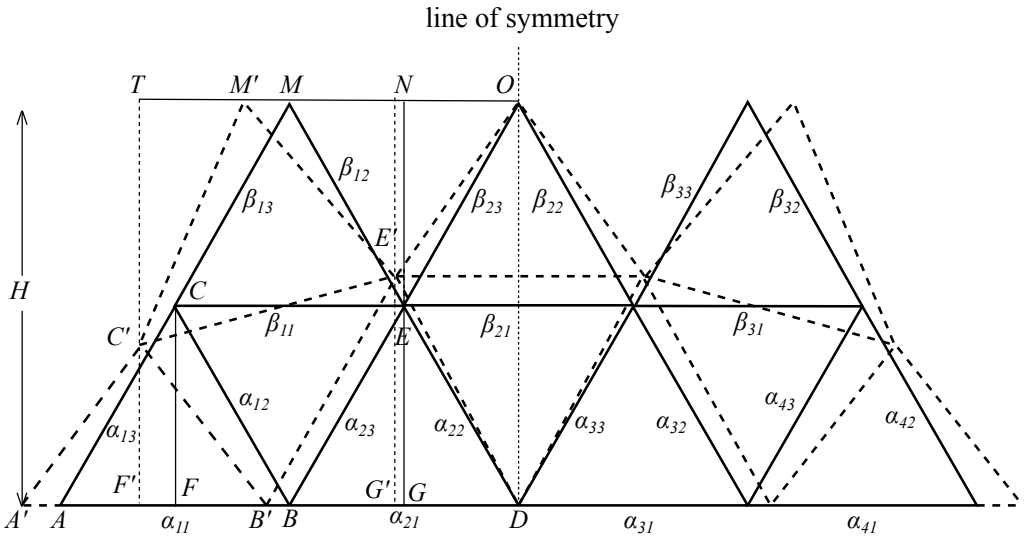

Figure 3.4: The virtual cells of a two row lattice with seven cells, where the solid lines are the virtual cells before and the dashed lines the cells after thermal expansion. Again, note that the cells in the upper row rotate because the height h of the cell in the lower row is permitted to change.

$0.5L(1 + A_1 dT) = L(1 + A_2 dT)$. From this, we find

$$\beta_{12} = \beta_{33} = 0.5A_2 - 0.25A_1 - 0.75\alpha_h. \tag{3.9}$$

Similarly, $TM' + M'N + NO = 0.5L(1 + (4\beta_{12} + 3\alpha_h)dT) + 0.5L(1 + A_1 dT) + 0.5L(1 + (4\beta_{13} - 3\alpha_h)dT) = 1.5L(1 + A_1 dT)$. From this, we have

$$\beta_{13} = \beta_{32} = 0.75A_1 - 0.5A_2 + 0.75\alpha_h. \tag{3.10}$$

The middle cell in the upper row behaves like the first cell in the lower row, hence

$$\beta_{22} = \beta_{23} = 0.25A_1 - 0.75\alpha_h. \tag{3.11}$$

In this case, again if $\alpha_h \equiv 0$, the formulae (3.9-3.11) coincide with formulae obtained in Toropova and Steeves (2014c) for three-cell one-row lattice.

Two materials of the lattice, with CTEs α_1 and α_2, and the CTE α_h of the cell height, reflecting the degree of the cell rotation, must be chosen to satisfy the equations (3.1). The larger α_h is, the more the left and the right cells in the upper row rotate (fig. 3.3, fig. 3.4). If $\alpha_h \equiv 0$, there is no rotation; this case was considered in the previous chapter. To solve equations (3.1), we also need to know the ratio α_2/α_1. The solution to the problem of material choice is the same as for a one-row lattice, and it is considered in

detail in Chapter 2.

The CTEs of the materials used in the examples below are presented in the Table 2.1.

Example 1: The higher values of normalized CTEs can be reached at negative nonequal skew angles: $\theta_1 \neq \theta_2$, $\theta_3 \neq \theta_4$, $\theta_5 \neq \theta_6$. This case will be illustrated by a three-cell titanium-magnesium alloy lattice connecting titanium and magnesium alloy substrates (fig. 3.5). We used negative unequal skew angles to provide a wider range of $\overline{\alpha}_2$ in the left cell and $\overline{\alpha}_3$ in the right cell.

From formulae (2.14), we have $\alpha_{11}/\alpha_1 = \alpha_{21}/\alpha_1 = \alpha_{31}/\alpha_1 = 1$, $\alpha_{12}/\alpha_1 = \alpha_{33}/\alpha_1 = 1.375$, $\alpha_{13}/\alpha_1 = \alpha_{32}/\alpha_1 = -0.875$, $\alpha_{22}/\alpha_1 = \alpha_{23}/\alpha_1 = 0.25$. To get a large positive value of α_{12}/α_1, we can use negative nonsymmetric skew angles $\theta_3 \neq \theta_4$ and for a small negative value of α_{13}/α_1, we can use symmetric angles greater than 30°; this will not lead to the overlapping of the cells because these skew angles are adjacent to the external sides of the lattice. The skew angles for the second cell are the same as in Problem 5 (Chapter 2). The solution for the first cell on the left is not unique, for example, the skew angles that satisfy equations (2.7) may be $\theta_1 = \theta_2 = 0.0°$, $\theta_3 = -14.19°$, $\theta_4 = -5.2°$, $\theta_5 = \theta_6 = 37.75°$. The sketch of the lattice is in fig. 3.5. Note that this problem has infinite number of solutions if we use non-equal skew angles adjacent to the same side of a base triangle.

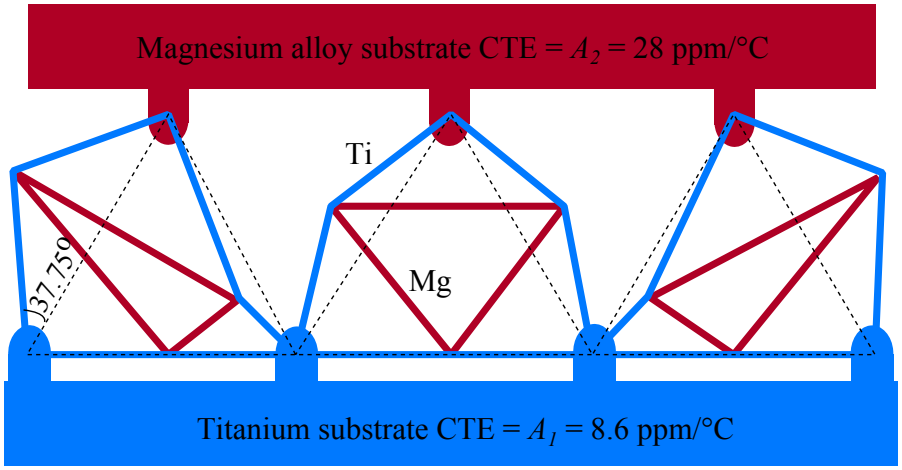

Figure 3.5: A three-cell titanium-magnesium alloy lattice to connect titanium and magnesium substrates. The available range of thermal expansion is expanded by allowing the six skew angles to be independent. The lattice has large and negative skew angles and is structurally inefficient.

This problem can be solved by using a two-row five-cell titanium-magnesium alloy lattice, hence, $\alpha_2/\alpha_1 = 3.26$. Suppose $\alpha_h \equiv 0$. Then, from the equations derived in

this section (3.2-3.5), we obtain: $\alpha_{11}/\alpha_1 = \alpha_{21}/\alpha_1 = \alpha_{31}/\alpha_1 = \beta_{11}/\alpha_1 = \beta_{21}/\alpha_1 = 1$, $\alpha_{12}/\alpha_1 = \alpha_{13}/\alpha_1 = \alpha_{22}/\alpha_1 = \alpha_{23}/\alpha_1 = \alpha_{32}/\alpha_1 = \alpha_{33}/\alpha_1 = 0.25$, $\beta_{12}/\alpha_1 = \beta_{23}/\alpha_1 = 0.81$, $= \beta_{13}\alpha_1 = \beta_{22}/\alpha_1 = -0.31$. Now, using formulae (3.1), we find that for the cells in the lower row $\theta_1 = \theta_2 = 0.0°$, $\theta_3 = \theta_4 = \theta_5 = \theta_6 = 19.1°$. For the left cell in the upper row, $\theta_1 = \theta_2 = 0.0°$, $\theta_3 = \theta_4 = 4.9°$, $\theta_5 = \theta_6 = 32.0°$. The right cell is a reflection of the left cells (fig. 3.6). In this problem, we do not need to use rotation of the cells. However,

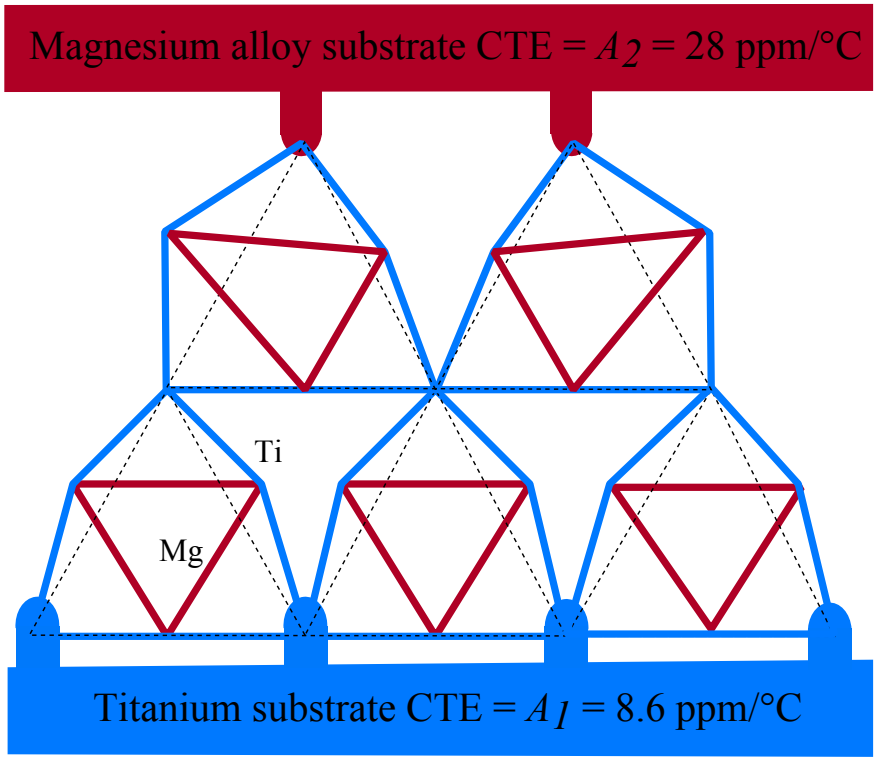

Figure 3.6: A two-row titanium-magnesium alloy lattice to connect titanium and magnesium alloy substrates. The skewness of the lattice is less than for the one-row system.

if the CTE difference between A_1 and A_2 is more substantial, we cannot achieve a feasible lattice design without cell rotation. The following example illustrates this.

Example 2: Suppose, we would like to connect titanium and magnesium alloy substrates with a titanium-magnesium alloy two-row seven cell lattice. Choose the CTE α_h that reflects the rotation of the left and the right cells in the upper row as $\alpha_h/\alpha_1 = 0.7$. We know that $\alpha_{i1}/\alpha_1 = A_1/\alpha_1 = 1$, $i = 1, 2, 3, 4$. From formulae (3.6-3.11), we find: $\alpha_{12}/\alpha_1 = \alpha_{13}/\alpha_1 = \alpha_{42}/\alpha_1 = \alpha_{43}/\alpha_1 = -0.275$, $\alpha_{22}/\alpha_1 = \alpha_{23}/\alpha_1 = \alpha_{32}/\alpha_1 = \alpha_{33}/\alpha_1 = 0.775$, $\beta_{12/\alpha_1} = \beta_{33/\alpha_1} = 0.85$, $\beta_{13}/\alpha_1 = \beta_{32}/\alpha_1 = -0.35$ $\beta_{22}/\alpha_1 = \beta_{23}/\alpha_1 = -0.275$, . Now, using formulae (3.1), the skew angles can be calculated as: cells 1, 4, 6: $\theta_1 = \theta_2 = 0.0°$, $\theta_3 = \theta_4 = \theta_5 = \theta_6 = 26.0°$; cells 2, 3: $\theta_1 = \theta_2 = 0.0°$, $\theta_3 = \theta_4 = \theta_5 = \theta_6 = 7.9°$; cell

5: $\theta_1 = \theta_2 = 0.0°$, $\theta_3 = \theta_4 = 4°$, $\theta_5 = \theta_6 = 32.8°$; cell 7: $\theta_1 = \theta_2 = 0.0°$, $\theta_3 = \theta_4 = 32.8°$, $\theta_5 = \theta_6 = 4°$ (fig. 3.7). Thus, the coefficient $\alpha_h \neq 0$ can extend the range of $\overline{\alpha}_i$,

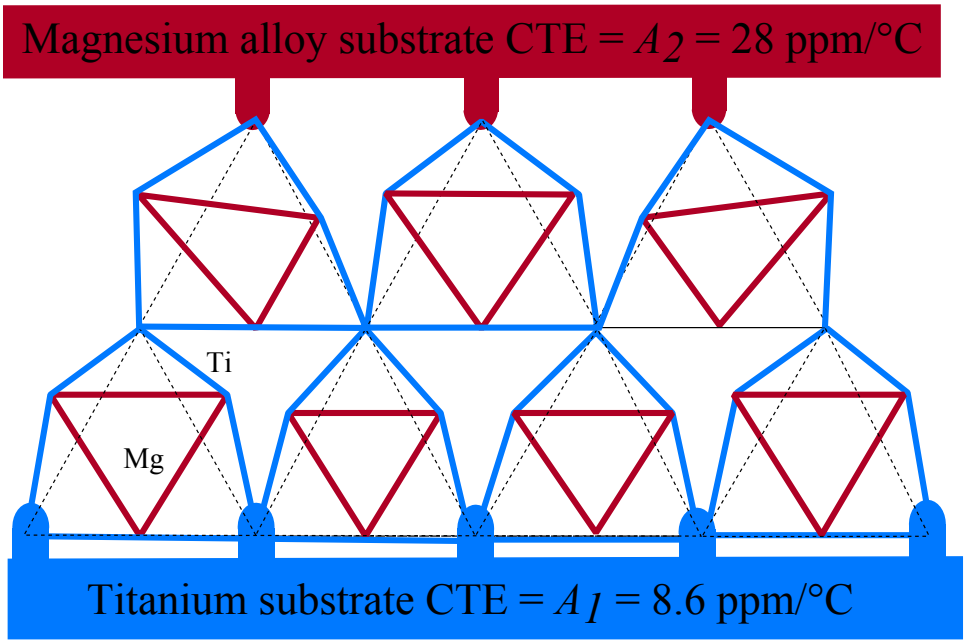

Figure 3.7: Sketch of a two-row, seven cell titanium-magnesium alloy lattice to connect titanium and magnesium alloy substrates.

$i = 1, 2, 3$. However, as will be shown in section 3.5, it leads to the reduction of the structural efficiency of the lattice.

Example 3: To connect substrates made of materials with an even larger difference in their CTEs, for example, titanium and Torlon 4203L, we can use lattice materials with larger difference in their CTEs to increase the ratio α_2/α_1. Additionally, we can increase the rotation of the cells. So, $\alpha_2/\alpha_1 = 3.26$. Let $\alpha_h/\alpha_1 = 0.8$. In this problem, we will use the same sketch as in Example 2. Therefore $\alpha_{i1}/\alpha_1 = A_1/\alpha_1 = 1$, $i = 1, 2, 3, 4$. From formulae (3.6-3.11), we find: $\alpha_{12}/\alpha_1 = \alpha_{13}/\alpha_1 = \alpha_{42}/\alpha_1 = \alpha_{43}/\alpha_1 = -0.35$, $\alpha_{22}/\alpha_1 = \alpha_{23}/\alpha_1 = \alpha_{32}/\alpha_1 = \alpha_{33}/\alpha_1 = 0.85$, $\beta_{12/\alpha_1} = \beta_{33/\alpha_1} = 0.929$, $\beta_{13}/\alpha_1 = \beta_{32}/\alpha_1 = -0.429$ $\beta_{22}/\alpha_1 = \beta_{23}/\alpha_1 = -0.35$, . The skew angles will be: cells 1, 4, 6: $\theta_1 = \theta_2 = 0.0°$, $\theta_3 = \theta_4 = \theta_5 = \theta_6 = 25.1°$; cells 2, 3: $\theta_1 = \theta_2 = 0.0°$, $\theta_3 = \theta_4 = \theta_5 = \theta_6 = 5°$; cell 5: $\theta_1 = \theta_2 = 0.0°$, $\theta_3 = \theta_4 = 1.72°$, $\theta_5 = \theta_6 = 31.88°$; cell 7: $\theta_1 = \theta_2 = 0.0°$, $\theta_3 = \theta_4 = 31.88°$, $\theta_5 = \theta_6 = 1.72°$ As can be seen, the increased cell rotation and lattice materials with larger difference in their CTEs allow us to design a lattice connecting titanium and Torlon substrates that has approximately the same skewness as in Example 2.

3.3 Design of advanced lattices

In this section, we show how to calculate CTEs of the lattices with more complicated shapes.

Example 4: Here, we design a four-cell titanium-magnesium angled lattice that can be used for mounting, for example, a cantilever on a satellite surface. Furthermore assume the first substrate is titanium and the second substrate is aluminum. Consider a skeleton of the lattice (fig. 3.8) that is symmetric with respect to the line OE. Suppose the right angle in the titanium substrate at the point O and the distances d and $r = d\sqrt{(2)}$ between substrates remain invariant when temperature changes. From the triangle COE, it is seen that extended CE is

$$CE^2 = d^2 + d^2 A_1^2 dT^2.$$

Neglecting the term with dT^2, we conclude that the right angle at the point C remains invariant with temperature and the CTE along CE $\overline{\alpha}_{CE} = 0$. It is obvious that the CTE along BC $\overline{\alpha}_{BC} = A_1$. Now, again neglecting the term with dT^2, the extended distance BE becomes

$$BE^2 = (\sqrt{2}d(1 + 0.5A_1 dT))^2,$$

which means that $\overline{\alpha}_{BE} = 0.5A_1$. From (3.1) applied to the cell with base triangle EBC with $\alpha = \beta = 45°$, $\gamma = 90°$, $L_1 = d\sqrt{2}$, $L_2 = L_3 = d$, we find $\theta_1 = \theta_2 = 28.5°$, $\theta_3 = \theta_4 = 0°$, $\theta_5 = \theta_6 = 20.2°$. Now, we design a cell based on an equilateral triangle ABD with $L_1 = L_2 = L_3 = 2d/\sqrt{3}$. Using formulae (2.12) and accounting for the extension along the segments BC and CO, we find $\overline{\alpha}_1/\alpha_1 = 1$, $\overline{\alpha}_2/\alpha_1 = 0.896$, and $\overline{\alpha}_3/\alpha_1 = -0.396$. From (3.1) applied to the cell based on an equilateral triangle, the skew angles are $\theta_1 = \theta_2 = 0°$, $\theta_3 = \theta_4 = 5.1°$, $\theta_5 = \theta_6 = 30.6°$. The sketch of the whole lattice is depicted in fig. 3.9.

Example 5: In this problem, we would like to design a non-planar lattice connecting two circular disks having the same radius R and distance from each other H. This configuration may occur in optical devices, such as telescopes. Let the lattice consists of n cells. It means that the angle $AO_1B = 2\phi = 360°/n$ (fig. 3.10). When the temperature changes, each disk expands axisymmetrically. That is, the CTE along AB $\alpha_{AB} = A_1$, and the CTEs along AT and BT are equal to each other: $\alpha_{AT} = \alpha_{BT}$. To find them, first we need to find the CTE along ST α_{ST}. To do this, we introduce a coordinate system O_1xyz as depicted in fig. 3.10. We will denote the coordinates of points and lengths of segments

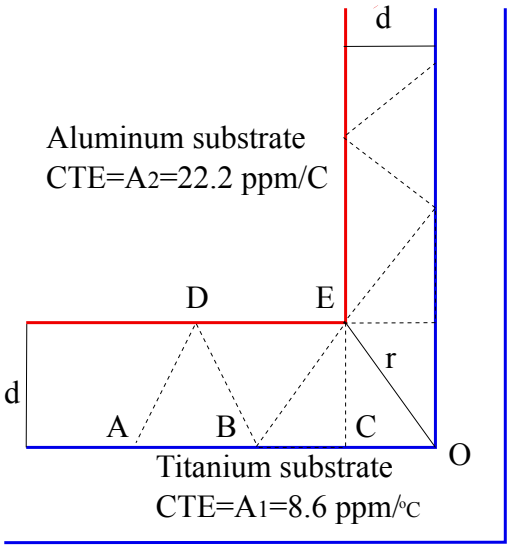

Figure 3.8: Problem 1. The skeleton of an angled titanium-magnesium alloy lattice to connect aluminum and titanium angled substrates.

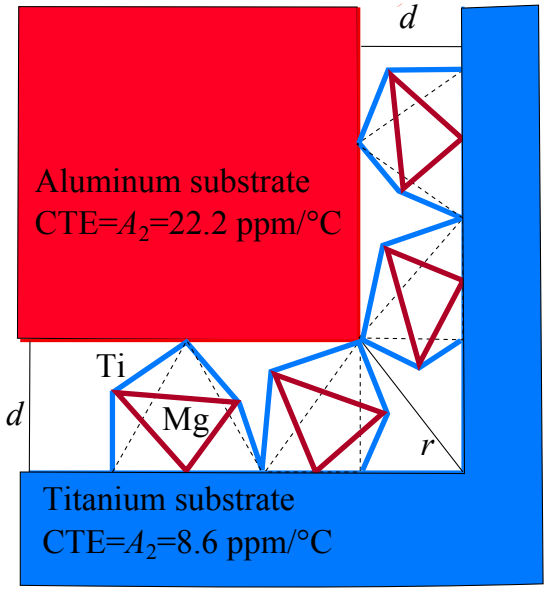

Figure 3.9: Problem 1. An angled titanium-magnesium alloy lattice to connect an aluminum cantilever to a titanium base.

at the initial state with subscript o, while after temperature changes, the same objects will be marked by subscript n: $S_o(R\cos\phi, 0, 0)$, $T_o(R, 0, H)$, $S_n(R(1 + A_1 dT)\cos\phi, 0, 0)$, $T_n(R(1 + A_2 dT), 0, H)$. Hence, neglecting the terms with dT^2, we find that $ST_o^2 = 4R^2\sin^4\phi/2 + H^2$ and

$$ST_n^2 = (4R^2\sin^4\frac{\phi}{2} + H^2)(1 + \frac{4R^2\sin^2\frac{\phi}{2}(A_2 - A_1\cos\phi)}{4R^2\sin^4\frac{\phi}{2} + H^2}dT).$$

Thus,

$$\alpha_{ST} = \frac{2R^2\sin^2\frac{\phi}{2}(A_2 - A_1\cos\phi)}{4R^2\sin^4\frac{\phi}{2} + H^2}. \tag{3.12}$$

On the other hand, consider the triangle ABT. Let $L_1 = AB$, $L_2 = L_3 = AT = BT$. From this triangle, neglecting terms with dT^2, we find

$$ST_n^2 = L_3^2 - 0.25L_1^2 + 2dT(l_3^2\alpha_{AT} - 0.25L_1^2 A_1).$$

Noting that $ST_o^2 = L_3^2 - 0.25L_1^2$ and comparing with (3.12), we find

$$\alpha_{AT} = \alpha_{BT} = \frac{2R^2 \sin^2 \frac{\phi}{2}(A_2 - A_1 \cos\phi)}{4R^2 \sin^4 \frac{\phi}{2} + H^2}(1 - \frac{L_1^2}{4L_3^2}) + \frac{L_1^2 A_1}{4L_3^2}.$$

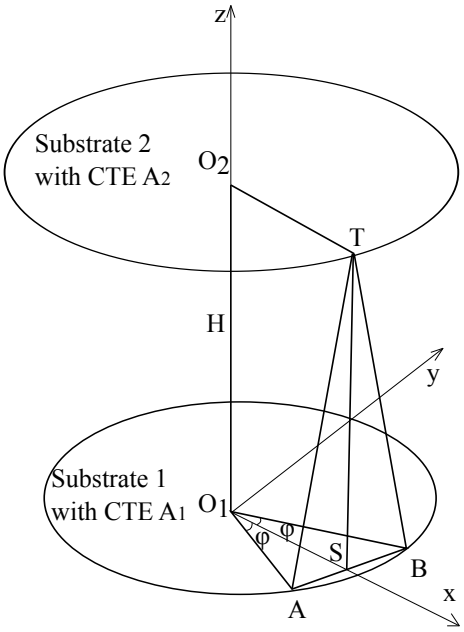

Figure 3.10: Problem 2. The base triangle for a cell of the lattice connecting two circular disks.

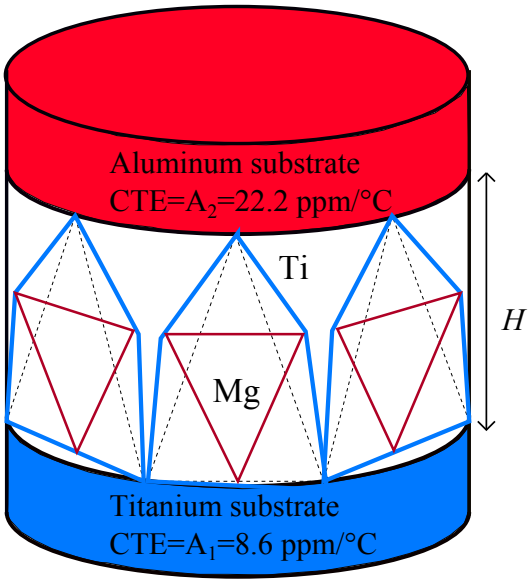

Figure 3.11: Problem 2. A non-planar titanium-magnesium alloy lattice connecting titanium and aluminum circular disks.

Now, suppose the lower circular disk is made of titanium, while the upper disk is made of aluminum. Suppose $R = H = 1$, $n = 6$; then $\phi = 30°$, $L_1 = 1$, $L_2 = L_3 = \sqrt{3 - \sqrt{3}}$. The lattice materials are titanium and magnesium alloy, so that $\alpha_{AT}/\alpha_1 = \alpha_{BT}/\alpha_1 = 0.38$. Solving equations (3.1) with $a = b = \arccos(0.444)$, and $c = 180° - a - b$, we find that $\theta_1 = \theta_2 = 0°$, $\theta_3 = \theta_4 = \theta_5 = \theta_6 = 18.0°$ (fig. 3.11). If the lattice is made of titanium and aluminum, the skew angles are $\theta_3 = \theta_4 = \theta_5 = \theta_6 = 22.5°$. The lattice with this material choice has lower structural efficiency, which will be shown in the section 3.5.

3.4 Adaptive lattices that compensate the thermal expansion of the substrates

Here, we design a lattice accounting for substrate thermal expansion in the normal direction and a lattice preventing shaft and collar sticking. Such lattices have negative CTE along their heights and are intermediate between adaptive lattices with passive control designed earlier and lattices for fine tuning and thermal actuation with active control. Similar to adaptive lattices, they eliminate or mitigate thermal stresses between two substrates with different CTEs; and they have desirable deflections of their vertices like lattices-actuators.

3.4.1 Lattice controlling total deflection

For previous lattices, the thermal expansion of the substrates in the direction perpendicular to the length of the lattice was assumed to be zero, and hence the lattice CTE along its height was equal to zero. Here, we design a three-cell lattice provided that the height of the two substrates and the lattice between them remains independent of temperature. Suppose the height of the first substrate is d_1, the second substrate is d_2, and the lattice itself is H (fig. 3.12).

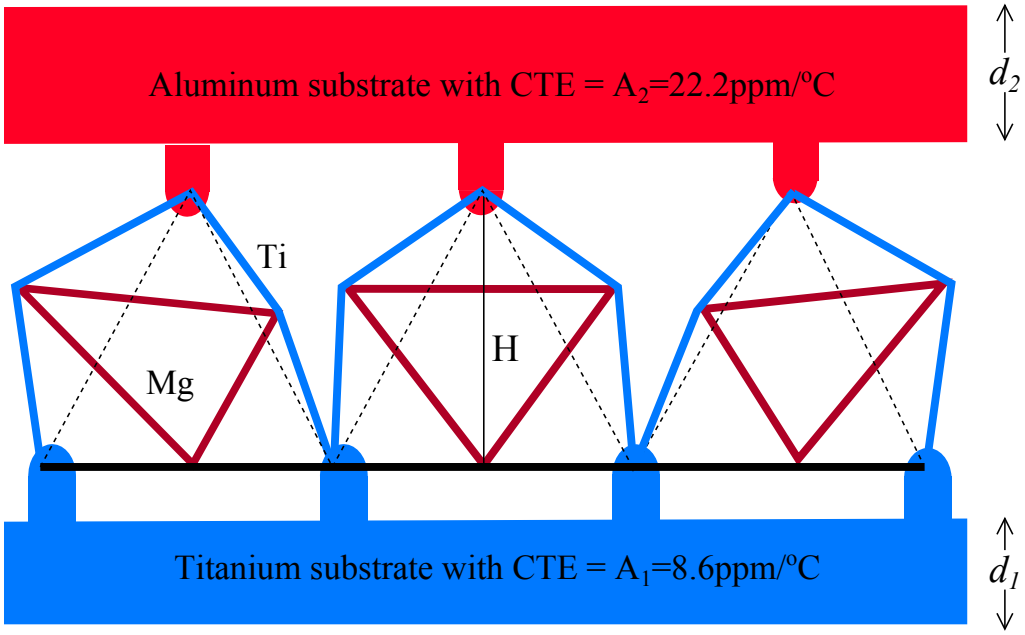

Figure 3.12: A magnesium alloy-titanium lattice connecting titanium and aluminum substrates (accounting for the vertical thermal extension of substrates).

Let α_{ij} denotes the CTEs in the cell with number i; the second index $j = 1$ along the line AC, $j = 2$ along the line CE, and $j = 3$ along the line AE (fig. 2.1). We consider both equilateral and isosceles right-angle base triangles to find out which is more suitable for the lattice. Following the approach described in Chapter 1 and accounting only for linear terms with α_{ij}, we find for an equilateral base triangle

$$\begin{aligned} \alpha_{11} = \alpha_{21} = \alpha_{31} = A_1, \\ \alpha_{12} = \alpha_{33} = 0.5A_2 - 0.25A_1 + 0.75\alpha_H, \\ \alpha_{13} = \alpha_{32} = 0.75A_1 - 0.5A_2 + 0.75\alpha_H, \\ \alpha_{22} = \alpha_{23} = 0.25A_1 + 0.75\alpha_H \end{aligned} \tag{3.13}$$

and for an isosceles right-angle base triangle

$$\begin{aligned} \alpha_{11} = \alpha_{21} = \alpha_{31} = A_1, \\ \alpha_{12} = \alpha_{33} = A_2 - 0.5A_1 + 0.5\alpha_H, \\ \alpha_{13} = \alpha_{32} = 1.5A_1 - 0.5A_2 + 0.5\alpha_H, \\ \alpha_{22} = \alpha_{23} = 0.5A_1 + 0.5\alpha_H \end{aligned} \tag{3.14}$$

where A_1 and A_2 are the CTEs of the first and second substrates, respectively, and α_H is the CTE along the height of the lattice (fig. 3.12). The total CTE in vertical direction of two substrates and the lattice between them is

$$\alpha_t = \frac{H\alpha_H + d_1A_1 + d_2A_2}{H + d_1 + d_2}. \tag{3.15}$$

As an example, consider a three-cell titanium-magnesium alloy lattice ($\alpha_1 = 8.6$ ppm/°C, $\alpha_2 = 28.0$ ppm/°C) connecting titanium ($A_1 = 8.6$ ppm/°C) and aluminum ($A_2 = 22.2$ ppm/°C) substrates. Suppose $d_1 = d_2 = 10$ mm, $H = 80$ mm and the total thickness of two substrates and the lattice remains independent of temperature ($\alpha_t = 0$). From formulae (3.15), we have $\alpha_H/\alpha_1 = -0.4475$. Because the first substrate and the lower CTE lattice material have the same CTE, $\alpha_{11}/\alpha_1 = \alpha_{21}/\alpha_1 = \alpha_{31}/\alpha_1 = 1$ and $t_1 = 0°$ in all cells. For equilateral base triangles, from formulae (3.13), we have $\alpha_{12}/\alpha_1 = \alpha_{33}/\alpha_1 = 0.7$, $\alpha_{13}/\alpha_1 = \alpha_{32}/\alpha_1 = -0.87$, $\alpha_{22}/\alpha_1 = \alpha_{23}/\alpha_1 = -0.0856$. Now, using the equations (3.1), we find in the left cell: $t_2 = 6.8°$, $t_3 = 39.1°$; in the middle cell: $t_1 = 0°$, $t_2 = t_3 = 23.8°$. The right cell is symmetric to the left cell with respect to the vertical line passing through the upper vertex of the middle cell (fig. 3.12).

This approach allows us to account for nonequal temperatures in the first and the

second substrates. Suppose the second substrate is heated 10% more compared to the first substrate. This is equivalent to the higher CTE of the second substrate: $A_2 = 22.2 * 1.1 = 24.42$ ppm/°C. In this case, $\alpha_H/\alpha_1 = -0.48$, $\alpha_{11}/\alpha_1 = \alpha_{21}/\alpha_1 = \alpha_{31}/\alpha_1 = 1$, $\alpha_{12}/\alpha_1 = \alpha_{33}/\alpha_1 = 0.68$, $\alpha_{13}/\alpha_1 = \alpha_{32}/\alpha_1 = -0.9$, $\alpha_{22}/\alpha_1 = \alpha_{23}/\alpha_1 = -0.11$. It means that in the left cell: $t_1 = 0°$, $t_2 = 7.0°$, $t_3 = 39.4°$; in the middle cell: $t_1 = 0°$, $t_2 = t_3 = 24.2°$.

For isosceles right-angle base triangles, from formulae (3.14), we have $\alpha_{12}/\alpha_1 = \alpha_{33}/\alpha_1 = 1.86$, $\alpha_{13}/\alpha_1 = \alpha_{32}/\alpha_1 = -0.0145$, $\alpha_{22}/\alpha_1 = \alpha_{23}/\alpha_1 = 0.28$. These CTEs can be reached if in the left cell $t_1 = 0°$, $t_2 = 23.77°$, $t_3 = -20°$; in the middle cell: $t_1 = 0°$, $t_2 = t_3 = 13.6°$. However, as shown in the next section, cells with negative skew angles have lower structural efficiency compared to the cells with positive skew angles. Hence, in this problem, cells based on an equilateral triangle are more appropriate.

3.4.2 Lattice between shaft and collar

Consider a structure consisting of a shaft and a collar made of materials with different CTEs. To prevent sticking when the shaft is heated, we design an adaptive lattice that has the CTE=0 of the collar on its outer contour and the CTE of the shaft at its inner contour. The collar is depicted as an external black hexagon and has CTE A_1, and the shaft is shown as a light-grey solid hexagon (fig. 3.13) with CTE A_2. The base triangle ABC has $\angle A = \angle B = 30°$. Denote $AO = OB = R$, then $OD = R\sqrt(3)/2$, $OC = R\sqrt(3)/3$, $DC = \sqrt(3)/6$. The CTE along the height $H = DC$ must compensate the CTE of the shaft along the OC, so

$$R\frac{\sqrt{3}}{3}(1 + A_2 dT) = R\frac{\sqrt{3}}{6}(1 - \alpha_H dT),$$

therefore, $\alpha_H = -2A_2$. On the other hand, from the triangle ABC

$$(2H(1 + \overline{\alpha}_2 dT)^2 - (H(1 + \alpha_H dT)^2 = (H\sqrt(3)(1 + A_1 dT)^2$$

and hence (neglecting nonlinear terms),

$$\overline{\alpha}_2 = \overline{\alpha}_3 = 0.25(3A_1 + \alpha_H)$$

Now, suppose that the shaft is made of aluminum with $A_2 = 22.2$ ppm/°C and the collar is not heated which is equivalent to zero CTE $A_1 = 0$ ppm/°C, then $\overline{\alpha}_2 = -11.1$ ppm/°C. As lattice materials we choose, for example, Kovar (with CTE 5.5 ppm/°C) for the external

cell hexagon and magnesium alloy (with CTE 28 ppm/°C) for the internal triangle. To avoid stresses due to thermal expansion mismatch, $\overline{\alpha}_1 = 0$ ppm/°C. From the equations (3.1), we find skew angles $t_1 = -18.3°$, and $t_2 = t_3 = 14.7°$ (fig. 3.13).

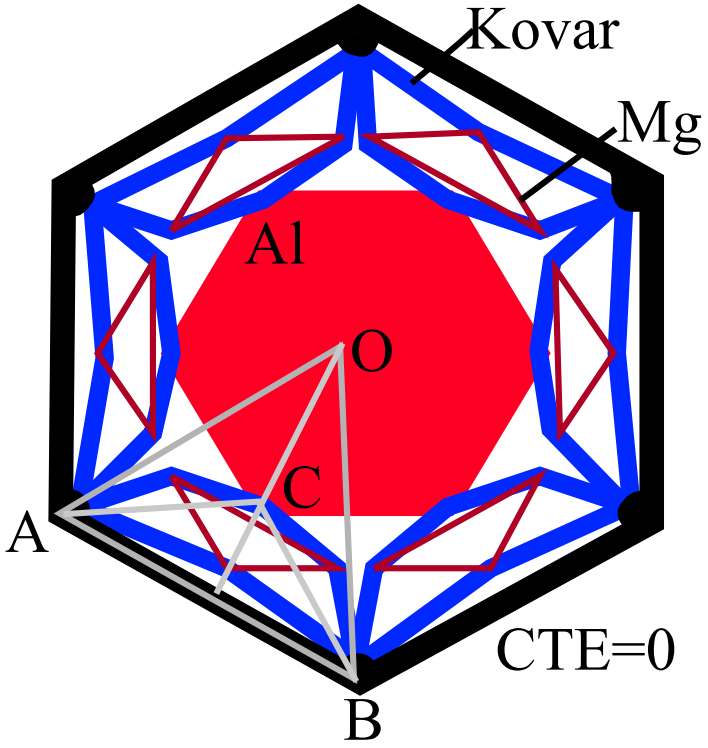

Figure 3.13: A Kovar-magnesium alloy lattice connecting aluminum shaft with zero thermal extension collar. A typical cell has a base triangle ABC. Point O is a centre of the shaft.

3.5 Structural efficiency

The lattices described in this thesis are intended to be structural elements that are subject to mechanical as well as thermal loading. We take a uniaxial load as archetypal and confine our analysis to that case. When a statically determined pin connected cell is loaded uniaxially, its members experience exclusively stretching or compressing. The uniaxial stiffness S_u links applied force N with resulting avarage strain $\overline{\varepsilon}$ as $N = S_u\overline{\varepsilon}$. The structural efficiency is defined as stiffness per mass M; here we consider dimensionless structural efficiency $P = S_u\rho/ME$ where ρ and E are the density and Young's modulus of a cell member, respectively, as was done in Steeves et al. (2007). Our goal is to

understand how the structural efficiency can be increased without a change of member materials or cross sectional area. The typical problem of designing a lattice to mitigate thermal expansion mismatch stresses has an infinite number of solutions: there are six angles to choose to achieve desirable effective CTEs along three lines. In this section, we are interested in choosing the six angles that provide the highest structural efficiency.

Consider an arbitrary cell with pin-jointed members under a uniaxial load as shown in fig. 3.14. The force N is applied to the top vertex of the cell, and F_i are the internal forces in members with lengths l_i, $i = \overline{1,9}$.

If the cell is in equilibrium, the forces in the members are

$$\begin{aligned} F_1 &= -\frac{N}{2}\frac{\cos(\alpha+\theta_6)}{\sin(\alpha+\theta_1+\theta_6)}, \quad F_2 = -\frac{N}{2}\frac{\cos(\beta+\theta_3)}{\sin(\beta+\theta_2+\theta_3)}, \\ F_3 &= \frac{N}{2}\frac{\cos(\theta_2)}{\sin(\beta+\theta_2+\theta_3)}, \quad F_4 = N\frac{\cos(\alpha-\theta_5)}{\sin(\gamma+\theta_4+\theta_5)}, \\ F_5 &= N\frac{\cos(\beta-\theta_4)}{\sin(\gamma+\theta_4+\theta_5)}, \quad F_6 = \frac{N}{2}\frac{\cos(\theta_1)}{\sin(\alpha+\theta_1+\theta_6)}, \\ F_7 &= -\frac{F_1\sin(\mu_2+\theta_1)+F_2\sin(\mu_2-\theta_2)}{\sin(\mu_1+\mu_2)}, \\ F_8 &= -\frac{F_1\sin(\mu_1-\theta_1)-F_2\sin(\mu_1+\theta_2)}{\sin(\mu_1+\mu_2)}, \\ F_9 &= -\frac{F_5\sin(\nu_2+\theta_5)+F_6\sin(\nu_2-\theta_6)}{\sin(\nu_1+\nu_2)} \end{aligned} \tag{3.16}$$

where angles μ_1, μ_2, ν_1, ν_2 are indicated in the fig. 3.14.

Suppose that the members with the lengths l_i, $i = \overline{1,6}$ have cross sectional area Λ_1 and are made from material with density ρ_1 and Young's modulus E_1, while the members with lengths l_i, $i = \overline{7,9}$ have cross section area Λ_2 and are made from material with density ρ_2 and Young's modulus E_2. Using the principle of virtual work, we can write

$$-N\delta + \frac{1}{\Lambda_1 E_1}\sum_{i=1}^{6} F_i^2 l_i + \frac{1}{\Lambda_2 E_2}\sum_{i=7}^{9} F_i^2 l_i = 0$$

where δ is the vertical deflection of the cell at the point of the force N application. Then, the resulting average strain of the cell $\overline{\varepsilon}$ will be

$$\overline{\varepsilon} = \frac{\delta}{h} = \frac{1}{\Lambda_2 E_2 N h}(Q\sum_{i=1}^{6} F_i^2 l_i + \sum_{i=7}^{9} F_i^2 l_i),$$

where h is the height of the cell and $Q = E_2\Lambda_2/E_1\Lambda_1$. The structural stiffness S_u in

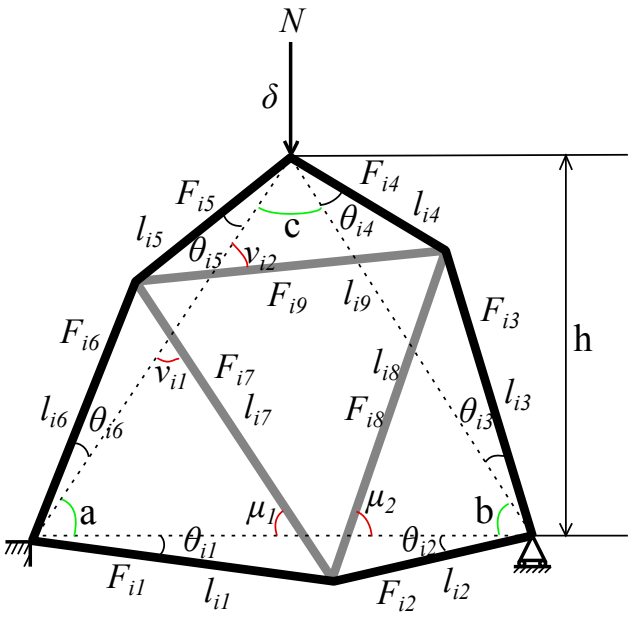

Figure 3.14: Arbitrary cell with applied force in uniaxial loading. The cell is supported by a pin at its left side and a roller at the right, head is applied vertically at the apex node.

uniaxial loading can be found as

$$S_u = \frac{N}{L_1 \bar{\varepsilon}} = \frac{N^2 \Lambda_2 E_2 h}{Q \sum_{i=1}^{6} F_i^2 l_i + \sum_{i=7}^{9} F_i^2 l_i}.$$

The mass of a cell per unit area of the lattice is given by

$$M = \frac{\rho_1 A_1 \sum_{i=1}^{6} l_i + \rho_2 A_2 \sum_{i=7}^{9} l_i}{L_1 h}.$$

Then, the structural efficiency P can be calculated as

$$P = \frac{S_u \rho_1}{M E_1} = N^2 \frac{Q h^2}{(Q \sum_{i=1}^{6} F_i^2 l_i + \sum_{i=7}^{9} F_i^2 l_i)(\sum_{i=1}^{6} l_i + \frac{\rho_2 E_1}{\rho_1 E_2} Q \sum_{i=7}^{9} l_i)}. \tag{3.17}$$

The maximum theoretical structural efficiency by this measure is $P = \frac{1}{3}$ (Steeves et al., 2007), for a perfectly triangulated lattice consisting of unskewed equilateral triangles and no high CTE members (that is, no internal triangles).

Analyzing formulae (3.16) and (3.17) and recalling that θ_i, $i = \overline{1,6}$ determine the three CTEs in the cell, we conclude that increasing the skew angles θ_3 and θ_6 (making the cell more "stout") increases the structural efficiency. For this purpose, introduce

coefficients of stoutness k_j, $j = 1, 2, 3$: $\theta_2 = k_1\theta_1$, $\theta_3 = k_2\theta_4$, $\theta_6 = k_3\theta_5$. Note that the solutions to the problems considered previously were obtained for $k_1 = k_2 = k_3 = 1$.

When k_j, $j = 1, 2, 3$ increase, the neighbouring cells can overlap each other or the lengths of the members l_3 and l_6 can become substantially smaller than l_4 and l_5, which can lead to prohibitive manufacturing difficulties for the cell. To avoid this, introduce length ratios $r_1 = l_1/l_2$, $r_2 = l_4/l_3$, $r_3 = l_5/l_6$ to limit the increase of skew angles θ_3 and θ_6 even though they do not cause overlapping.

Finally, in this work, lattices with cells having approximately the same structural efficiency are designed. It means that a cell with rather small θ_3, θ_6 and length ratios needs not be further optimized if other cells in the lattice are already optimized and have lower structural efficiency. The structural efficiency of the whole lattice is taken equal to the minimum structural efficiency among all cells. Now, a general algorithm for design of a lattice structure with increased structural efficiency can be formulated:

1. Design the lattice for $k_1 = k_2 = k_3 = 1$ described previously in Chapter 2 (Section 2.3); calculate the skew angles of all cells of the lattice and its structural efficiency.

2. Choose the increments Δk_j $j = 1, 2, 3$ for the coefficients of stoutness. If the skew angles adjacent to a side of base triangle are equal to zero, the coefficient of stoutness related to this side is 1.

3. Find the solution to the problem at $k_j + \Delta k_j$, calculate the skew angles of all cells and the structural efficiency of each cell.

4. If cells do not overlap each other and length ratios r_j in all cells do not exceed limits stipulated by the manufacturing process, increase $k_j = k_j + \Delta k_j$ and go to the previous step.

5. If there is at least one pair of cells overlapping each other or the length ratios of at least one cell exceeds the set limit, decrease the increment Δk_j for these cells and go to step 3.

6. The process halts if structural efficiency of cells designed for smaller Δk_j exceeds the structurally efficiency of already optimized cells or the new structural efficiency is not significantly better than the structural efficiency from the previous step.

While this algorithm does not generate rigorously optimal geometries, the term "optimal" is used loosely to describe the results. In the examples below, we consider titanium-magnesium alloy lattices with cells based on equilateral triangles, areas $\Lambda_1 = \Lambda_2$, $E_1 = 116.3$ GPa (titanium), $E_1 = 45.0$ GPa (magnesium alloy), and hence $Q = 0.387$.

Example 6: Titanium and magnesium alloy substrates can be connected by the titanium and magnesium alloy one-row lattice depicted in fig. 3.5. The structural efficiency of the lattice is $P = 0.0899$, which is very low. Another solution of the same problem involving a two-row lattice has the structural efficiency of the cells in the lower row of the lattice (fig. 3.6) is $P = 0.1382$, and of the cells in the upper row is $P = 0.1346$. The structural efficiency improvement of the two-row lattice with $k_1 = 1$ and $k_2 = k_3 = 2$ for all cells results with $P = 0.1562$ for the cells in the lower row ($\theta_1 = \theta_2 = 0°$, $\theta_3 = 24.8°$, $\theta_4 = 12.4°$, $\theta_5 = 12.4°$, $\theta_6 = 24.8°$) and $P = 0.1496$ for the cells in the upper row ($\theta_1 = \theta_2 = 0°$, $\theta_3 = 6.5°$, $\theta_4 = 3.25°$, $\theta_5 = 20.2°$, $\theta_6 = 40.4°$ for the left cell). So, the lattice's improved structural efficiency is $P = 0.1496$. (fig. 3.15). In this solution, the

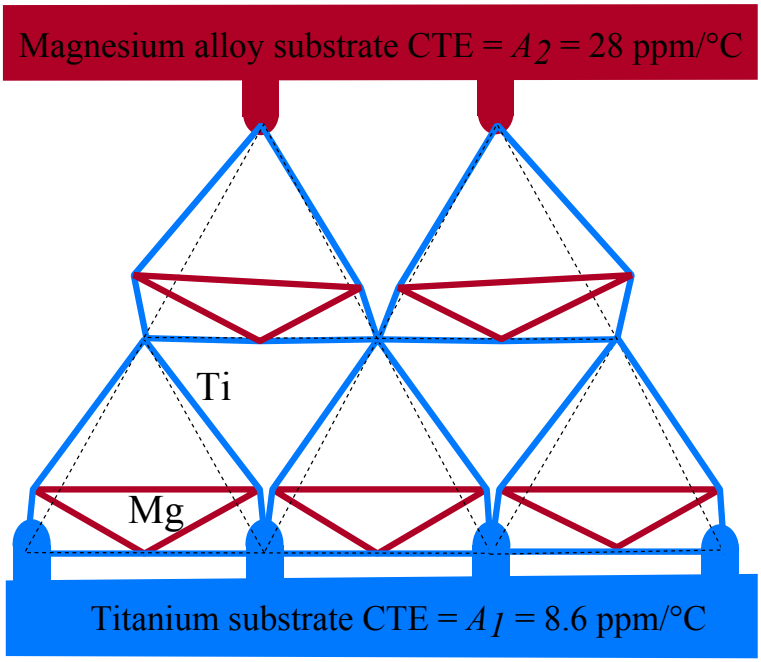

Figure 3.15: Improved structural efficiency of two-row titanium-magnesium alloy lattice connecting titanium and magnesium alloy substrates.

structural efficiency is improved by 66% compared to the one-row solution.

Example 7: Using the formula (3.17), calculate the structural efficiency of the non-planar lattice presented in Problem 2 section 3.3 (fig. 3.11) can be calculated; it is P=0.191. After improvement, the structural efficiency increases to P=0.211. The lattice with increased structural efficiency is depicted in fig. 3.16. Its skew angles are $\theta_1 = \theta_2 = 0°$, $\theta_3 = 23.2°$, $\theta_4 = 11.6°$, $\theta_5 = 11.6°$, $\theta_6 = 23.2°$. If titanium and aluminum are chosen as lattice materials, the initial structural efficiency is P=0.143, and after improvement it becomes P=0.161, which is significantly lower than in the titanium-magnesium lattice.

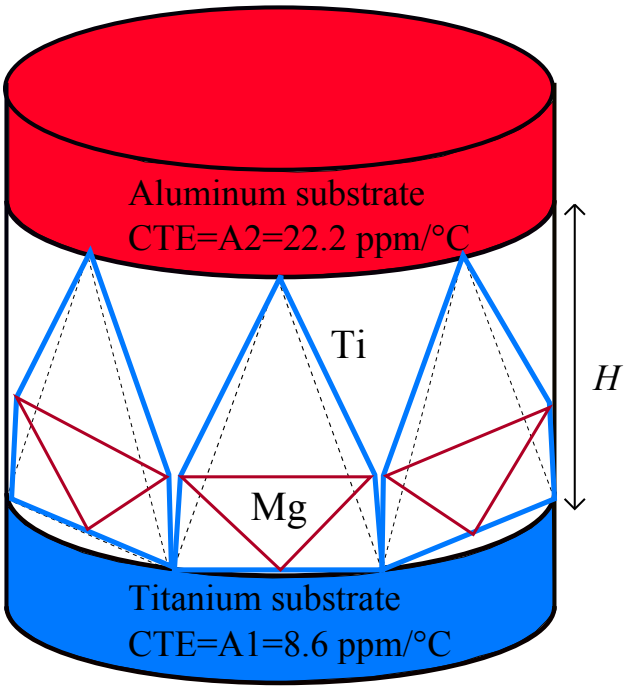

Figure 3.16: Optimized non-planar titanium-aluminum lattice connecting titanium and aluminum circular disks.

Example 5: The cells of the lattice presented in Example 2 of this Chapter (fig. 3.7) have the following structural efficiency: for cells 1, 4, and 6, $P = 0.077$; for cells 2 and 3, $P = 0.255$; for cells 5 and 7, $P = 0.133$. Hence, to improve the structural efficiency of the whole lattice, the structural efficiency of the cells 1, 4, and 6 must be increased: if $k_1 = 1$, $k_2 = k_3 = 5$, $\theta_1 = \theta_2 = 0°$, $\theta_3 = \theta_6 = 48.34°$, $\theta_4 = \theta_5 = 9.67°$, then $P = 0.0995$ (fig. 3.17). As it is seen, the structural efficiency increased substantially but remains much lower than in previous examples, which is a consequence of cell rotation. Note that the results of all of these calculations show that the lattice designs generating unusual multifunctional thermal properties retain significant proportions of the theoretically possible structural efficiency while remaining stress-free. This is in strong contrast to other anisotropic tailorable systems which are either compliant (Jefferson et al., 2009) or generate thermal stresses (Harris, 2003; Zhang et al., 2013).

3.6 Concluding remarks

In this chapter, lattices of more complicated configuration than the lattices considered in Chapter 2: a right-angled cantilever joint and a cylindrical adapter for optical lenses

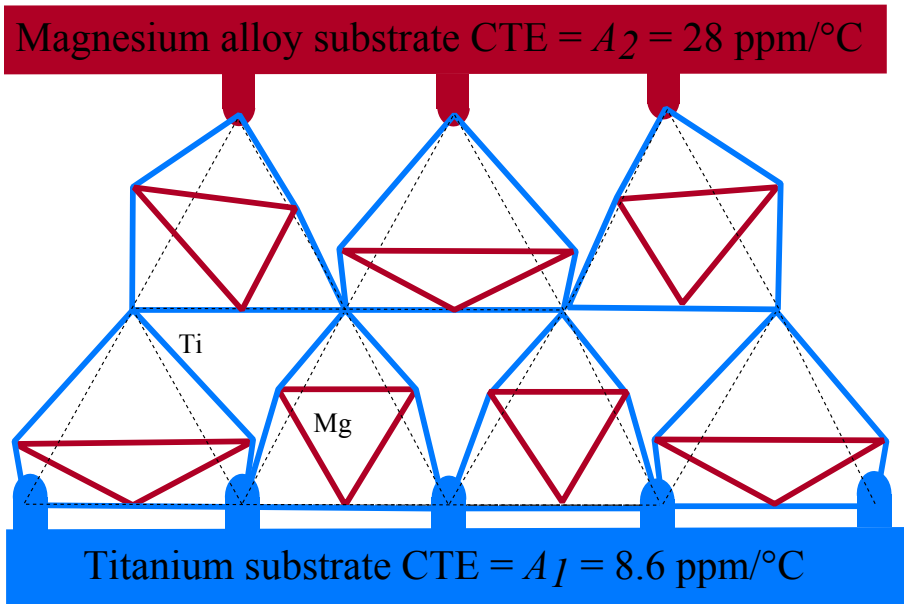

Figure 3.17: Optimized seven-cell titanium-aluminum lattice connecting titanium and Torlon substrates.

were designed. Also, a method to connect substrates with a greater differences between their CTEs by using two-row lattices with cell rotation was elaborated. To design such lattices, we allowed non-zero changes in the cell heights. This approach opened new opportunities for controlling the total deflection of two substrates and a lattice between them (the substrates can be parallel to each other or represent a joint such as a shaft a collar). The design of these lattices made it clear that anisotropic bimaterial lattices can be used not only for accommodation of thermal expansion but also for imposing geometric changes. In other words, the issues considered in this chapter enabled us to attain insight and experience that are necessary for the design of lattices as mechanisms for thermal actuation and fine tuning, which will be considered in the next chapter.

Chapter 4

Actuation through bimaterial lattices

In this chapter, we examine the theoretical capability of bimaterial lattices as active systems for fine tuning and thermal actuation [1] [2] [3]. It is possible to design a lattice connecting two substrates without thermal expansion mismatch stresses and with desirable deflections at some of its vertices. Actuation, where defined displacements are imposed between specific locations, is a natural extension to this. However, the deflections caused by thermal expansions are small. Hence, we need to identify methods to amplify these displacements to enable useful actuation. In the previous chapters, we considered lattices with cells in which the inner triangle material has a higher CTE than the outer hexagon ($\alpha_2 > \alpha_1$). Now, to increase the lattice capabilities, a cell where the outer hexagon material has a higher CTE than the inner triangle ($\alpha_2 < \alpha_1$) is also used. In addition, it is supposed that skew angles $\theta_1 = \theta_2 = t_1$, $\theta_3 = \theta_4 = t_2$, $\theta_5 = \theta_6 = t_3$, because the different skew angles adjacent to the same side of the based triangle may be beneficial in the structural efficiency problem which is not considered in this chapter. Also, it is supposed that $t_2 = t_3$ (fig. 4.1) because in actuators designed in this chapter the substrates have the same CTEs (similar case was considered for the cells in the lower row of two-row lattices).

Fig. 4.2 shows the range $\overline{\alpha}_2/\alpha_1 = \overline{\alpha}_3/\alpha_1$ of titanium-magnesium alloy cells based on

[1] M M Toropova and C A Steeves. Controlling thermal deformation through the use of lattice structures. 62nd CASI Aeronautics Conference and AGM 3rd CARDN Conference, Montreal, Canada, May 19-21, 2015.

[2] M M Toropova and C A Steeves. Thermal actuation through bimaterial lattices. ASME Conference on Smart Materials, Adaptive Structures and Intelligent Systems SMASIS, Colorado Springs, USA, September 21-23, 2015.

[3] M M Toropova and C A Steeves. Bimaterial lattices as thermal adapters and actuators. Smart Materials and Structures (accepted), 2016.

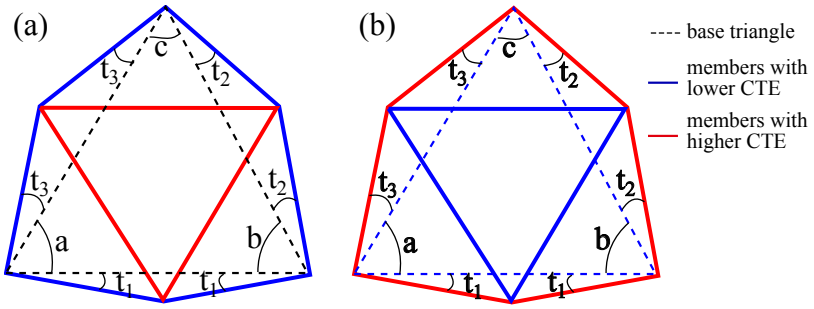

Figure 4.1: (a) Bimaterial cell with $\alpha_2 > \alpha_1$. (b) Bimaterial cell with $\alpha_2 < \alpha_1$. The skew angles adjacent to the same side of the base triangle are equal to each other.

an equilateral triangle when the internal triangle is made of magnesium alloy and the surrounding hexagon is made of titanium (dotted line). We consider here a titanium alloy (Ti-6Al-4V Grade 5) with CTE 8.6 ppm/°C and a magnesium alloy (of type AZ81A) with CTE 28.0 ppm/°C. The solid line is for the cell with a titanium triangle and a magnesium alloy hexagon. The skew angle t_1 was assumed equal to zero with $\overline{\alpha}_1/\alpha_1 = 1$ and also $t_2 = t_3$. Such cells will be used in actuator design. The range of $\overline{\alpha}_2/\alpha_1 = \overline{\alpha}_3/\alpha_1$ for other cell materials with different ratios α_2/α_1 is shown in fig. 4.3 as a colored region. The black boundary of the region corresponds to $t_2 = t_3 = -15°$, and the grey boundary corresponds to $t_2 = t_3 = 35°$.

Similar curves for cells based on an isosceles right-angle triangle are shown in fig. 4.4. The range of $\overline{\alpha}_2/\alpha_1 = \overline{\alpha}_3/\alpha_1$ in cells based on isosceles right angle triangles for different ratios α_2/α_1 of other cell materials is shown in fig. 4.5 as a colored region. The black boundary of the region corresponds to $t_2 = t_3 = -22.5°$, and the grey boundary corresponds to $t_2 = t_3 = 35°$. The range of CTE in cells based on a right-angle triangle is wider than the analogous range for cells based on an equilateral triangle. In general, if $\alpha_2 > \alpha_1$, the increase of skew angles leads to the decrease of CTE with transition to negative zone. If $\alpha_2 < \alpha_1$, the relation between the CTE and skew angles is inverse.

4.1 Fine tuning of an optical system connector

A non-planar lattice connecting two circular disks and eliminating displacements due to thermal expansion was designed in Chapter 3 (fig. 3.11). Here, we show how the lattice of this shape can be used for fine tuning of optical lenses represented by circular disks. To provide the widest possible tuning range, the cells in the lattice must have maximal thermal expansion along their heights. To enable such a tuning system, it is necessary to

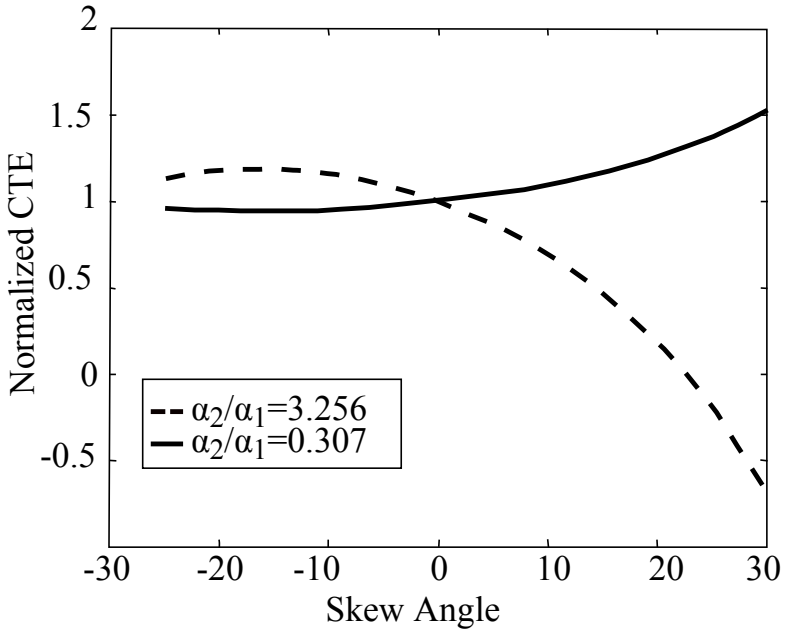

Figure 4.2: Ranges $\overline{\alpha}_2/\alpha_1 = \overline{\alpha}_3/\alpha_1$ of titanium-magnesium alloy cells based on an equilateral triangle with $t_1 = 0°$. The solid line corresponds to the cell with a titanium inner triangle and a magnesium alloy outer hexagon, while the dotted line corresponds to the magnesium alloy inner triangle and titanium outer hexagon.

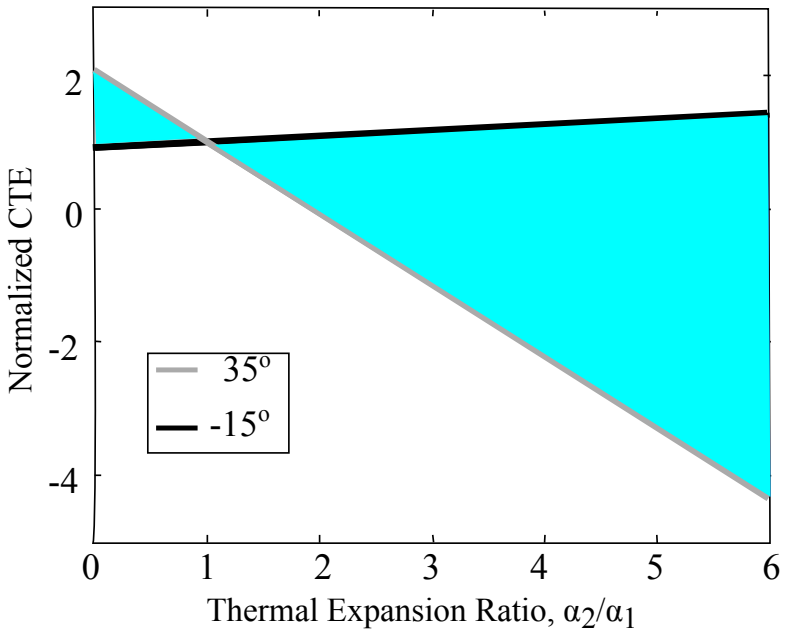

Figure 4.3: Range of $\overline{\alpha}_2/\alpha_1 = \overline{\alpha}_3/\alpha_1$ in a cell based on an equilateral triangle with $t_1 = 0°$ as a function of the ratio of lattice material CTEs α_2/α_1.

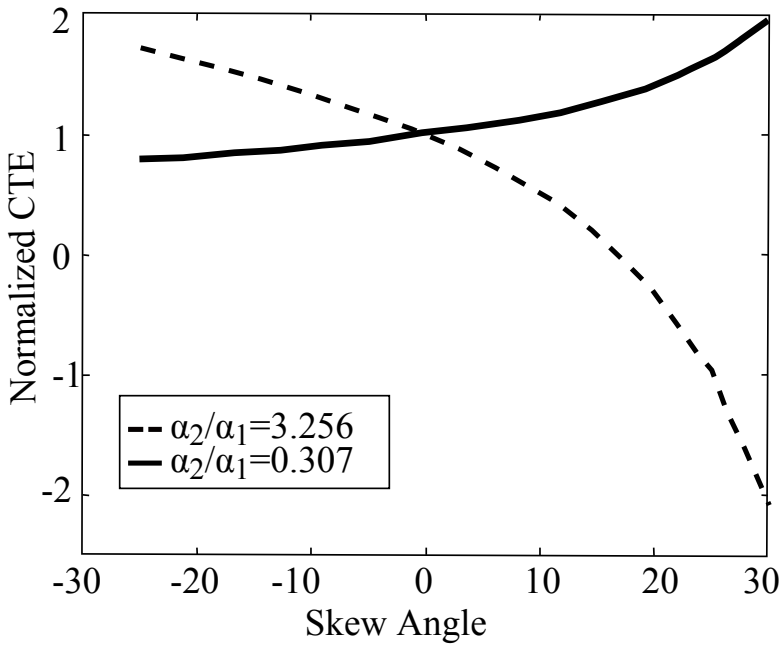

Figure 4.4: Ranges $\overline{\alpha}_2/\alpha_1 = \overline{\alpha}_3/\alpha_1$ of titanium-magnesium alloy cells based on an isosceles right-angle triangle with $t_1 = 0°$. The solid line corresponds to a cell with a titanium inner triangle and a magnesium alloy outer hexagon, while the dotted line corresponds to the magnesium alloy inner triangle and titanium outer hexagon.

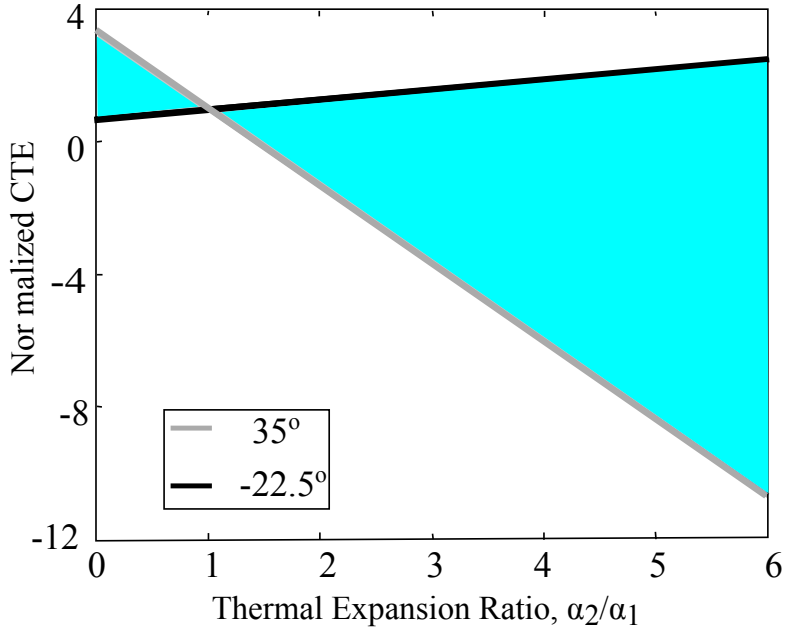

Figure 4.5: Range of $\overline{\alpha}_2/\alpha_1 = \overline{\alpha}_3/\alpha_1$ in a cell based on an isosceles right-angle triangle with $t_1 = 0°$ as a function of the ratio of lattice material CTEs α_2/α_1.

induce different temperatures in the cells of the lattice. The lattice is axisymmetric and

$$L_1 = 2R\sin\frac{\phi}{2}, \quad L_2 = L_3 = \sqrt{4R^2\sin^2\frac{\phi}{2} + H^2}, \quad a = b = \arccos\frac{0.5L_1}{L_2}$$

where $\phi = 2\pi/n$. The cells are designed based on isosceles triangles with $\overline{\alpha}_{i2} = \overline{\alpha}_{i3}$ in all cells where $i = \overline{1,n}$ is a cell number and n is the total number of lattice cells .

If both substrates have the same CTE, the maximal deflection can be larger, so let $A_1 = A_2$. Suppose $R = 10$ cm, $H = 1$ cm, and $n = 6$, then the angles in a cell base triangle are $a = b = 18.49°$. Suppose the substrate material is magnesium alloy ($A_1 = A_2 = 28$ ppm/°C). As lattice materials we choose Kovar (iron-nickel-cobalt alloy with $\alpha_2 = 5.5$ ppm/°C) for the internal triangles and magnesium alloy ($\alpha_1 = 28$ ppm/°C) for the outer hexagons - this will provide us with $\overline{\alpha}_{i1}/\alpha_1 = 1$ while the values of $\overline{\alpha}_{i2}/\alpha_1$ and $\overline{\alpha}_{i3}/\alpha_1$ will be higher than in a cell with an internal magnesium alloy triangle and an outer titanium hexagon (examples of the analogous situation are illustrated by fig. 4.2 and fig. 4.4). Because α_H depends linearly on α_{i2} and α_{i3}, the value of α_H will also be higher. The maximum values of α_{i2} and α_{i3} can be reached if the skew angles $t_2 = t_3 \to a = b = 18.5°$. For example, if $t_2 = t_3 = 15°$, then $\alpha_{i2} = \alpha_{i3} = 82.9$ ppm/°C. From the formula $\alpha_H = (\alpha_{i2} - A_1\cos^2 a)/\sin^2 a$, we obtain $\alpha_H = 574$ ppm/°C. For $H = 1$ cm and $\Delta T = 100$°C, $\Delta H = H\alpha_H\Delta T = 0.574$ mm. Thus, if we supply the temperature $\Delta T = 100°$ to the cells with number 1 and 6, the temperature $\Delta T = 50°$ to the cells with number 2 and 5, and the temperature $\Delta T = 0°$ to the cells with number 3 and 4, the upper disk will tilt (fig. 4.6) with angle 0.164°. Smaller skew angles or supplied temperature can provide even finer tuning.

4.2 Thermal actuators

Broadly, the lattices described here and in previous chapters exhibit the ability to change shape in a precise and controlled manner during temperature changes. Consequently, they can be used as thermal actuators as well as adapters. However, the thermal deflections are small and demand significant amplification. In Chapter 3, it was shown that lattice materials with a higher ratio α_2/α_1 and two-row lattices with cell rotation can connect substrates with larger differences in the CTEs of their materials. These techniques can be used in the design of actuators, but our goal is to provide even higher amplification. This problem was solved in several ways: choosing isosceles right angle base triangles that provide a wider range of CTEs compared to equilateral base triangles (fig. 4.4), removing intermediate connections to the first substrate between lattice cells, selecting

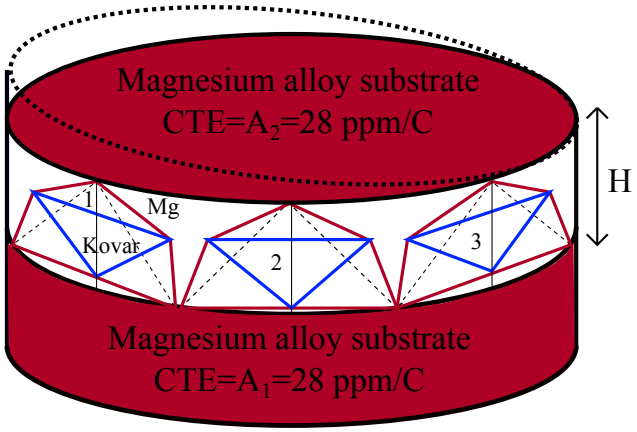

Figure 4.6: Non-planar Kovar-magnesium alloy lattice for fine tuning of optical lenses. Lattice materials are chosen to provide positive CTE along the height of each cell. Skew angles are chosen to maximize the CTE. The upper disk tilts when different temperatures are supplied to different cells causing their different vertical extensions.

materials with the same CTEs for both substrates, and choosing in some cells lattice materials with $\alpha_2/\alpha_1 > 1$ (type I cells) providing negative deflection and in other cells $\alpha_2/\alpha_1 < 1$ (type II cells) providing positive deflection. All lattice-based actuators are designed based on isosceles right-angled triangles with $a = b = \pi/4$ and $c = \pi/2$ because such cells have higher absolute values of CTEs compared to, for example, cells based on equilateral triangles (fig. 4.3, fig. 4.5). We shall next consider the design of a switch, tweezers, and a valve.

4.2.1 Thermal switch

A thermally actuated switch consists of two cells connected to a pair of substrates. One substrate (substrate 1) is stationary, while substrate 2 can rotate. The concept is that the rotating substrate can be used to make or break contact in an electrical circuit. For example, such a switch may be used to control a cooling system that operates when a trigger temperature is reached. The left cell is of type I, while the right cell is of type II (fig. 4.2, fig. 4.4). The skew angles in both cells are chosen so that the CTE along the height in the left cell has a negative value and the CTE in the right cell has a positive value. As a result, when temperature increases the height of the left cell decreases while the height of the right cell increases, and the second substrate rotates raising the right end and lowering the left end. The new position of the second substrate is depicted in

fig. 4.7 with a dashed contour. The lattice is pin-connected to the first substrate only at the left vertex of the left cell and the right vertex of the right cell (fig. 4.7). This allows us to connect the lattice to substrates with the CTEs higher than the lattice made of type I cells and lower than the lattice made of type II cells. If the materials of both substrates have the same CTEs, the CTEs along the lateral sides of base triangles are equal to each other.

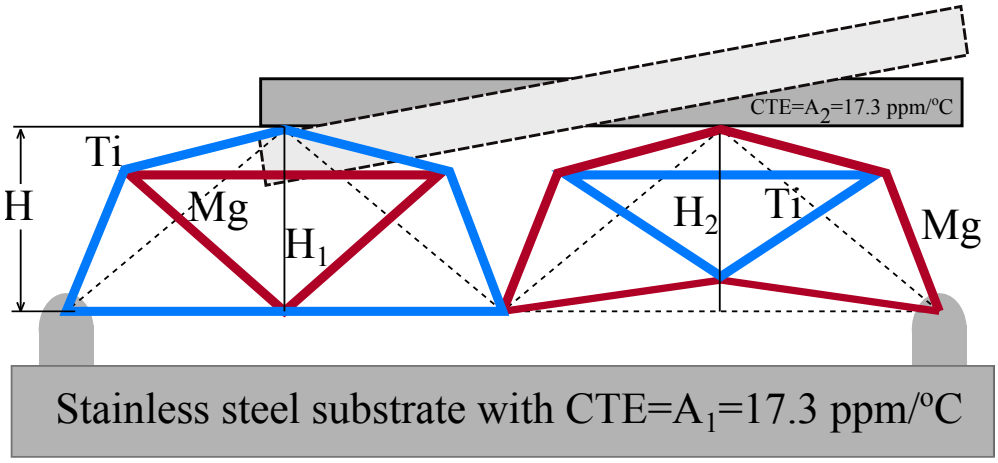

Figure 4.7: A two-cell titanium-magnesium alloy lattice having connections with substrates free of thermal stress and behaving like a thermally driven switch.

Thus, applying the technique developed in Chapters 2 and 3 for a two-cell lattice with isosceles right-angled base triangles and using the same notation for lattice CTEs as in section 2.3, we obtain

$$\begin{aligned} \alpha_{11} + \alpha_{21} &= 2A_1 = 2A_2, \\ \alpha_{12} = \alpha_{13}, \quad \alpha_{22} &= \alpha_{23}, \\ \alpha_{H1} &= 2\alpha_{12} - \alpha_{11}, \\ \alpha_{H2} &= 2\alpha_{22} - \alpha_{21} \end{aligned} \tag{4.1}$$

where α_{H1} and α_{H2} are the CTEs along the heights of the left and the right cells, respectively (fig. 4.7). Note that the first equation of (4.1) presents a restriction on the materials of substrates and cells in terms of their CTEs. We have to choose the skew angles that provide $\alpha_{H1} < 0$ in the left cell and $\alpha_{H2} > 0$ in the right cell.

As an example, consider a lattice made from titanium and a magnesium alloy. The internal triangle of its left cell is made of magnesium alloy and the external members are made of titanium, so that $\alpha_2/\alpha_1 = 3.256$. From the equations (4.1) it is seen that

$\alpha_{H1} < 0$ is smaller when $\alpha_{12} = \alpha_{13}$ are smaller. So, we select skew angles $t_1 = 0°$, and $t_2 = t_3 = 35°$, (fig. 4.4) and then from the equations (3.1), we get $\alpha_{11}/\alpha_1 = 1$, $\alpha_{12}/\alpha_1 = \alpha_{13}/\alpha_1 = -4.27$, and from the third equation (4.1), $\alpha_{H1}/\alpha_1 = -9.54$ implying $\alpha_{H1} = -82.0$ ppm/°C. This is a very large negative CTE. In the right cell, the internal triangle is made from titanium and the hexagon members from a magnesium alloy ($\alpha_2/\alpha_1 = 0.307$), hence to get larger $\alpha_{H2} > 0$, we can choose skew angles as $t_1 = -11°$, $t_2 = t_3 = 35°$. Then, using the equations (3.1), we have $\alpha_{21}/\alpha_1 = 0.929$, $\alpha_{22}/\alpha_1 = \alpha_{23}/\alpha_1 = 2.5892$ and $\alpha_{H2}/\alpha_1 = 4.292$ or $\alpha_{H2} = 119$ ppm/°C. Similarly, this is a very large positive CTE. If we set $t_1 = 0°$ in the right cell, the CTE of substrate material must be (4.1) $A_1 = A_2 = 0.5(8.6 + 28.0) = 18.3$ ppm/°C. However, there is no conventional material with such a CTE. Hence, we need to correct slightly the skew angle t_1 to increase either α_{11} or α_{21} to get the substrate CTE, for example, $A_1 = A_2 = 17.3$ ppm/°C which corresponds to the CTE of austenitic stainless steel (304). This is easier to do with the right cell because all its normalized CTEs are greater than 1. Thus, the chosen skew angles provide lattice connection to the stainless steel substrates without thermal expansion mismatch stresses. Different skew angles t_1 in both cells would allow us to connect the switch without thermal expansion mismatch stresses to substrates with other values of their CTEs. The displacement of the right end of the second substrate is

$$\Delta H = L\tan\phi - |\Delta H_1| = 2L_1\frac{|\Delta H_1| + \Delta H_2}{L_1} - |\Delta H_1| = \\ |\Delta H_1| + 2\Delta H_2 = H\Delta T(|\alpha_{H1}| + 2\alpha_{H2})$$

where $|\Delta H_1|$, ΔH_2 are deflections of the left and right cell apexes, $L = 2L_1$ is a switch length, and ϕ is a rotation angle of the second substrate (fig. 4.8). If $\Delta T = 100°C$, $\Delta H/H100\% = 3.2\%$. We can see that the lattice behaves like a thermally-driven actuator.

Now, we calculate the blocking force associated with the lattice. The blocking force is the force that completely restricts motion of the actuator and qualifies the overall actuation capability of the system. In case of the switch, the blocking force is applied to the right end of the second substrate that keeps it at zero deflection. This force P creates loads $P_1 = P$ and $P_2 = -2P$ on the vertices of the left and the right cells of the switch, respectively (fig. 4.9). Denote as F_{ij} the internal forces in members with lengths l_{ij}, with $i = 1, 2$ the cell number and $j = \overline{1,9}$ the member number.

In the left cell, $i = 1$ and in the right cell $i = 2$. The second index j indicates a number of a member in each cell that has the length l_{ij}. Fig. 4.10 shows the cell with number i. Let $F_{ij} = NG_{ij}$ where $N = P$ if $i = 1$ and $N = -2P$ if $i = 2$. In this problem,

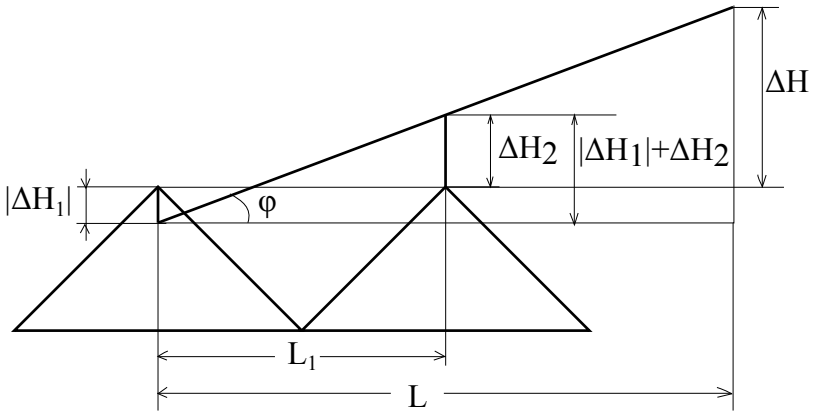

Figure 4.8: Sketch of switch kinematics. $|\Delta H_1|$, ΔH_2 are deflections of the left and right cell apexes, while ΔH is a deflection of the second substrate right end.

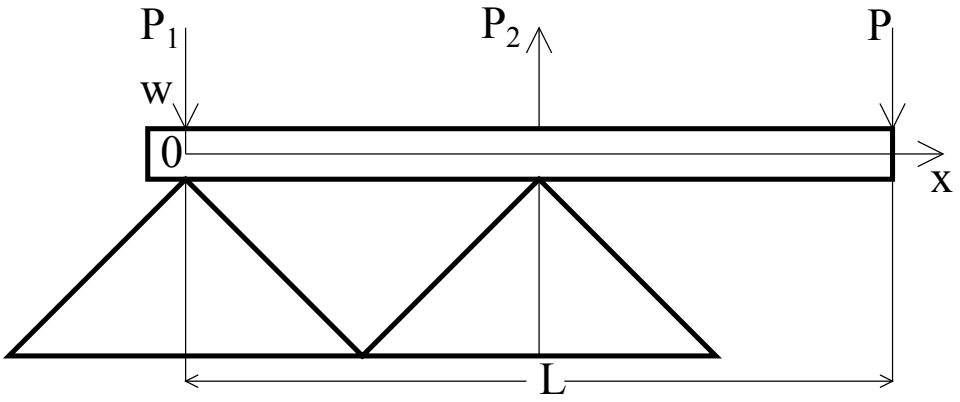

Figure 4.9: Sketch of configuration of forces associated with the blocking force P applied to a thermal switch.

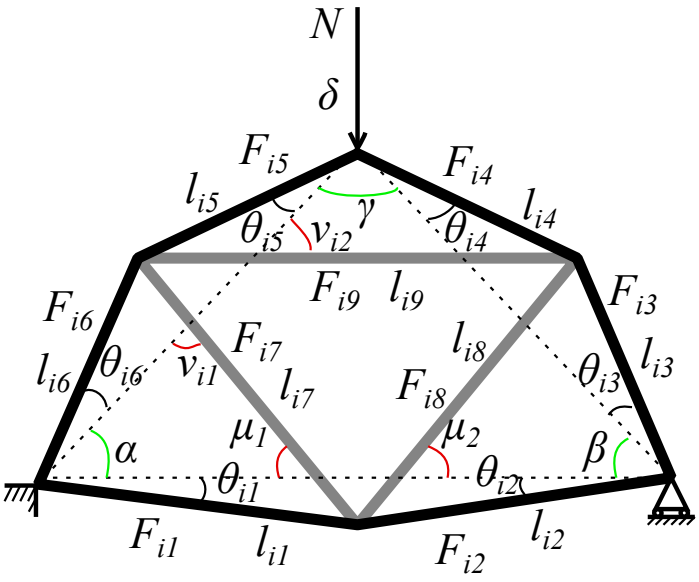

Figure 4.10: Nomenclature of forces, lengths and angles for an arbitrary cell subject to applied force N in uniaxial loading.

denote $\theta_{i1} = \theta_{i2} = \tau_{i1}$ and $\theta_{i3} = \theta_{i4} = \theta_{i5} = \theta_{i6} = \tau_{i2}$ where θ_{ik} is a skew angle with number k in the cell with number i, $m = \overline{1,6}$. Then, similarly to what was found in Section 3.5, equation (3.16),

$$\begin{aligned}
G_{i1} = G_{i2} &= -\frac{1}{2}\frac{\cos(\pi/4 + \tau_{i2})}{\sin(\pi/4 + \tau_{i1} + \tau_{i2})}, \\
G_{i3} = G_{i6} &= \frac{1}{2}\frac{\cos(\tau_{i1})}{\sin(\pi/4 + \tau_{i1} + \tau_{i2})}, \\
G_{i4} = G_{i5} &= \frac{\cos(\pi/4 - \tau_{i2})}{\cos(2\tau_{i2})}, \\
G_{i7} = G_{i8} &= -G_{i1}\frac{\cos(\tau_{i1})}{\cos(\mu_i)}, \\
G_{i9} &= -\frac{G_{i5}\sin(\nu_{i2} + \tau_{i2}) + \sin(\nu_{i2} - \tau_{i2})}{\sin(\nu_{i1} + \nu_{i2})},
\end{aligned} \tag{4.2}$$

where the angles μ_i, ν_{i1}, ν_{i2} indicated in fig. 4.10 are given by

$$\mu_i = \pi - \arcsin\left(\frac{l_{i1}}{l_{i7}}\sin(\pi/4 + \tau_{i1} + \tau_{i2})\right) - \pi/4 - \tau_{i2},$$
$$\nu_{i1} = \tau_{12} + \arcsin\left(\frac{l_{i4}}{l_{i9}}\cos(2\tau_2)\right),$$
$$\nu_{i2} = -\arcsin\left(\frac{l_{i1}}{l_{i7}}\sin(\pi/4 + \tau_{i1} + \tau_{i2})\right) + \tau_{i2}.$$

The members with lengths l_{ik}, $k = \overline{1,6}$ have cross section area Λ_{i1} and are made from material with Young's modulus E_{i1}, while the members with lengths l_{im}, $m = \overline{7,9}$ have cross section area Λ_{i2} and Young's modulus E_{i2}. Using the principle of virtual work, we can write

$$-N\delta_i + \frac{1}{\Lambda_{i1}E_{i1}}\sum_{j=1}^{6} F_{ij}^2 l_{ij} + \frac{1}{\Lambda_2 E_2}\sum_{m=7}^{9} F_{im}^2 l_{im} = 0, \tag{4.3}$$

where δ_i is the deflection of the cell with number i at the point of the force N application. From (4.3), we can present in nondimensional form

$$\overline{\delta}_1 = \overline{P}S_1 \qquad \overline{\delta}_2 = -2\overline{P}S_2, \tag{4.4}$$

where $\overline{\delta}_i = \delta_i/L_1$, $\overline{P} = P\,L_1^2/(EI)$, E and I are Young's modulus and the second moment of area of the substrates, respectively, and

$$S_1 = Q_{11}\sum_{j=1}^{6}\bar{l}_{1j}G_{1j}^2 + Q_{12}\sum_{m=7}^{9}\bar{l}_{1m}G_{1m}^2,$$
$$S_2 = Q_{21}\sum_{j=1}^{6}\bar{l}_{2j}G_{2j}^2 + Q_{22}\sum_{m=7}^{9}\bar{l}_{2m}G_{2m}^2. \tag{4.5}$$

Here, $\bar{l}_{ij} = l_{ij}/L_1$, $i = 1, 2$, $j = \overline{1,9}$ and

$$Q_{11} = \frac{EI}{\Lambda_{11}^2 L_1^2 E_{11}}, \quad Q_{12} = \frac{EI}{\Lambda_{12}^2 L_1^2 E_{12}},$$
$$Q_{21} = \frac{EI}{\Lambda_{21}^2 L_1^2 E_{21}}, \quad Q_{22} = \frac{EI}{\Lambda_{22}^2 L_1^2 E_{22}}.$$

Now, suppose that the moving substrate can be modeled as an Euler-Bernoulli beam free of load but with nonzero deflections at the cell vertices where the beam is supported and a free right end. The beam behavior can be described by the equation Gere and

Timoshenko (1997)

$$EIw^{IV} = 0, \tag{4.6}$$

where w is the beam center-line deflection. Introduce dimensionless quantities: $\bar{x} = c/L_1$, $\bar{w} = w/L_1$. The total nondimensional deflection of the cell vertices will be the sum of the deflection due to applied force and thermal deflection due to change of temperature, i.e.,

$$\bar{w}_{i*} = \bar{\delta}_i + H_i/L_1\alpha_{Hi}\mathrm{d}T, \qquad i = 1, 2 \tag{4.7}$$

We can present a general solution of the equation (4.6) in nondimensional form as

$$\begin{aligned} \bar{w}_1 &= c_0 + c_1\bar{x} + c_2\bar{x}^2 + c_3\bar{x}^3, \qquad \bar{x} \in [0, 1], \\ \bar{w}_2 &= c_4 + c_5\bar{x} + c_6\bar{x}^2 + c_7\bar{x}^3, \qquad \bar{x} \in [1, 2] \end{aligned} \tag{4.8}$$

with boundary conditions:

$$\begin{aligned} \bar{w}_1(0) = \bar{w}_{1*}, \qquad & \bar{w}_1^{''}(0) = 0, \\ \bar{w}_2^{''}(2) = 0, \qquad & \bar{w}_2^{'''}(2) = \bar{P}, \\ \bar{w}_1(1) = \bar{w}_2(1) = \bar{w}_{2*}, & \\ \bar{w}_1^{'}(1) = \bar{w}_2^{'}(1), \qquad & \bar{w}_1^{''}(1) = \bar{w}_2^{''}(1). \end{aligned} \tag{4.9}$$

Substituting (4.8) into (4.9) and solving, we can find c_4, c_5, c_6, c_7 and $\bar{w}_2(2)$:

$$\bar{w}_2(2) = 2\bar{w}_{2*} - \bar{w}_{1*} - 2/3\bar{P}.$$

Finally, accounting for (4.4) and (4.7), we obtain

$$\bar{P} = \frac{2\alpha_{H2} - \alpha_{H1}}{2 + 12S_2 + 3S_1}\frac{3H}{L_1}\mathrm{d}T.$$

Using formulae (4.2),(4.5) and the values of α_{H1}, α_{H2} obtained earlier for the switch, we calculate the blocking force versus the ratio of the second substrate thickness to its length b/L (fig. 4.11) provided that the second substrate has a square cross section, $L = 2L_1$ and $\Delta T = 100°\mathrm{C}$.

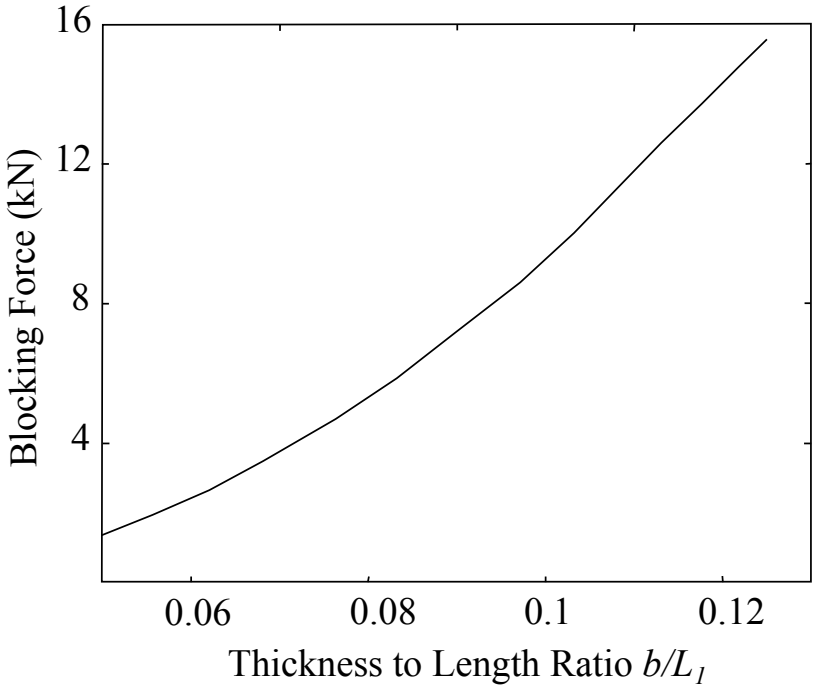

Figure 4.11: Blocking force of a stainless switch thermally driven by a titanium-magnesium alloy lattice.

4.2.2 Tweezers

Thermal tweezers use changes in temperature to induce relative rotation in a mechanical system, leading to the ability to grip objects between two parts of the system. Here, we design a two-cell lattice that can be used as a mechanism for the thermal actuation of tweezers . Our interest is in tweezer kinematics. The gripping force depends on the tweezer materials and the cross sectional area of tweezers members. Because tweezers are determined by a designer to achieve specific functional goals in a particular application, we do not consider gripping force here.

In this subsection, to design thermal tweezers, we will use the same base triangles, lattice materials, and skew angles as we used for the thermal switch considered previously. The actuation mechanism consists of two cells with different heights: $H_1 = 2$ cm in the left cell and $H_2 = 1.5$ cm in the right cell (fig. 4.12). The left cell is of type II, and the right cell type I. When temperature $\Delta T = 100°$C is applied, using the rounded results obtained for the switch, the left cell extends along the height with $\Delta H_1 = 2 \cdot 119$ μm $= 238$ μm, and the right cell shrinks with $\Delta H_2 = -1.5 \cdot 82$ μm$= -123$ μm (fig. 4.13) causing a rotation of the second substrate and lowering its right end. The grey circles and the dashed line depict hinges and a new position of tweezers tips, respectively.

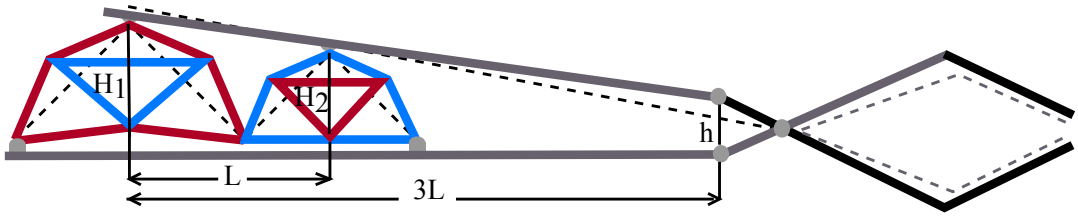

Figure 4.12: Two-cell titanium-magnesium alloy lattice as a part of tweezer.

Denote the distance between the heights of the cells as L. If the distance from H_1 to the two hinges on substrates is $3L$, the distance between the two hinges is $h = AB = 3H_2 - 2H_1 = 5$ mm (fig. 4.14) . It can be shown that when temperature increases, the distance between the two hinges is $h_n = A_1B_1 = 3H_2 + 3\Delta H_2 - 2H_1 - 2\Delta H_1 = 0.5 - 0.85$ mm. Then, $\sin \angle EO_1C_1 = 0.5 \cdot h_n/A_1O_1 = 0.42$ or $\angle EO_1C_1 = 24.5°$. The tweezers are designed with equilateral triangle ABO. At heating it distorts, the hinges at the points A, B and O move to the new positions A_1, B_1 and O_1 so that $A_1O_1 = B_1O_1 = AO(1 + \alpha_{st.st}\Delta T)$ where $\alpha_{st.st.} = 17.3$ ppm/°C is the CTE of the stainless steel substrates. If $OC = 5AO$, $CD = 3.5AO$, and $\angle OCD = 120°$ remains independent of temperature, then $O_1D_{1=}\sqrt{54.75}h_n$, $\sin \angle D_1O_1C_1 = 1.75\sqrt{3/54.75}$, and $\angle D_1O_1C_1 = 24.2°$. The original distance from the point D to the line OE was 3.75 mm. When temperature increases, the point D moves to the position D_1, and the distance from D_1 to the line OE is $D_1E = \sqrt{54.75}h_n \sin(24.5 - 24.2) = 0.174$ mm, i.e. each tweezer tip moves 3.57 mm toward the closed position.

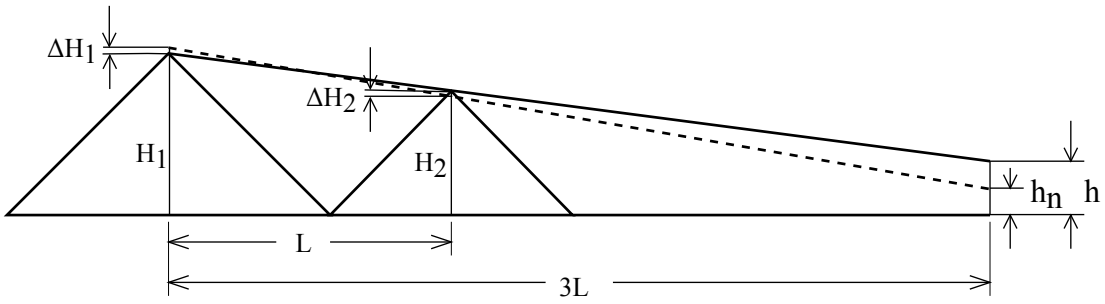

Figure 4.13: Kinematics of tweezer handles. When temperature is applied, the left cell extends along H_1, and the right cell shrinks along H_2.

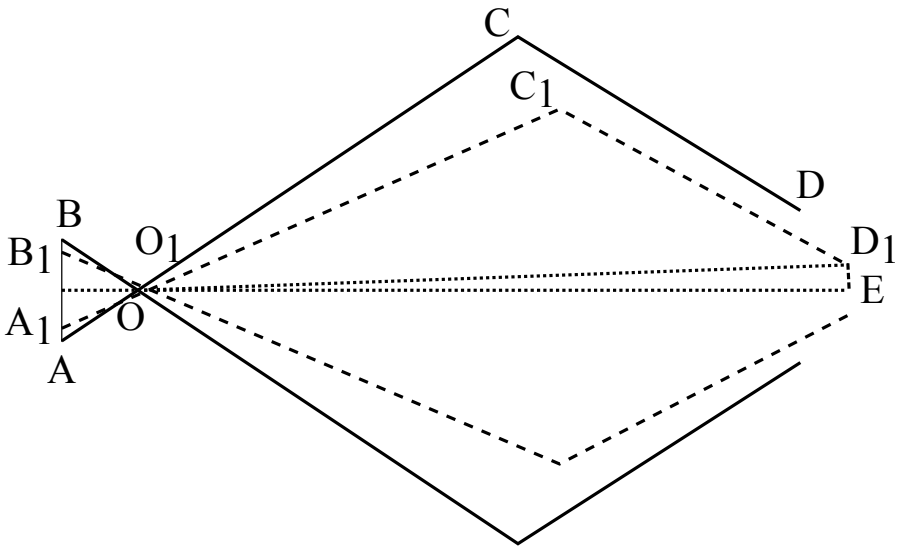

Figure 4.14: Kinematics of tweezer jaws. The polygonal line $O_1C_1D_1$ shows a new position of the upper jaw when temperature is applied.

4.2.3 Thermal valve

A thermal valve consists of three-cell lattice connected on its bottom and top surfaces to two substrates parallel to each other. When temperature changes, the height of the left and the right cells increases, while the height of the cell in the middle decreases. This leads to the deflection of the upper substrate, which schematically resembles a valve (fig. 4.15). Here, we are interested in the design of such a structure and do not consider bending deformation in the upper substrate. The three-cell lattice consists of two type II cells on its left and right edges and one type I cell between them as shown in fig. 4.15. The left and right cells of the lattice have the same configuration. The lattice is joined to the first substrate only at its left and right ends. A plug controlling a valve is connected at point A. To be connected to the substrates without thermal expansion mismatch stresses, the following relation must be fulfilled in a three-cell lattice

$$\begin{gathered} \alpha_{11} + \alpha_{21} + \alpha_{31} = 3A_1 = 3A_2, \\ \alpha_{12} = \alpha_{13}, \quad \alpha_{22} = \alpha_{23}, \quad \alpha_{32} = \alpha_{33} \end{gathered} \tag{4.10}$$

As an example, we consider a titanium-magnesium alloy lattice. For its left and right cells (Type II), choose $t_1 = 3.8°$, $t_2 = t_3 = 35°$, that correspond to normalized CTEs $\alpha_{11}/\alpha_1 = 1.035$, $\alpha_{12}/\alpha_1 = \alpha_{13}/\alpha_1 = 2.6326$ or $\alpha_{11} = 29$ ppm/°C, $\alpha_{12} = \alpha_{13} = 73.7$ ppm/°C. For the cell in the middle, let $t_1 = 0°$, $t_2 = t_3 = 35°$, that correspond to

$\alpha_{21}/\alpha_1 = 1$, $\alpha_{22}/\alpha_1 = \alpha_{23}/\alpha_1 = -4.2688$ or $\alpha_{21} = 8.6$ ppm/°C, $\alpha_{22} = \alpha_{23} = -36.7$ ppm/°C. Using the last two formulae (4.1), we have $\alpha_{H1} = 118.45$ ppm/°C and $\alpha_{H2} = -82.0$ ppm/°C. From the first formula (4.10), it is seen that these skew angles provide a substrate CTE $A_1 = A_2 = (29 + 8.6 + 29)/3 = 22.2$ ppm/°C, which correspond to the CTE of aluminum. Hence, the valve can be connected to aluminum substrates without thermal expansion mismatch. As in the previous example, other skew angles θ_1 and θ_2 in all three cells would let us connect the valve without thermal expansion mismatch stresses to a substrate with a different CTE. When temperature changes, the difference between the position of the middle point of the second substrate and its left or right ends is $\Delta H = |\Delta H_1| + |\Delta H_2| = \Delta T H(\alpha_{H1} - \alpha_{H2}) = 2 \cdot 10^{-4} \Delta T H$ m (fig. 4.15). If $\Delta T = 100$°C, $\Delta H/H100\% = 2\%$. When the temperature changes, the position of the second substrate is depicted with dash-line contour.

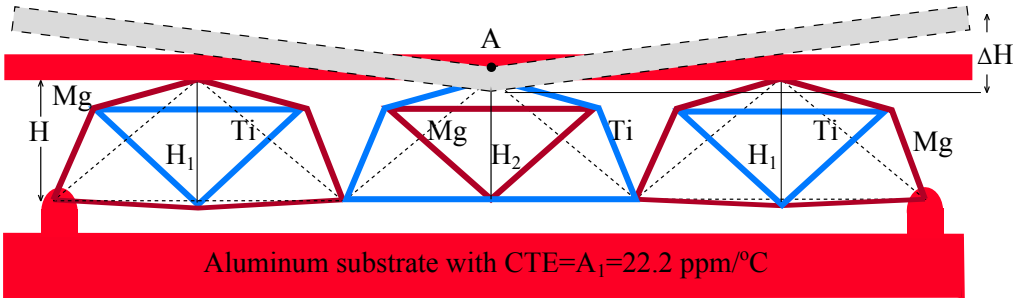

Figure 4.15: A three-cell lattice working as a thermal valve designed using based isosceles triangles with right angles.

4.3 Concluding remarks

The approach demonstrated in this chapter shows that a combination of cells that extend and cells that shrink when temperature is applied can amplify desirable deflections in substrates. Moreover, extension and shrinking can be designed in different directions, and this can be used for more complicated shape control of structures. For proper evaluation of actuator performance we need to compare it with the performance of actuators having identical or similar configuration and dimensions. This is very difficult to do because a typical piezoelectric actuator is a cylindrical stack or a wire while the actuators comprising bimaterial lattices have a unique configuration. The comparison of attainable strain is insufficient because we have to account also for the deformation per actuator mass or per applied force. However, we can broadly position the strain attainable by the

actuators designed here and equal to 3.2% for the thermal switch and of 2% for the valve between piezoceramic (0.2 %) and NiTi SMA (10 %) actuators made of pure materials and reported in Jani et al. (2014).

Chapter 5

Experimental results

The goal of this chapter is to validate the results presented in Chapter 2 and Chapter 3 that were obtained analytically using equations (2.7) and (3.1). To reach this goal, two bimaterial cells of different geometry and combination of materials were heated and their CTEs were measured.

5.1 Experimental configuration

In this chapter, the methodology for measuring CTEs in isotropic bimaterial lattices (Steeves et al., 2009) is applied to anisotropic bimaterial cells. The experiment is performed on a hotplate with 30 cm x 60 cm heating surface (fig. 5.1). The hotplate was placed on a resin rug to damp external vibrations; its surface was carefully leveled to be horizontal. An additional polished copper plate with 15 cm x 14 cm side lengths was put on the middle part of the heating surface to create a homogeneous temperature field. The position of the plate was chosen to be equidistant from the hotplate heating elements. The copper plate was painted black to have better contrast for the camera images. A high resolution camera with a TAMRON SP macro lens leveled normal to the hotplate surface was mounted over the copper plate. The exposed part of the hotplate was covered with 25 mm thick insulating material to prevent image distortion due to convection currents. The area over the copper plate was covered with a heat resistant glass plate. A dial indicator was mounted on the boundary of the glass and the insulation to touch the copper plate and measure the normal thermal expansion of the hotplate. The effect of this displacement was removed from the calculation of CTEs. The boundaries of the glass plate were additionally covered with a second layer of thermal insulation. A fan was set near the hotplate to provide air currents; this helped to avoid heat shimmer and minimize camera image distortion. To damp vibrations from the fan, it was mounted on

a foam rubber pad (fig. 5.1).

To obtain high quality images, the camera aperture was set at its maximum, and the exposure time was minimized. The camera was connected to a computer with Vic-2D Correlated Solutions System (2009). Two cells with different skew angles and different combinations of materials were tested separately. The cell CTEs were measured by comparing images taken at room temperature and images taken at elevated temperature. The distances between the pin heads in the cell vertices coinciding with the vertices of the base triangle were compared. To increase the accuracy of the images, the camera was positioned as close as possible to the cell on the hotplate, so only two pins corresponding to the base triangle vertices were in focus. The cell pin heads were covered with high-temperature white paint and cured in an electric oven at 70°C for 5-6 hours. This resulted in sharp contours of black speckles added to the white background. Every test day, the speckle patterns were renewed because after few hours of heating, the white paint became yellowish, and the quality of the images deteriorated because of reduced contrast. The pin stems and the lower surface of pin heads were cleaned of paint. Restriction in the relative rotation of the lattice members would bias the results. For lower friction at rotation of pins in the holes of cell members, the pin stems, the holes, and the part of member horizontal surfaces where the pin heads touched the cell members were covered with liquid silicone. The internal triangle of the cells was painted in black for better contrast. The lighting of pins heads was extremely important since the two pins between which the displacements were measured must be lighted uniformly, and the shadows from the insulating plates must be eliminated.

Two thermocouple wires were attached to the copper plate surface; their other ends were connected to the computer measuring temperature and to the hotplate controller, respectively. Two other thermocouple wires were connected to cell members for additional control of temperature, but later they were removed to reduce interference with the cell expansion. The two remaining wires were positioned in a way not to interfere with the thermal insulation.

5.2 Materials and fabrication

The members of two bimaterial cells were manufactured and assembled. The first cell was made based on an equilateral triangle with side lengths of 45 mm. The thickness of the hexagon members was 6 mm and the width was 8 mm. The internal triangle material was an aluminum alloy AA 2124-T851 with CTE=22.9 ppm/°C. The external hexagon member material was a titanium alloy Ti-6Al-4V (Grade 5) with CTE=8.6 ppm/°C. The

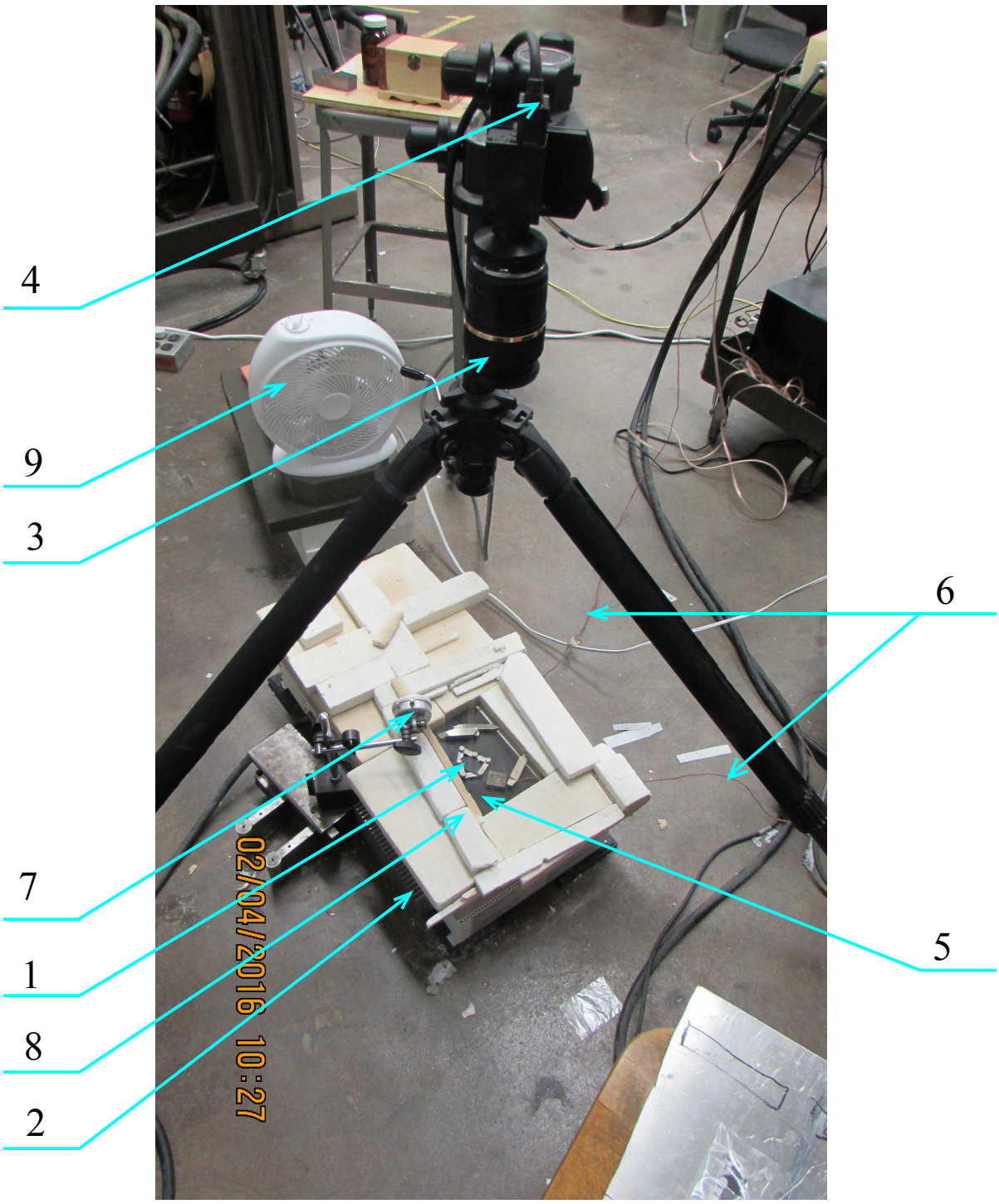

Figure 5.1: Experimental setup: 1 - bimaterial cell; 2 - hotplate; 3 - camera lens; 4 - camera; 5 - copper plate; 6 - thermocouple wires; 7 - dial indicator; 8 - insulation; 9 - fan.

skew angles were $\theta_1 = \theta_2 = t_1 = 0°$, $\theta_3 = \theta_4 = t_2 = 12.92°$, and $\theta_5 = \theta_6 = t_3 = 27.11°$ (fig. 5.2).

The second cell was made based on an isosceles right-angle triangle with base side lengths 45 mm. The thickness of hexagon members was 6 mm and the width was 7 mm. The internal triangle material was titanium alloy with CTE=8.6 ppm/°C while the external hexagon member material was aluminum alloy with CTE=22.9 ppm/°C. The skew angles were $\theta_1 = \theta_2 = t_1 = -5.6°$, $\theta_3 = \theta_4 = t_2 = \theta_5 = \theta_6 = 20.0°$ (fig. 5.3).

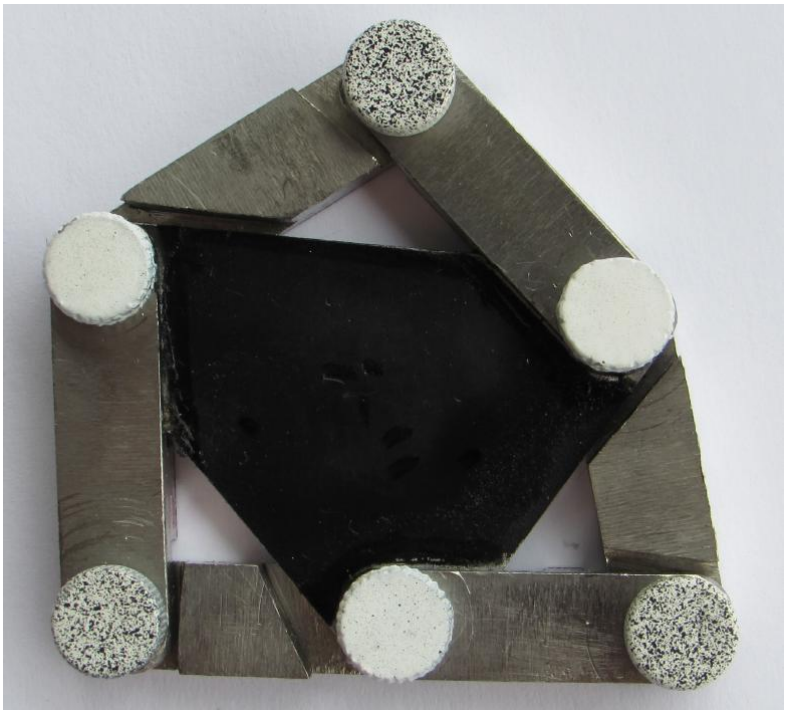

Figure 5.2: An aluminum-titanium cell based on an equilateral triangle used in the experiment.

The pins were made of a titanium alloy with CTE=8.6 ppm/°C. The diameter of the pin heads was 7 mm and the diameter of the pin stems was 2.5 mm to fit the diameter of the holes in the members for pin connections. The pins were tightly inserted in the holes but had freedom to rotate.

5.3 Experimental measurements

Before starting the experiments, a preliminary test of two material samples made of titanium alloy (8.6 ppm/°C) and aluminum alloy (22.9 ppm/°C) was performed. The samples had a shape copied from the hexagon cell members with 53 mm length and 8

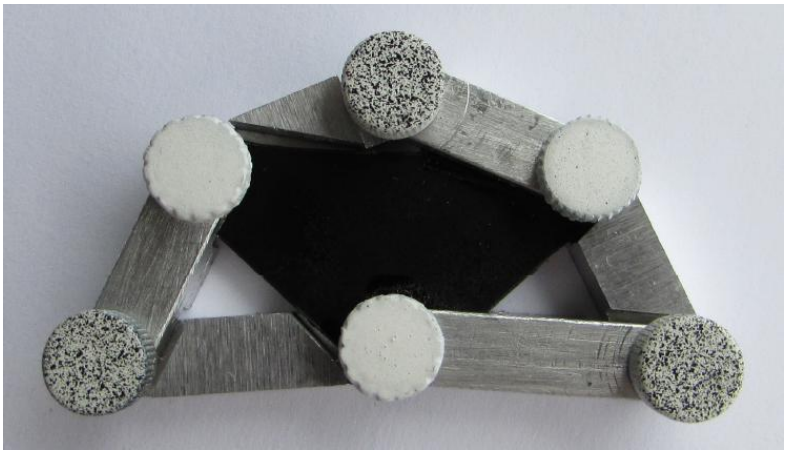

Figure 5.3: An aluminum-titanium cell based on an isosceles right-angle triangle used in the experiment.

mm in width and thickness. They were heated to 78°C, 96°C, and 110°C. The room temperature varied from 22°C to 23°C. Their CTEs were calculated, and it was found that the difference between experimentally found and known CTEs of their materials did not exceed 4.7%. Subsequently, the experiment with cells was initiated. On every experimental day, only one cell CTE was measured. Because the hotplate controller was not able to provide an exact temperature, the temperature was chosen approximately but measured exactly. To heat the cells, the temperature was kept constant for at least 10 minutes. Five images were taken at each temperature. The value of the CTE was calculated as the mean of the five CTEs calculated from the data of these five images. First, a cell based on an equilateral triangle was heated, and its CTEs were measured (fig. 5.4). The standard deviation σ_i of each CTE $\overline{\alpha}_i$, $i = 1, 2, 3$ among five images made at the same temperature did not exceed 0.3 ppm/°C.

Second, a cell based on a isosceles right angle triangle was heated, and its CTEs were measured (fig. 5.5). In this case the standard deviation σ_i of each CTE $\overline{\alpha}_i$, $i = 1, 2, 3$ among five images made at the same temperature did not exceed 0.7 ppm/°C.

As it is seen from fig. 5.4 and fig. 5.5, the experimental data are in good agreement with theoretical predictions. Experimental values of the cell CTEs obtained for the cell based on an equilateral triangle are higher than analytically predicted values because this cell tends to shrink when temperature rises, and friction between hexagon members and the copper plate and between pins and cell members partially inhibit this shrinkage. In fig. 5.5, the experimental data obtained for the sides with 20° skew angles lie below the analytically predicted values because this cell tends to extend along the lateral sides of the base triangle, and the friction partially inhibits this. Along the side with the skew

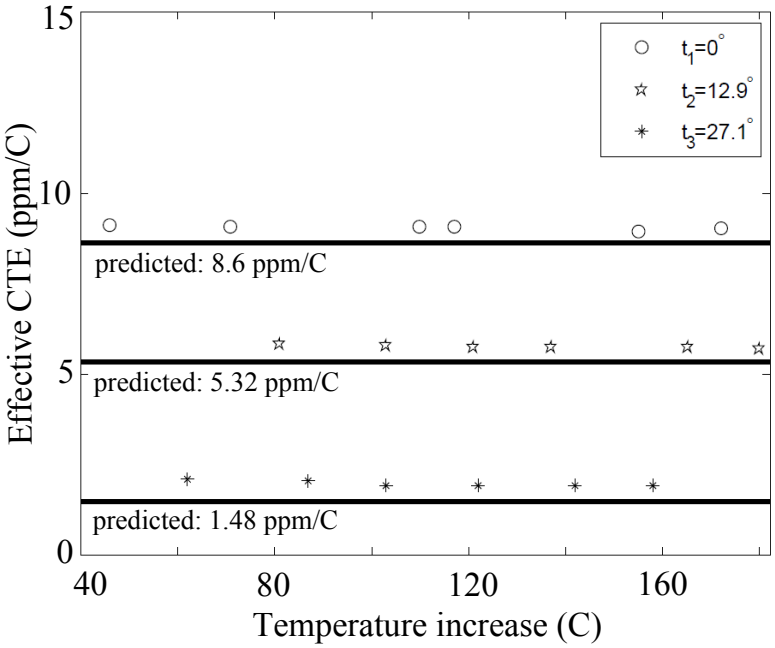

Figure 5.4: Correspondence of the experimental data to theoretical results in a cell based on an equilateral triangle.

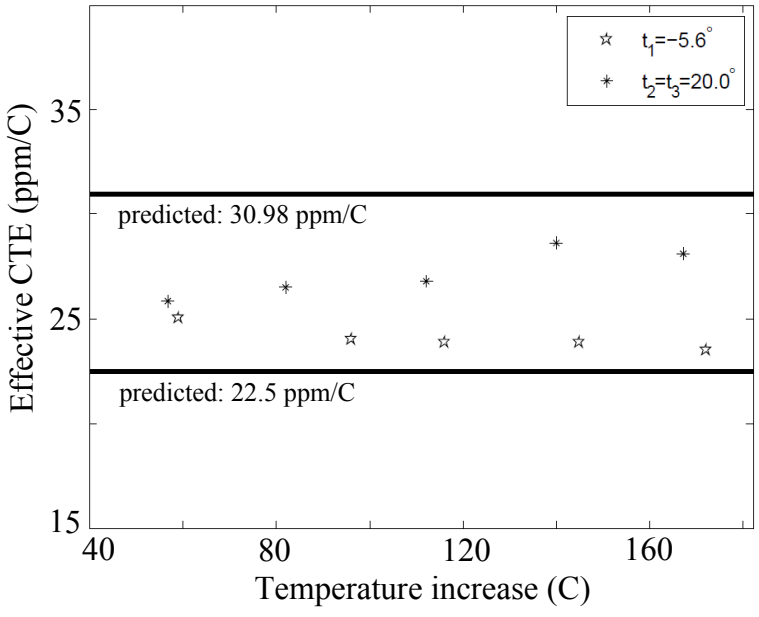

Figure 5.5: Correspondence of the experimental data to theoretical results in a cell based on an isosceles right-angle triangle.

angle $-5.6°$, the opposite is true. At higher temperature, for both cells, as was earlier observed by Steeves et al. (2009), the experimental results are closer to the analytically predicted values because the imperfections at the pin joints become less important. Also, for the cells with higher anisotropy the experiment is more challenging because a cell CTE depends nonlinearly on all external interventions such as external vibrations, non-uniform light, etc. and on internal imperfections; with greater anisotropy the nonlinearity increases. That is why the experimental data in fig. 5.5 differ from analytically predicted values more than in fig. 5.4. In general, the experimental results confirmed the analytical results.

Chapter 6

Stiffness analysis

In the previous chapter, the analytical results obtained earlier were confirmed experimentally. Additionally, they can be confirmed numerically using, for example, finite element method (Ross, 1991). First, we will model a bimaterial cell as a pin-jointed truss and calculate its CTEs numerically using discrete rod elements for the pin-jointed trusses. As was shown in the Chapter 5, imperfections in pin joints distort the values of cell CTEs. Bimaterial cells and lattices with rigid joints can be fabricated more accurately with cutting by electric discharge machining and subsequent press fit (Berger et al., 2011; Steeves et al., 2009), spot laser welding (Gdoutos et al., 2013) or printing on a multimaterial 3-D printer. Such cells would not be pin-connected but, rather, would be rigidly connected. Hence, a model for such cells is needed and will be developed in this chapter. Using the same approach as for pin-jointed cells, we will simulate a bimaterial cell as a frame with rigid joints and find its CTEs accounting for member bending stiffness.

6.1 Stiffness analysis of bimaterial lattices

Consider an arbitrary cell as an assembly of nine members - elements with six nodes (fig. 6.1). In this figure, element numbers are indicated by a circle and node coordinates (x_i, y_i), $i = \overline{1,6}$ are in parentheses.

In this chapter we consider cells with equal skew angles adjacent to the same side of a base triangle: $\theta_1 = \theta_2 = t_1$, $\theta_3 = \theta_4 = t_2$, $\theta_5 = \theta_6 = t_3$. The nodal coordinates in the

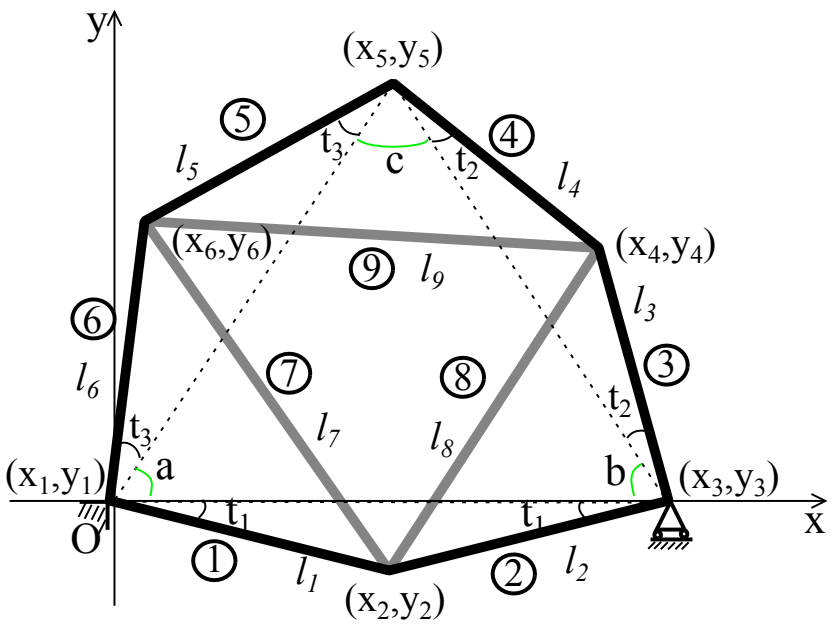

Figure 6.1: Bimaterial cell with members -discrete elements

coordinate system depicted in fig. 6.1 are

$$\begin{aligned} x_1 &= -0.5L_1, \quad y_1 = 0, \\ x_2 &= 0, \quad y_2 = -0.5L_1 \tan t_1, \\ x_3 &= 0.5L_1, \quad y_3 = 0, \\ x_4 &= 0.5L_1 - l_3 \cos(b + t_2), \quad y_4 = l_3 \sin(b + t_2), \\ x_5 &= 0, \quad y_5 = 0.5L_1 \tan b, \\ x_6 &= -0.5L_1 - l_6 \cos(a + t_3), \quad y_6 = l_6 \sin(a + t_3). \end{aligned}$$

An element stiffness matrix is denoted as k_i and force vector as f_i where i is a number of the element. Their expressions will be presented later. Assembly produces a global stiffness matrix K_g and a global force vector F_g that are linked to each other through the displacement vector U_g with components u_1, v_1, u_2, $v_2, \ldots,$ u_6, v_6

$$K_g U_g = F_g. \tag{6.1}$$

To exclude rigid body motion, set the boundary conditions as

$$u_1 = v_1 = v_3 = 0. \tag{6.2}$$

After introduction of the boundary conditions (6.2) into the matrix equation (6.1), the displacement vector U can be found as its solution $U_g = K_g^{-1} F_g$ where K_g^{-1} is the matrix inverse to K_g. The new coordinates of the cell nodes due to thermal expansion can be calculated as $x_{1n} = x_1 + u_1$, $y_{1n} = y_1 + v_1$, and so on.

Suppose all cell members have a square cross section with side length w, area $\Lambda = w^2$, and second moment of area $I = \Lambda^2/12$. First, we are going to employ a rod element for trusses with pin joints and compare numerical results with the analytical results obtained in the previous sections. Then we will use a beam element for plane frames with rigid joints (Ross, 1991) and compare the results obtained with the rod analysis.

6.2 Rod elements

In the global coordinate system (fig. 6.1), a rod discrete element (with two nodes at the ends of the rod with number i and j) has two displacement degrees of freedom in the x and y directions at each node $\{u_i, v_i, u_j, v_j\}$. The element stiffness matrix in global coordinates is (Ross, 1991)

$$k_i = \frac{\Lambda E_i}{l_i} \begin{bmatrix} c^2 & cs & -c^2 & -cs \\ cs & s^2 & -cs & -s^2 \\ -c^2 & -cs & c^2 & cs \\ -cs & -s^2 & cs & s^2 \end{bmatrix}$$

where $c = (x_j - x_k)/l_i$, $s = (y_j - y_k)/l_i$, l_i is the length of member i, E_i is Young's modulus of the material of member i. The thermal expansion of the member can be included by modifying the element force vector as

$$f_i = E_i \alpha_i T \Lambda \begin{bmatrix} -c \\ -s \\ c \\ s \end{bmatrix}$$

where α_i is the element CTE and T is temperature increase.

Stiffness analysis with rod elements was used to obtain solutions to the problems considered in Chapters 2-4. The analytical equations derived earlier and the stiffness technique described here have completely coincident results.

The problems also can be solved using an analytical geometry approach. Introduce a Cartesian coordinate system with the origin of coordinate coinciding with the vertex F

(fig. 6.2) where the cell is fixed and the x-axis passes along the line FD. The y-axis is

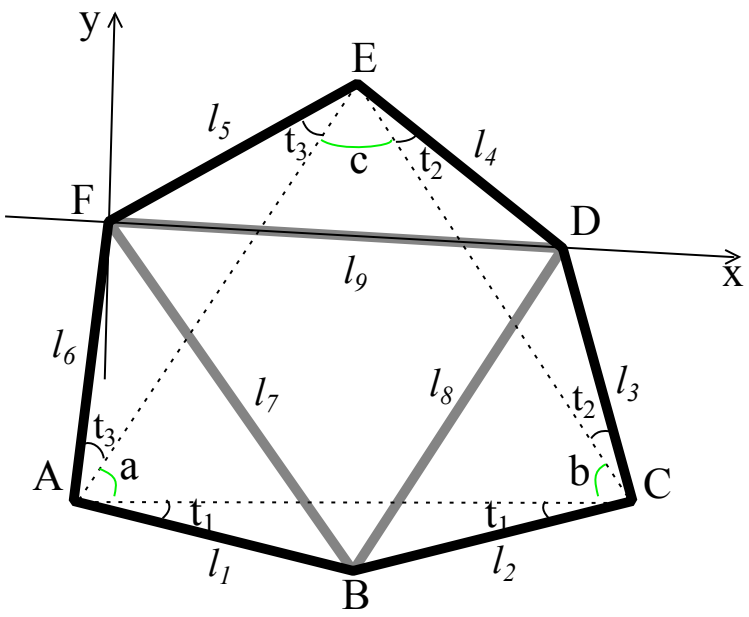

Figure 6.2: Sketch of a lattice cell in Cartesian coordinate system.

directed upward perpendicular to the x-axis through the point F. We need to express the coordinates of three cell vertices A, C, and E as functions of nine cell member lengths l_i, $i = \overline{1,9}$ before and after heating. As it was indicated in Chapter 2, $l_i = L_1/2\cos t_1$, $i = 1,2$, $l_i = L_2/2\cos t_2$, $i = 3,4$, $l_i = L_3/2\cos t_3$, $i = 5,6$, $l_7 = \sqrt{l_1^2 + l_6^2 - 2l_1 l_6 \cos A'}$, $l_8 = \sqrt{l_2^2 + l_3^2 - 2l_2 l_3 \cos B'}$, $l_9 = \sqrt{l_4^2 + l_5^2 - 2l_4 l_5 \cos C'}$, $A' = t_1 + t_3 + a$, $B' = t_1 + t_2 + b$, $C' = t_2 + t_3 + c$. When the temperature has an increment ΔT, the lengths become $l_{in} = l_i(1 + \alpha_j \Delta T)$ where $\alpha_j = \alpha_1$ for $i = \overline{1,6}$ and $\alpha_j = \alpha_2$ for $i = \overline{7,9}$. Let vertices A, B, C, D, E, F have numbers 1, 2, 3, 4, 5, 6, correspondingly. The vertex coordinates before heating can be presented as $x_i = f_i(l_1, l_2, l_3, l_4, l_5, l_6, l_7, l_8, l_9)$

and $y_i = g_i(l_1, l_2, l_3, l_4, l_5, l_6, l_7, l_8, l_9)$ where

$$\begin{aligned}
f_1(l_1,\ldots,l_9) &= \frac{-c_1c_2 - \sqrt{l_6^2(1+c_2^2) - c_1^2}}{1+c_2^2},\\
g_1(l_1,\ldots,l_9) &= c_1 + c_2\frac{-c_1c_2 - \sqrt{l_6^2(1+c_2^2) - c_1^2}}{1+c_2^2},\\
f_2(l_1,\ldots,l_9) &= \frac{l_7^2 + l_9^2 - l_8^2}{2l_9},\\
g_2(l_1,\ldots,l_9) &= -\sqrt{l_7^2 - \left(\frac{l_7^2 + l_9^2 - l_8^2}{2l_9}\right)^2},\\
f_3(l_1,\ldots,l_9) &= \frac{l_9 - c_3c_4 + \sqrt{l_3^2(1+c_4^2) - c_3^2 - c_4^2l_9^2 - 2l_9c_3c_4}}{1+c_4^2},\\
g_3(l_1,\ldots,l_9) &= c_3 + c_4\frac{l_9 - c_3c_4 + \sqrt{l_3^2(1+c_4^2) - c_3^2 - c_3^2l_9^2 - 2l_9c_3c_4}}{1+c_4^2}\\
f_4(l_1,\ldots,l_9) &= l_9,\\
g_4(l_1,\ldots,l_9) &= 0,\\
f_5(l_1,\ldots,l_9) &= \frac{l_5^2 + l_9^2 - l_3^2}{2l_9},\\
g_5(l_1,\ldots,l_9) &= \sqrt{l_5^2 - \left(\frac{l_5^2 + l_9^2 - l_3^2}{2l_9}\right)^2}
\end{aligned} \tag{6.3}$$

and

$$c_1 = \frac{l_6^2 + l_7^2 - l_1^2}{2y_2},\ c_2 = -\frac{x_2}{y_2},\ c_3 = \frac{l_3^2 + l_7^2 - l_2^2 - l_9^2}{2(y_2 - y_4)},\ c_4 = -\frac{x_2 - x_4}{y_2 - y_4}.$$

When the temperature changes, the new coordinates of vertices A, C, and E will be

$$x_{in} = f_i(l_{1n}, l_{2n}, \ldots l_{9n}), \quad y_{in} = g_i(l_{1n}, l_{2n}, \ldots l_{9n}), \quad i = 1, 3, 5$$

Now, the three cell CTEs can be found by formulae

$$\begin{aligned}
\overline{\alpha}_1 &= \frac{\sqrt{(x_{1n} - x_{3n})^2 + (y_{1n} - y_{3n})^2} - L_1}{L_1\Delta T},\\
\overline{\alpha}_2 &= \frac{\sqrt{(x_{3n} - x_{5n})^2 + (y_{3n} - y_{5n})^2} - L_2}{L_2\Delta T},\\
\overline{\alpha}_3 &= \frac{\sqrt{(x_{1n} - x_{5n})^2 + (y_{1n} - y_{5n})^2} - L_3}{L_3\Delta T}.
\end{aligned} \tag{6.4}$$

The analytical geometry approach and the stiffness analysis with rod elements lead to

identical results.

6.3 Frame elements with rigid joints

In a global coordinate system (fig. 6.1), a frame element with rigid joints has six degrees of freedom at two nodes that are at the two ends of the element $\{u_j, v_j, \phi_j, u_k, v_k, \phi_k\}$ where j and k are the numbers of the nodes on the cell member, u_j, u_k are displacements in x direction, v_j, v_k are displacements in y direction, ϕ_j and ϕ_k are counterclockwise rotations of the nodes with numbers j and k, respectively. An element stiffness matrix in global coordinates k_i can be presented as a sum of the stiffness matrix of a rod element kr_i and the stiffness matrix of a beam element kb_i (Ross, 1991)

$$k_i = kb_i + kr_i \tag{6.5}$$

where

$$kb_i = EI \begin{bmatrix} \frac{12}{l_i^3}s^2 & & & & & \\ -\frac{12}{l_i^3}cs & \frac{12}{l_i^3}c^2 & & & & \\ \frac{6}{l_i^2}s & -\frac{6}{l_i^2}c & \frac{4}{l_i} & & & \\ -\frac{12}{l_i^3}s^2 & \frac{12}{l_i^3}cs & -\frac{6}{l_i^2}s & \frac{12}{l_i^3}s^2 & & \\ \frac{12}{l_i^3}cs & -\frac{12}{l_i^3}c^2 & \frac{6}{l_i^2}c & -\frac{12}{l_i^3}cs & \frac{12}{l_i^3}c^2 & \\ \frac{6}{l_i^2}s & -\frac{6}{l_i^2}c & \frac{2}{l_i} & -\frac{6}{l_i^2}s & \frac{6}{l_i^2}c & \frac{4}{l_i} \end{bmatrix}$$

and

$$kr_i = \frac{\Lambda E}{l_i} \begin{bmatrix} c^2 & cs & 0 & -c^2 & -cs & 0 \\ cs & s^2 & 0 & -cs & -s^2 & 0 \\ 0 & 0 & 0 & 0 & 0 & 0 \\ -c^2 & -cs & 0 & c^2 & cs & 0 \\ -cs & -s^2 & 0 & cs & s^2 & 0 \\ 0 & 0 & 0 & 0 & 0 & 0 \end{bmatrix}$$

The force vector in a global coordinate system reflects thermal expansion of each

member as

$$f_i = E\alpha_n T\Lambda \begin{bmatrix} -c \\ -s \\ 0 \\ c \\ s \\ 0 \end{bmatrix}$$

In the **Example 1**, Section 3.2, a two-row titanium-magnesium alloy lattice with pin joints connecting titanium and magnesium alloy substrates has been designed. The skew angles of the left cell in the upper row $t_1 = 0°$, $t_2 = 4.9°$, $t_1 = 32°$ provided three normalized cell CTEs as $\overline{\alpha}_1/\alpha_1 = 1$, $\overline{\alpha}_2/\alpha_1 = 0.81$, $\overline{\alpha}_3/\alpha_1 = -0.31$. The CTEs of the cell with the same skew angles but with rigid joints can be found using plane frame elements. The normalized CTEs have been calculated for four values of lattice member thickness $w = 0.01L_1^2$, $w = 0.003L_1^2$, $w = 0.001L_1^2$, and $w = 0.0005L_1^2$ (Table 6.1). It is seen that as member thickness goes to zero, the pin-connected solution is recovered.

Table 6.1: Three normalized CTEs in a cell with rigid joints for varying member thickness w

i	t_i	$w = 0.1L_1$	$w = 0.055L_1$	$w = 0.032L_1$	$w = 0.022L_1^2$	w=0
1	0°	1.0508	1.0169	1.0058	1.0029	1
2	4.9°	0.89415	0.83991	0.82218	0.81749	0.81
3	32°	-0.03228	-0.21854	-0.27993	-0.29594	-0.31

Normalized CTEs in the titanium-magnesium alloy cell based on an equilateral triangle with $t_1 = 0$ and different values of skew angles $t_2 = t_3$, a square cross-section with area $w \times w$ for different slenderness ratios $r = w/L_1$ are presented in fig. 6.3. The analogous plot for the titanium-magnesium alloy cell based on an isosceles right-angle triangle is depicted in fig. 6.4. On both plots, dotted curves correspond to the case $\alpha_2 < \alpha_1$, and solid curves correspond to the case $\alpha_2 > \alpha_1$. The figures show that as the skew angles become large the rigid-joint solutions diverge from the pin-joint solutions, and rigid joints obstruct thermal expansion of cell members, which is more significant for larger values of r and in the cells where $\alpha_2 < \alpha_1$.

Note that the normalized CTE was calculated along the sides with the length $L_2 = L_3$. However, in the equilateral triangle $L_2 = L_3 = L_1$ but in the isosceles right-angle triangle $L_2 = L_3 = L_1/\sqrt{2}$.

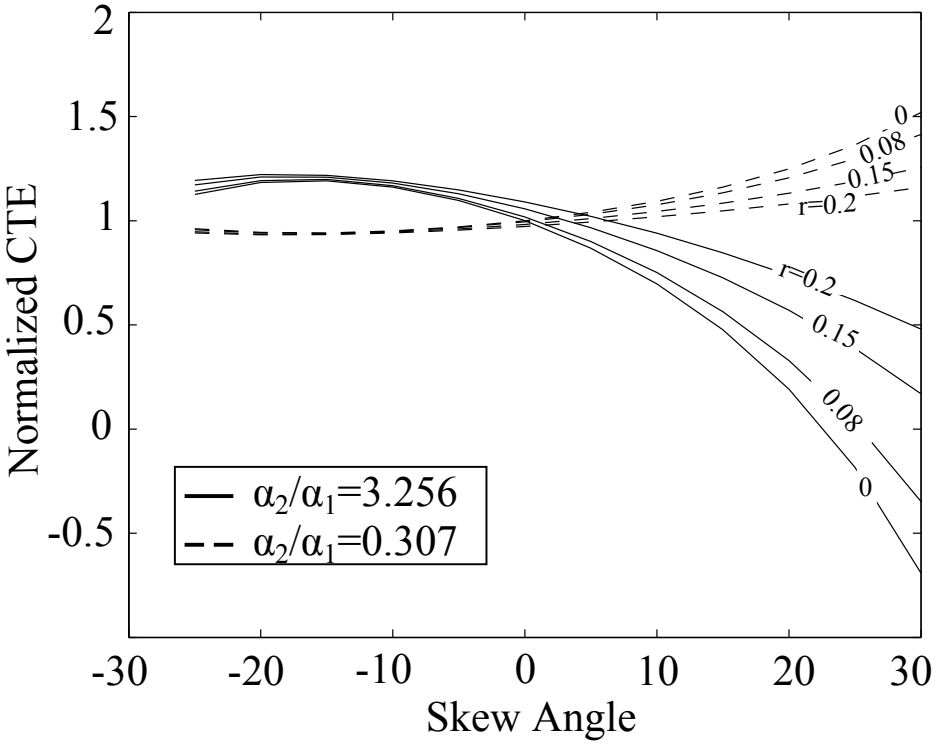

Figure 6.3: Ranges $\overline{\alpha}_2/\alpha_1 = \overline{\alpha}_3/\alpha_1$ of titanium-magnesium alloy cells with rigid joints based on an equilateral triangle with $t_1 = 0°$ for different slenderness ratios $r = w/L_1$; $r = 0$ corresponds to a cell with pin joints. The dotted lines correspond to a cell with a titanium inner triangle and a magnesium alloy outer hexagon, while the solid lines correspond to the magnesium alloy inner triangle and titanium outer hexagon.

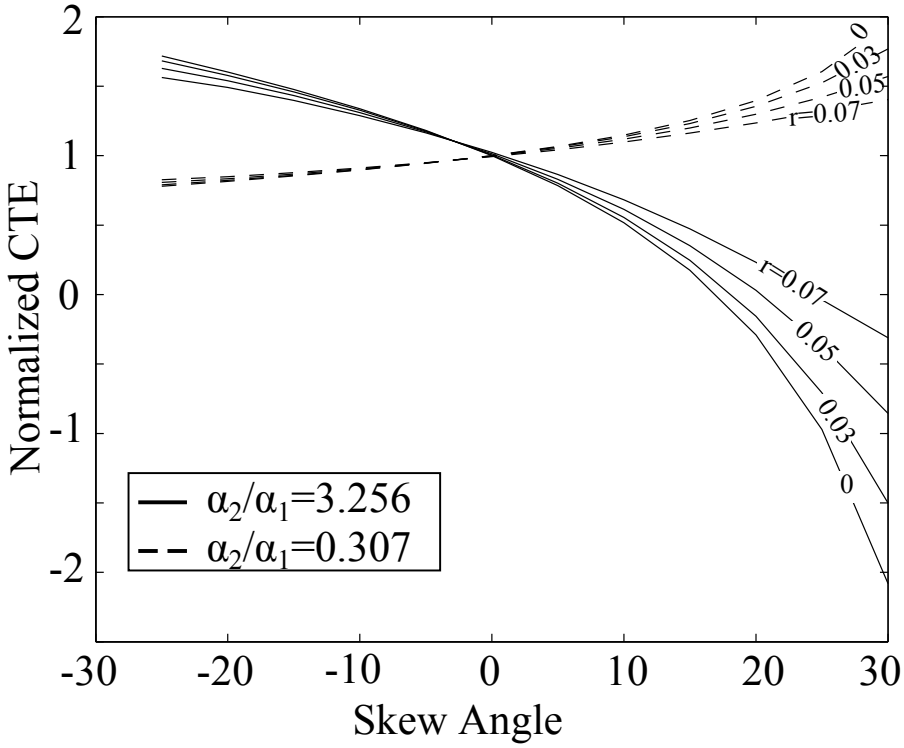

Figure 6.4: Ranges $\overline{\alpha}_2/\alpha_1 = \overline{\alpha}_3/\alpha_1$ of titanium-magnesium alloy cells with rigid joints based on an isosceles right-angle triangle with $t_1 = 0°$ for different slenderness ratios $r = w/L_1$; $r = 0$ corresponds to a cell with pin joints . The dotted lines correspond to a cell with a titanium inner triangle and a magnesium alloy outer hexagon, while the solid lines correspond to the magnesium alloy inner triangle and titanium outer hexagon.

Chapter 7

Conclusions

This work is devoted to bimaterial anisotropic planar lattices. The lattices consist of nonidentical cells, and each cell is composed of internal and external triangles made of materials with different CTEs and pin-connected at three locations. The internal triangle is regular, whereas the external triangle is deformed into a hexagon with varying skew angles. As a consequence of the variation in skew angles in a single cell, the cells have anisotropic CTEs. Combining cells with anisotropic CTEs into a pin-jointed lattice provides the capability to achieve desirable, and differing if necessary, CTEs on the bottom and top edges of the lattice.

The lattice structures designed in this thesis can be used in several applications. First, they can serve as transition elements between two parts of a structure with different CTEs. As a result, the whole structure will be free of thermal mismatch stresses. The design strategy elaborated herein provides a systematic process for choosing the geometric configuration of a single-row lattice that connects substrates of known materials. In particular, guidance on the choice of the materials that would be appropriate to connect the substrates is given, based upon the CTEs of the substrate materials. The design process for single rows of lattice can be extended to multiple rows if that provides a preferable aspect ratio for the adapter. A key limitation to this lattice system is that there are stringent limits on the maximum number of cells that can be used. As the difference between the substrate CTEs increases, the maximum number of lattice cells is reduced because the total deflections that must be accommodated increase with lattice length. An option for mitigating this limitation is to choose lattice materials with larger ratio of their CTEs or use multi-row lattices, and permit rotation of the lattice cells. Two-row lattices enable the connection of substrates with greater CTE mismatch compared to one-row lattices; allowing rotation of the lattice cells extends the concept further. Such topics are the subject of ongoing research. In addition, other configurations, such as a

right-angled cantilever joint and a cylindrical geometry, are also amenable to the same design approach.

Moreover, these lattices are relatively stiff; the isotropic variants are nearly optimally stiff for a structure of this nature Steeves et al. (2007). Alternative options for adapters for thermal mismatch mitigation either induce thermal stresses and curvatures, or are very compliant. Because for anisotropic lattices there are more design variables than design requirements, it is possible to select combinations of lattice skew angles that also achieve additional goals; structural efficiency is an obvious choice. It was shown that the more "stout" a cell is, the higher is its structural efficiency.

Hence it can be seen that these lattices may serve as elements that mitigate thermal mismatch stresses, but they can be considered in a broader sense as well. The lattices have been used here as systems to accommodate geometric changes, but they can also be used to impose geometric changes: these lattices are effectively thermally-activated actuators. This opens additional possibilities for the analysis and use of these lattice systems.

It is possible to impose kinematic conditions on the lattice vertices to enable the solution of three related problems: (i) connecting two materials with differing CTEs without inducing thermal mismatch stresses; (ii) imposing precise known displacements in a system through temperature changes; and (iii) providing thermally-driven actuation for devices such as switches, tweezers, or valves. In (ii) and (iii), the main challenge is to maximize the deflections of the vertices. The amplification of total thermal motion is accomplished through the geometric arrangement and proper material choice of the lattice constituents. In a mathematical sense, (ii) and (iii) are inverse problems to (i): in (i), substrate CTEs are given, lattice materials must be chosen based on them, and skew angles are found as functions of lattice material CTE ratio. In (ii) and (iii), only the lattice materials and skew angles that provide maximal deflections of cells are used, and substrate materials are found to eliminate or mitigate thermal stresses on the substrate boundaries.

Thus, the bimaterial lattices presented in this work have application for systems requiring zero or small isotropic thermal expansion, small but graded thermal expansion, and large predetermined thermal deformation, all while maintaining relatively large stiffness, and hence they represent an exceptionally adaptable (perhaps "smart") multifunctional structure.

7.1 Contributions

The main contributions of the research are

- A mathematical model of anisotropic bimaterial lattice thermal deformation;
- A new algorithm for the design of bimaterial lattices with anisotropic thermal expansion;
- Equations linking six skew angles with three coefficients of thermal expansion of a lattice cell that account for shape change of the cell base triangle;
- Design concepts for various one-row, two-row, angled, non-planar cylindrical, and planar axisymmetric adaptive lattices;
- A method to increase structural efficiency of designed lattices;
- Experimental confirmation of analytical results;
- A computer code for cell structural analysis;
- Concepts for thermal actuators based on the anisotropic bimaterial lattices: a thermal switch, tweezers, and a valve.

7.2 Future research directions

Numerous directions of research remain open for further exploration and study. A few are listed here as follows:

- Model the lattice designs using three-dimensional finite elements;
- Manufacture thermal actuators and experimentally investigate their performance;
- Design actuators of more complicated shape.

Bibliography

E M K Abad, D Pasini, and R Cecere. Shape optimization of stress concentration free lattice for self-expandable nitinol stent-grafts. *J. Biomechanics*, 45:1028–1035, 2012.

E H Anderson, D M Moore, J L Fanson, and M A Ealey. Development of an active truss element for control of precision structures. *Optical Engineering*, 29(11):1333–1341, 1990.

H Asanuma, O Haga, J Ohira, G Hakoda, and K Kimura. Proposal of an active composite with embedded sensor. *Science and Technology of Advanced Material*, 3(2):209–216, 2002.

J Berger, C Mercer, and A G Evans. The design of bounded biomaterial lattices that combine low thermal expansion with high stiffness. *J. Am. Ceram. Soc.*, 94(S1):S42–S54, 2011.

S C Chen and M L Culpepper. Design of contoured microscale thermomechanical actuators. *J MEMS*, 15:1226–1234, 2006.

P Chopra and A S Phani. *Effective Mechanical Properties of Lattice Materials: A Comparative Study*. CANCAM, Vancouver, Canada, 2011.

E F Crawley. Intelligent structures for aerospace: a technology overview and assessment. *AIAA Journal*, 32, 8, 1994.

C H Dang. *Coefficient of thermal expansion adaptor*. Patent No US 2009/0269497 A1, 2006.

S Djouadi, R Motro, J C Pons, and B Crosnier. Active control of tensegrity systems. *Journal of Aerospace Engineering*, 11(2):37–44, April, 1998.

M Elsayed and D Pasini. Mechanics of 2d pin jointed lattice structures, aes technical reviews, part b. *Int. J. Advances Mechanics Applications Industrial Materials*, 1(1): 83–91, 2009.

M Elsayed and D Pasini. Multiscale structural design of columns made of regular octet-truss lattice material. *Int. J. Solids and Structures*, 47(14-15):1764–1774, 2010.

J S O Evans, T A Mary, and A W Sleight. Negative thermal expansion materials. *Physica B*, (241-243):311–316, 1998.

H Fan, D Fang, and F Jin. Mechanical properties of lattice grid composites. *Acta Mech.*, 24:409–418, 2008.

H Fan, F Jin, and D Fang. Uniaxial local buckling strength of periodic lattice composites. *Mater. Des.*, 30:4136–4145, 2009.

E Gdoutos, A A Shapiro, and C Daraio. Thin and thermally stable periodic metastructures. *Exp. Mech.*, (53):1735–1742, 2013.

A A Geisberger, N Sarkar, M Ellis, and G D Skidmore. Electrothermal properties and modeling of polysilicon microthermal actuators. *J MEMS*, 12:513–523, 2003.

J M Gere and S P Timoshenko. *Mechanics of materials 4th ed.* PWS Pub Co. in Boston, 1997.

L V Gibiansky and S Torquato. Thermal expansion of isotropic multiphase composites and polycrystals. *J. Mech. Phys. Solids*, 45(7):1223–1252, 1997.

L E Gibson and M F Ashby. *Cellular Solids: Structure and properties.* Cambridge University Press, Cambridge, 1997.

R T Haftka and H M Adelman. An analytical investigation of shape control of large space structures by applied temperatures. *AIAA Journal*, 23(3):450–457, 1985.

B Harris. *Fatigue in composites. Science and technology of the fatigue response of fibre-reinforced plastics.* Woodhead Pub Co, 2003.

U Herold-Schmidt, W Schaefer, and H W Zaglauer. Piezoceramics CFRP composites for active vibration control and shape control of aerospace structures. In *3rd International Conference on Intelligent Materials and 3rd European Conference on Smart Structures and Materials 718*, April 26, 1996.

L Huang, X Ma, M Gong, and Q Bian. Experimental investigation of the deformable mirror with bidirectional thermal actuators. *Optics express*, 23(13):17520–17530, 2015.

Q A Huang and N K S Lee. Analytical modeling and optimization for a laterally-driven polysilicon thermal actuator. *Microsyst. Technol*, 5:133–137, 1999.

R G Hutchinson, N Wicks, A G Evans, N A Fleck, and J W Hutchinson. Kagome plate structures for actuation. *Int. J. Solids and Structures*, 40:6969–6980, 2003.

H A Irschik. A review on static and dynamic shape control of structures by piezoelectric actuation. *Engineering Structures*, 24:5–11, 2002.

H A Irschik and U Pichler. Dynamic shape control of solids and structures by thermal expansion strains. *J Thermal Stresses*, 24:565–578, 2001.

J M Jani, M Leary, A Subic, and M A Gibson. A review of shape memory alloy research, applications and opportunities. *Materials and Design*, (56):1078–1113, 2014.

R Jassemi-Zargani and J F Simard. *Utilization of smart structures in enhanced satellites, in.* 2nd CanSmartWorkshop, 1999.

G Jefferson, T A Parthasarathy, and R Kerans. Tailorable thermal expansion hybrid structures. *Int. J. Solids and Structures*, 46(11-12):2372–2387, 2009.

A Jungen, M Pfenniger, M Tonteling, C Stampfer, and C Hierold. Electrothermal effects at the microscale and their consequences on system design. *J. Micromech. Microeng*, 16:1633–1638, 2006.

S Kaur, S Kaur, and S Poonia. Design and fabrication of twisting-type thermal actuation mechanism for micromirrors. *Int J Advanced Research in Computer and Communication Engineering*, 2(10):3849–3851, 2013.

D H Kim, Y C Park, and S Park. Design and fabrication of twisting-type thermal actuation mechanism for micromirrors. *Sensors and Actuators A: Physical*, 159(1): 79–87, 2010.

S Korkmaz. A review of active structural control: challenges for engineering informatics. *Computers and Structures*, 89:2113–2132, 2011.

M Krommer. An electromechanically coupled plate theory taking into account the influence of shear, rotatory inertia and electric feld. *Mech Res Comm*, pages 197–202, 2000.

M Krommer and H A Irschik. Reissner-mindlin-type plate theory including the direct piezoelectric and the pyroelectric effect. *Acta Mech*, 141:51–69, 2000.

R S Lakes. Cellular solid structures with unbounded thermal expansion. *J. Mater. Sci. Lett.*, 15(6):475–477, 1996.

R S Lakes. Solids with tunable positive or negative thermal expansion of unbounded magnitude. *Appl. Phys. Lett.*, 90:221905, 2007.

C Lee and C Y Wu. Study of electrothermal v-beam actuators and latched mechanism for optical switch. *J Micromechanics and Microengineering*, 15(1):11–19, 2005.

C K Lee. Theory of laminated piezoelectric plates for the design of distributed sensors/actuators. part i: governing equations and reciprocal relationships. *J Acoust Soc Am*, 87:1144–1158, 1990.

C K Lee and F C Moon. Modal sensors/actuators. *J Appl Mech*, 57:434–441, 1990.

J Lehman and R Lakes. Stiff lattices with zero thermal expansion and enhanced stiffness via rib cross section optimization. *Int. J. Mech. Mater. Des.*, (9):213–225, 2013.

A C H Leung, D D Symons, and S D Guest. *Actuation of kagome lattice structures.* Proceedings of the 45th AIAA/ASME/ASCE/AHS/ASC Structures, Structural Dynamics and Materials Conference. AIAA 2004-1525. AIAA, Palm Springs, CA, 2004.

D Li, W Liu, J Jiang, and R Xu. Placement optimization of actuator and sensor and decentralized adaptive fuzzy vibration control for large space intelligent truss structure. *SCIENCE CHINA Technological Sciences*, 54(4):853–861, 2011.

T Liedl, B Hgberg, J Tytell, D E Ingber, and W M Shih. Self-assembly of three-dimensional prestressed tensegrity structures from DNA. *Nature Nanotechnology*, (5):520–524, 2010.

T Lisec, H J Quenzer, M Kreutzer, S Hoerschelmann, B Wagner, and W Benecke. Thermally driven microvalve with buckling behaviour of pneumatic applications 2. *Sensors and Materials*, (8):303–316, 1996.

J S Liu and T J Lu. Multi-objective and multi-loading optimization of ultralightweight truss materials. *Int. J. Solids and Structures*, 41:619–635, 2004.

M McCarthy, N Tiliakos, V Modi, and L G Frechette. Thermal buckling of eccentric microfabricated nickel beams as temperature regulated nonlinear actuators for flow control. *Sensors and Actuators*, (134):37–46, 2007.

A Michael, C . Kwok, K Yu, and M R Mackenzie. A novel bistable two-way actuated out-of-plane electrothermal microbridge. *J MEMS*, 17:58–69, 2008.

D Michel, Th Graf, H J Glur, W Luthy, and H P Weber. Thermo-optically driven adaptive mirror for laser applications. *Appl. Phys. B-lasers Opt.*, 79:721–724, 2004.

M M Mikulas, G Thorwald, and B K Wada. *Design considerations for doubly curved conformable trusses*. Report JPL D-10528, Jet Propulsion Lab, Caltech, Pasadena, CA, 1993.

K Miura. *Design and operation of a deployable truss structure*. Proceedings of 18th Aerospace Mechanisms Symposium, 24 May 1984, NASA Goddard Space Flight Center, Greenbelt, Maryland, NASA-CP-2311, 1984a.

K Miura. *Variable geometry truss and its application to deployable truss and space crane arm*. Proceedings of 35th Congress of the International Astronautical Federation, 713 October 1984, Lausanne, Switzerland, IAF-84-394, 1984b.

I J Oppenheim and W O Williams. Tensegrity prisms as adaptive structures a review of active structural control: challenges for engineering informatics. *Adaptive Structures and Material Systems, ASME AD-Vol. 54, ASME Int'l. Mechanical Engineering Congress*, pages 2113–2132, November, 1997.

A S Phani. On elastic waves and related phenomena in lattice materials and structures. *AIP Advances*, 1(4):041602, 2011a.

A S Phani. *Lattice Materials: A Unified Structural Mechanics Perspective*. PHONONICS, Santa Fe, NM, USA, 2011b.

A S Phani and N A Fleck. *Elastic boundary layers in isotropic perioidc lattices*. ASME IDETC, Las Vegas, USA, 2007.

A S Phani and N A Fleck. Elastic boundary layers in two-dimensional isotropic lattices. *J. Applied Mechanics*, 75(2):021020, 2008.

A S Phani, J Woodhouse, and N A Fleck. Wave propagation in two-dimensional periodic lattices. *J. Acoustical Society of America*, 119(4):1995–2005, 2006.

L Puig, A Barton, and N Rando. A review on large deployable structures for astrophysics missions. *Acta Astronautica*, 67:12–26, 2010.

L Que, J S Park, and Y Gianchandani. Bent-beam electrothermal actuators, part I. Single beam and cascaded devices. *J Microelectromech Syst*, 10:247–254, 2001.

D S Ramrkahyani, G A Lesieutre, M Frecker, and S Bharti. Aircraft structural morphing using tendon actuated compliant cellular trusses. *Lournal of Aircraft*, 42(6):1614–1620, November-December 2005.

F Reinert and W Luthy. Thermo-optically driven adaptive mirror based on thermal expansion: preparation and resolution. *Optics express*, 13(26):10749–10753, 2005.

S T F Ross. *Finite element methods in engineering science*. Ellis Horwood, 1991.

H Sehr, A G R Evans, and A Brunnschweiller. Fabrication and test of thermal vertical bimorph actuators for movement in the wafer plane. *Micromech. Mircoeng.*, (11): 306–310, 2001.

H Sepiani, F Ebrahimi, and H Karimipour. A mathematical model for smart functionally graded beam integrated with shape memory alloy actuators. *J. Mech. Sci. Tech.*, (31): 3179–3190, 2009.

X Shen and X Chen. Mechanical performance of a cascaded v-shaped electrothermal actuator. *Int. J. of Advanced Robotic Systems*, 10:379–386, 2013.

Y Shimamura, K Udeshi, L Que, and J Park. Impact behavior and energy transfer efficiency of pulse-driven bent-beam electrothermal actuators. *J MEMS*, 15:101–110, 2006.

O Sigmund and S Torquato. Composites with extremal thermal expansion coefficients. *Appl. Phys. Lett.*, 69(21):3201–3205, 1996.

O Sigmund and S Torquato. Design of materials with extreme thermal expansion using a three-phase topology optimization method. *J. Mech. Phys. Solids*, 45(6):1037–1067, 1997.

R E Skelton and M C de Olivera. *Tensegrity systems*. New York: Springer, 2009.

R E Skelton, R Adhikari, J P Pinaud, and C Waileung. *An introduction to the mechanics of tensegrity structures*. The mechanical systems design handbook, 2000.

C A Steeves, S L dos Santos e Lucato, M He, E Antinucci, J W Hutchinson, and A G Evans. Concepts for structurally robust materials that combine low thermal expansion with high stiffness. *J. Mech. Phys. Solids*, 55(9):1803–1822, 2007.

C A Steeves, C Mercer, E Antinucci, M Y He, and A G Evans. Experimental investigation of the thermal properties of tailored expansion lattices. *Int. J. Mech Mater Des*, (5): 195–202, 2009.

T R Tauchert, F Ashida, N Noda, S Adali, and V Verijenko. Developments in thermopiezoelasticity with relevance to smart composite structures. *Compos Struct*, 48: 31–45, 2000.

S P Timoshenko. Analysis of bi-metal thermostats. *J. Opt. Soc. Am.*, (11):233–255, 1925.

M M Toropova and C A Steeves. Composite lattices with anisotropic coefficient of thermal expansion. *60th CASI Aeronautics Conference and AGM,Toronto, Ontario*, April 30-May 2, 2013a.

M M Toropova and C A Steeves. Composite lattices with anisotropic coefficient of thermal expansion. *The 4th Canadian Conference on Nonlinear Solid Mechanics (CanCNSM 2013) McGill University, Montreal, Canada*, July 23-26, 2013b.

M M Toropova and C A Steeves. Design of composite bi-material lattice adapters. *1st International Conference on Mechanics of Composites , Stony Brook University, USA*, June 8-12 , 2014a.

M M Toropova and C A Steeves. Adaptive bi-material lattices to mitigate thermal expansion mismatch in satellite structures. *65th International Astronautical Congress, Toronto, Canada*, September 29 October 3, 2014b.

M M Toropova and C A Steeves. Bimaterial lattices with anisotropic thermal expansion. *Journal of Mechanics of Materials and Structures*, 9(2):227–244, 2014c.

M M Toropova and C A Steeves. Controlling thermal deformation through the use of lattice structures. *62nd CASI Aeronautics Conference and AGM 3rd CARDN Conference, Montreal, Canada*, May 19-21, 2015a.

M M Toropova and C A Steeves. Thermal actuation through bimaterial lattices. *ASME Conference on Smart Materials, Adaptive Structures and Intelligent Systems SMASIS, Colorado Springs, USA*, September 21-23, 2015b.

M M Toropova and C A Steeves. Adaptive bimaterial lattices to mitigate thermal expansion mismatch stresses in satellite structures. *Acta Astronautica*, 113:132–141, 2015c.

H S Tzou. Multi-field transducers, devices, mechatronic systems, and structronic systems with smart materials. *Shock Vibrat Digest*, 30:282–294, 1998.

J Varona, M Tecpoyotl-Torres, and A A Hamoui. *Modeling of MEMS Thermal Actuation with External Heat Source*. Fourth Congress of Electronics, Robotics and Automotive Mechanics, DOI 10.1109/CERMA.2007.6, 2007.

G Vdovin and M Loktev. Deformable mirror with thermal actuators. *Opt Letters*, 27: 677–679, 2002.

A Vigliotti and D Pasini. Stiffness and strength of tridimensional periodic lattices. *Computer Methods in Applied Mechanics and Engineering*, 229-232:27–43, 2012.

A Vigliotti and D Pasini. Analysis and design of lattice materials for large cord and curvature variations in skin panels of morphing wings. *Smart Materials and Structures*, 24(3):037006, 2015.

A Vigliotti, V S Deshpande, and D Pasini. Non linear constitutive models for lattice materials. *J. Mech. Physics Solids*, 64:44–60, 2014.

N Wicks and S D Guest. Single member actuation in large repetitive truss structures. *Int. J. Solids and Structures*, 41:965–978, 2004.

N Wicks and J W Hutchinson. Optimal truss plates. *Int. J. Solids and Structures*, 38: 5165–5183, 2001.

J W Wittwer, M S Baker, and L L Howell. Simulation, measurement, and asymmetric buckling of thermal microactuators. *Sens Actuators A Phys*, 128:395–401, 2006.

A Yousefiani, J M Comfort, J G Vollmer, and M L Hand. *Joined composite structures with a graded coefficient of thermal expansion for extreme environment applications*. Patent No US 2009/0266870 A1, 2009a.

A Yousefiani, J G Vollmer, M L Hand, and J M Comfort. *Built-up composite structures with a graded coefficient of thermal expansion for extreme environment applications*. Patent No US 2009/0269497 A1, 2009b.

C Zhang, W K Binienda, G N Morscher, R E Martin, and L W Kohlman. Experimental and fem study of thermal cycling induced microcracking in carbon/epoxy triaxial traded composites. *Composites Part A: Applied Science and Manufacturing*, 46:34–44, 2013.

Y H Zhang, X M Qiu, and D N Fan. Mechanical properties of two novel planar lattice structures. *Int. J. Solids and Structures*, 45(13):3751–3768, 2008.